Alexander Pieter Betzler, BSc

Coherent Population Trapping: Experimental Parameter Studies

MASTER'S THESIS

to achieve the university degree of

Diplom-Ingenieur

Master's degree programme: Technical Physics

submitted to

Graz University of Technology

Supervisors

Supervisor Em.Univ.-Prof. Dipl.-Phys. Dr.rer.nat. Wolfgang Ernst

Co-Supervisor Dipl.-Ing. Dr.techn. Roland Lammegger

Institute of Experimental Physics

Graz, November 2020

AFFIDAVIT

I declare that I have authored this thesis independently, that I have not used other than the declared sources/resources, and that I have explicitly indicated all material which has been quoted either literally or by content from the sources used. The text document uploaded to TUGRAZonline is identical to the present master's thesis.

Date, Signature

Abstract

Coherent Population Trapping is a quantum interference phenomenon which can be achieved in three-level systems interacting with a dichromatic laser field.
The most straightforward system consists of two long lived ground states and one short lived excited state and is called Λ-system. If the laser frequency difference is exactly the ground-state spacing, the atoms are first pumped and then trapped in a state, that does not interact with the laser field. In this case absorption and fluorescence are severely reduced: hence this state is also called Dark State.
The typical linewidth of this feature is orders of magnitude smaller compared to a typical Doppler broadened absorption spectrum and thus can be used to measure the ground-state energy spacing with remarkable accuracy. This lends itself to applications, where high precision is of utmost importance, such as atomic clocks and magnetometry.
The CDSM Coupled Dark State Magnetometer, build for space exploration, is an example of a magnetometer, utilising this phenomenon. The necessary Dark States are excited with an frequency modulated VCSEL in the ^{87}Rb hyperfine structure. As the line shape and the exact position of the CPT resonance are of great consequence for the accuracy and possible range of the CDSM, parameters influencing the resonance have to be studied carefully.
Therefore, in this work, the effect of buffer-gas-pressure (Neon), Rb-cell-temperature, laser intensity, detuning and microwave power have been measured. The results were used to optimize the operating parameters of the CDSM.

Kurzfassung

Coherent Population Trapping ist ein Quanteninterferenzeffekt, der in Dreiniveausystemen mit einem dichromatischen Laserfeld erreicht werden kann.
Das einfachste System besteht aus zwei langlebigen Grundzuständen und einem kurzlebigen angeregten Zustand und heißt Λ-system. Wenn die Frequenzdifferenz des Laserfeldes exakt die Energiedifferenz der Grundzustände ist, wird das Atom in einem Zustand gefangen, der nicht mehr mit dem Laserfeld interagiert. Da in diesem Zustand die Fluoreszenz stark unterdrückt ist wird dieser Zustand auch Dunkelzustand genannt.
Die Linienbreite dieser CPT Resonanzen ist um Größenordnungen kleiner als die typischen Breiten von Dopplerverbreiterten Absorptionsspektren und dadurch kann die Energiedifferenz zwischen den Grundzuständen bemerkenswert genau vermessen werden. Ebendiese Genauigkeit macht CPT für verschiedene Anwendung sehr interessant, allen voran für Atomuhren und Magnetometer.
Das CDSM Coupled Dark State Magnetometer basiert auf diesem Phänomen. In diesem Fall werden die notwendigen Resonanzen mit einem frequenzmodelierten VCSEL in der Hyperfeinstruktur von ^{87}Rb angeregt. Da die Linienform und Position des Dunkelzustandes von enormer Wichtigkeit für die Genauigkeit und den möglichen Messbereich des CDSM sind wurden Einflüsse darauf untersucht.
Dementsprechend werden in dieser Arbeit die Auswirkungen von Puffer-Gas-Druck (Neon), Rb-Zellentemperatur, Laser-Intensität, Laser-Verstimmung und Mikrowellenkraft auf die CPT Resonanz vermessen. Die Ergebnisse dieser Arbeit werden beim Betrieb des CDSM berücksichtigt.

Contents

1 Fundamentals

1.1 Coherent Population Trapping

Coherent Population Trapping is a quantum interference phenomenon which can be achieved in the simplest case in three-level systems interacting with two resonant laser fields. In a Λ-system, as shown in figure 1.1, the Dark Resonance is observed if the laser frequency difference is exactly the ground-state energy spacing. In this case the atoms are pumped into a state that does not interact with the laser fields and hence absorption and fluorescence is reduced [1].
This effect was first observed by Alzetta, Gozzini, Moi and Orriols in 1976[2].
The explanation of the Coherent Population Trapping effect follows the papers of Arimondo[1], Wynands et al.[3], Agap'ev et al.[4] and Orriols[5].

1.1.1 Λ-system

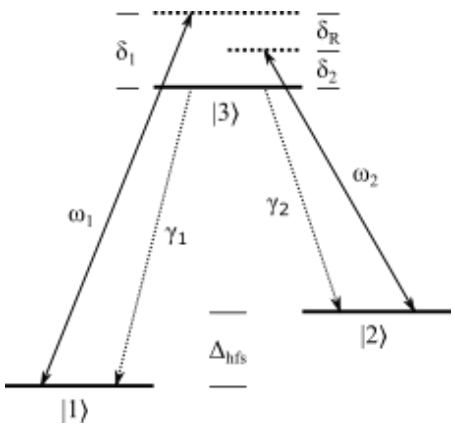

Figure 1.1: The energies in a Λ scheme are $E_1 < E_2 < E_3$. $|1\rangle$ and $|2\rangle$ are two dipole forbidden long-lived ground states. $|3\rangle$ is the excited state. Dipole transitions are excited between $|n\rangle$ and $|3\rangle$ with a Laser with frequency ω_n. γ_n are the decay rates to the two ground states. δ_n are the respective detunings and δ_R is the Raman-detuning. Δ_{hfs} is the energy difference between $|1\rangle$ and $|2\rangle$.

Λ-systems consist of two dipole forbidden long-lived states $|1\rangle$ and $|2\rangle$ and one excited state $|3\rangle$ interacting with two laser fields $\vec{e_1}E_1 exp(-i\omega_1 t - i\varphi_1 + ik_1 z)$ and $\vec{e_2}E_2 exp(-i\omega_2 t - i\varphi_2 + ik_2 z)$. Only one laser is resonant with one transition at a time. Furthermore the

spatial component can be ignored for co-propagating lasers.
The laser detuning from the respective transition frequency is

$$\delta_n = \omega_n - \omega_{3n} \quad n = 1, 2 \tag{1.1}$$

and the Raman detuning δ_R from the two photon-resonance is defined as

$$\delta_R = \omega_1 - \omega_2 - \Delta_{hfs} \tag{1.2}$$

with Δ_{hfs} being the ground states frequency difference. The operator

$$\hat{V} = -\hat{d}\vec{E} \tag{1.3}$$

describes the interaction between the monochromatic light fields and the atom with $\hat{d}$ being the dipole operator. This interaction operator $\hat{V}$ can be written as

$$\hat{V} = \hbar\frac{g_1}{2}e^{-i\omega_1 t - i\varphi_1}\left|3\right\rangle\left\langle 1\right| + \hbar\frac{g_2}{2}e^{-i\omega_2 t - i\varphi_2}\left|3\right\rangle\left\langle 2\right| + h.c. \tag{1.4}$$

using the rotating wave approximation (RWA) to eliminate nonresonant terms.

$$g_n = \frac{E_n}{\hbar}\left\langle 3\right|\vec{de_n}\left|n\right\rangle \quad n = 1, 2 \tag{1.5}$$

is called the Rabi Frequency and characterizes the strength of the atom-laser-interaction. Instead of describing the system in the energy eigenstates $|1\rangle$ and $|2\rangle$ for an atom at rest, it is better to use the linear combinations $|C\rangle$ and $|NC\rangle$, which are obtained by unitary transformation.

$$\begin{aligned} \left|C\right\rangle &= \frac{1}{\sqrt{|g_1^2| + |g_2^2|}}(g_1\left|1\right\rangle + g_2^*\left|2\right\rangle) \\ \left|NC\right\rangle &= \frac{1}{\sqrt{|g_1^2| + |g_2^2|}}(g_2\left|1\right\rangle - g_1\left|2\right\rangle) \end{aligned} \tag{1.6}$$

These develop in time:

$$\begin{aligned} \left|C\right\rangle &= \frac{1}{\sqrt{|g_1^2| + |g_2^2|}}(e^{-i\Omega_1 t}g_1\left|1\right\rangle + e^{-i\Omega_2 t}g_2^*\left|2\right\rangle) \\ \left|NC\right\rangle &= \frac{1}{\sqrt{|g_1^2| + |g_2^2|}}(e^{-i\Omega_1 t}g_2\left|1\right\rangle - e^{-i\Omega_2 t}g_1\left|2\right\rangle) \end{aligned} \tag{1.7}$$

The transition dipol matrix elements thus yield:

$$\begin{aligned} \left\langle 3\right|\hat{V}\left|C\right\rangle &= \frac{\hbar}{2\sqrt{|g_1^2| + |g_2^2|}}e^{-i(\Omega_1+\omega_1)t - i\varphi_1)}(|g_1|^2 + |g_2|^2 e^{i\delta_R t + i(\varphi_1 - \varphi_2)}) \\ \left\langle 3\right|\hat{V}\left|NC\right\rangle &= \frac{\hbar g_1 g_2}{2\sqrt{|g_1^2| + |g_2^2|}}e^{-i(\Omega_1+\omega_1)t - i\varphi_1)}(1 - e^{i\delta_R t + i(\varphi_1 - \varphi_2)}) \end{aligned} \tag{1.8}$$

If the difference frequency of the two lasers is exactly the ground state splitting, $\omega_1 - \omega_2 = \Delta_{hfs}$ thus $\delta_R = 0$, and the relative phase is $\Delta\varphi = \varphi_1 - \varphi_2 = 0$, the transition matrix elements become:

$$\begin{aligned} \langle 3| \hat{V} |C\rangle &= \frac{\hbar\sqrt{|g_1^2| + |g_2^2|}}{2} e^{-i(\Omega_1+\omega_1)t - i\varphi_1} \\ \langle 3| \hat{V} |NC\rangle &= 0 \end{aligned} \tag{1.9}$$

The state $|NC\rangle$ is called coherent dark state and cannot be excited to the upper state $|3\rangle$ by the present laser field. Furthermore any population in the coherent state $|C\rangle$ is also optically pumped into the dark state where it is then trapped. Thus after a certain time most of the population is trapped in the coherent dark state and absorption and fluorescence is severely reduced.
A more realistic approach to describing the quantum mechanical system is usually done with the density matrix formalism. It includes decay and damping constants and more accurately describes the underlying physics.

1.1.2 Density Matrix Formalism

The Density Matrix Formalism is designed to deal with an ensemble of of pure states (mixed states), for example, large quantities of atoms interacting with each other and their environment, as is the case in the here treated CPT phenomenon. It allows also a easy implementation of physical effects such as relaxation and coherence loss.
In general the density operator is defined as[6]:

$$\rho = \sum_i P_i |\psi_i\rangle \langle\psi_i| \tag{1.10}$$

P_i is the probability of an object of the ensemble to be in the state $|\psi_i\rangle$.
Important properties of the density operator are[6]:

1. Tr(ρ)=1
2. it is hermitian $\rho = \rho^\dagger$
3. it is positive $\langle\psi| \rho |\psi\rangle > 0$ for all $|\psi\rangle$

1.1.3 Density Matrix Formalism in the case of CPT

For CPT the three possible states of the Λ-system are the two lower energy eigenstates $|1\rangle$,$|2\rangle$ and the excited energy eigenstate$|3\rangle$. The equation of motion for p is described by the Liouville or Von-Neumann equation:

$$i\hbar\frac{\partial\hat{\rho}}{\partial t} = [\hat{H}_0 + \hat{V}, \hat{\rho}] + \hat{R}\hat{\rho} \tag{1.11}$$

expanded with the relaxation operator $\hat{R}$ and the atom-laser interaction Hamiltonian $\hat{V}$ given by equation 1.4 on page 9.

To eliminate fast dependencies in the time evolution of the density matrix elements the off-diagonal ones are substituted with:

$$\begin{aligned}\tilde{\rho}_{n3} &= \rho_{n3} e^{-i\delta_n t - i\varphi_n} \quad n = 1, 2 \\ \tilde{\rho}_{12} &= \rho_{12} e^{-i(\delta_1 - \delta_2)t - i(\varphi_1 - \varphi_2)}\end{aligned} \tag{1.12}$$

For the Λ-system this results in the following equations for the elements of the density matrix:

$$\begin{aligned}\frac{\partial \rho_{11}}{\partial t} &= i\frac{g_1}{2}\tilde{\rho}_{31} - \gamma_1 \rho_{33} \\ \frac{\partial \rho_{22}}{\partial t} &= i\frac{g_2}{2}\tilde{\rho}_{32} - \gamma_2 \rho_{33} \\ \frac{\partial \rho_{33}}{\partial t} &= i\frac{g_1}{2}\tilde{\rho}_{31} + i\frac{g_2}{2}\tilde{\rho}_{32} - (\gamma_1 + \gamma_2)\rho_{33} \\ \frac{\partial \tilde{\rho_{13}}}{\partial t} &= i\frac{g_1}{2}(\rho_{33} - \rho_{11}) - i\frac{g_2}{2}\tilde{\rho}_{21} - (\gamma_1 + i\delta_1)\tilde{\rho}_{13} \\ \frac{\partial \tilde{\rho}_{23}}{\partial t} &= i\frac{g_2}{2}(\rho_{33} - \rho_{22}) - i\frac{g_1}{2}\tilde{\rho}_{12} - (\gamma_2 + i\delta_2)\tilde{\rho}_{23} \\ \frac{\partial \tilde{\rho}_{12}}{\partial t} &= -i\frac{g_2}{2}\tilde{\rho}_{32} + i\frac{g_1}{2}\tilde{\rho}_{13} - (\Gamma + i\delta_R)\tilde{\rho}_{12}\end{aligned} \tag{1.13}$$

where γ_n are the partial decay rates and Γ the relaxation of the coherence between the ground states. In the simplest case these are the only non-zero relaxation parameters and have, together with the intensity, a strong influence on the CPT-resonance, for example, only if $g^2 > \gamma_n \Gamma$ is CPT observable.
Kelley, Harshman, Blum and Gustafson[7] have reported the steady-state solutions of these equations in "Radiative renormalization analysis of optical double resonance", but instead of showing these , it is more convenient to showcase Coherent Population Trapping by presenting the numerical solutions.

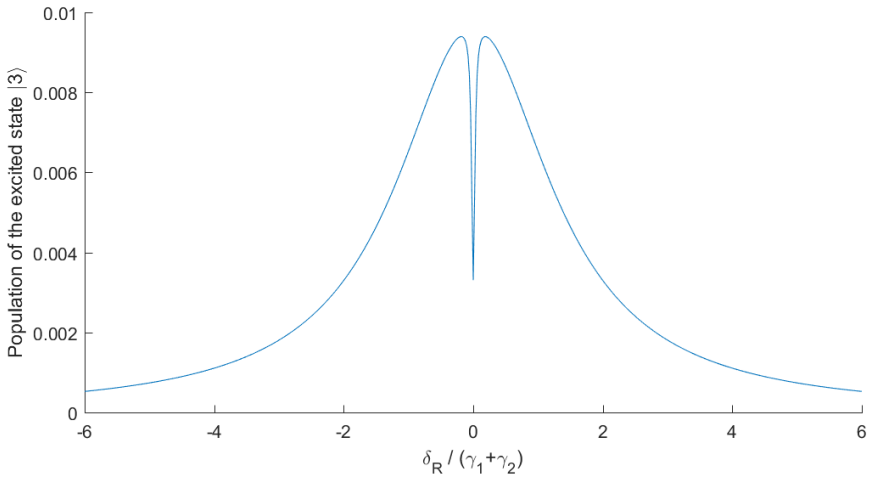

Figure 1.2: Population of the excited state $|3\rangle$ as a function of the normalized Raman Detuning. Γ determines the depth of the central dip. If Γ=0 the excited state is depopulated in the middle.

In figure 1.2 the occupation of the excited state $|3\rangle$ are plotted as a function of the normalized Raman detuning $\frac{\delta_R}{(\gamma_1+\gamma_2)}$ for the Λ-system, i.e.. one laser is scanned through its resonance while the second one is fixed at theirs (δ_2=0). Most prominently a strong dip appears in the expected Lorentzian line-shape, when the first laser is also in resonance, and therefore the raman-detuning is δ_R=0. In this case most of the population is trapped in the lower states $|1\rangle$ and $|2\rangle$.
A more thorough analysis of the CPT phenomenon can be found in Arimondo[1], and Agap'ev et al.[4].

1.2 The Rubidium Atom

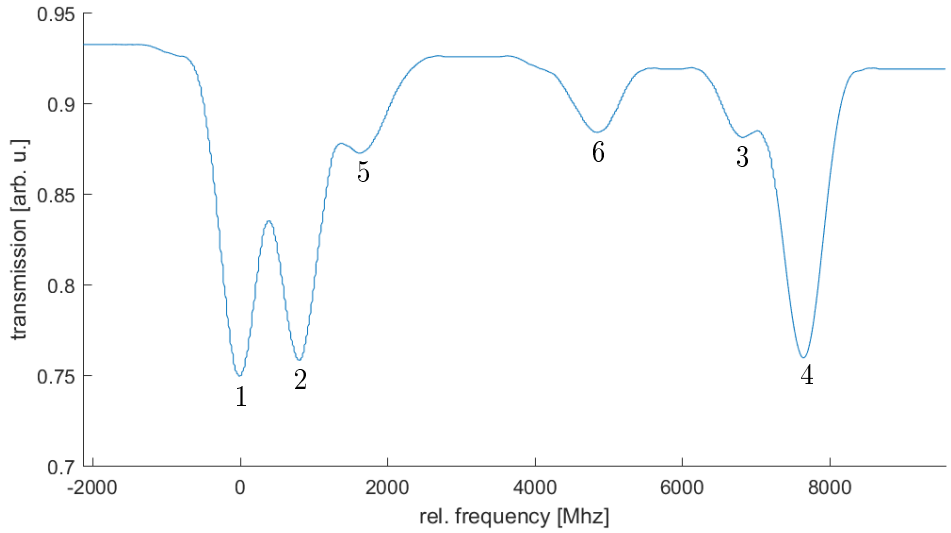

Figure 1.3: Rb D_1 Transmission Spectrum
1 = ^{87}Rb: $5^2S_{1/2}$ F=2 $\longrightarrow$ $5^2P_{1/2}$ F=1
2 = ^{87}Rb: $5^2S_{1/2}$ F=2 $\longrightarrow$ $5^2P_{1/2}$ F=2
3 = ^{87}Rb: $5^2S_{1/2}$ F=1 $\longrightarrow$ $5^2P_{1/2}$ F=1
4 = ^{87}Rb: $5^2S_{1/2}$ F=1 $\longrightarrow$ $5^2P_{1/2}$ F=2
5 & 6 = ^{85}Rb

The data presented here is from the paper "Rubidium 87 D Line Data" by Steck [8].
Rubidium is a alkali metal with the atomic number 37. It similar in behaviour to most alkali metals, as it is also dominated by its s-valence electron in the outer-most shell. Two natural isotopes of Rubidium exist on earth: 72% is made up by the stable ^{85}Rb and 28% by the radioactive ^{87}Rb, with a half-time of 49 billion years.
In the following experiments ^{87}Rb was used. The two most important ^{87}Rb transitions are the D_1 line ($5^2S_{1/2} \longrightarrow 5^2P_{1/2}$) with a transition wavelength of 795 nm and the D_2 line ($5^2S_{1/2} \longrightarrow 5^2P_{3/2}$) with a transition wavelength of 780 nm.
The hyperfine structure of the $5^2S_{1/2}$ state consists of the lower energy level with F=1 and the higher level with F=2, separated by the splitting frequency of 6.834 GHz. The upper state $5^2P_{1/2}$ includes two hyperfine components (F=1,2) and the upper state of the D_2 transition $5^2P_{3/2}$ is made up by 4 different energy levels (F=0,1,2,3).
In the present work the Λ-system was realized between the hyperfine components F=1 and F=2 of the $5^2S_{1/2}$ state and the upper state $5^2P_{1/2}$ F=2.
Thus the exact position and the width of the CPT-resonance is highly dependent on parameters influencing the hyperfine splitting frequency.

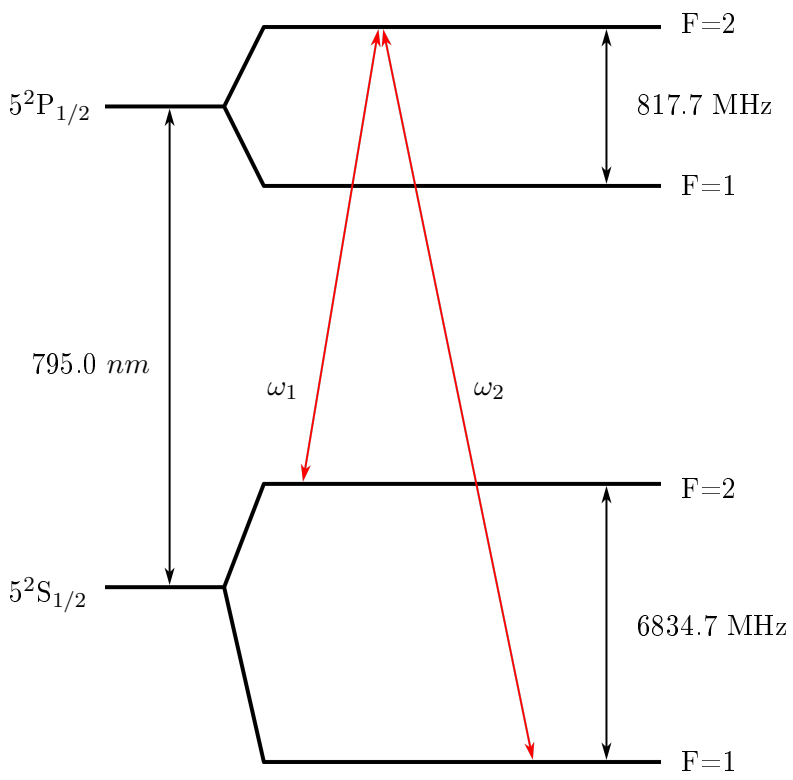

Figure 1.4: Hyperfine Structure of the D_1 line of ^{87}Rb
The used Λ-system is depicted in red.

1.3 Buffer Gas

The primary purpose of buffer Gas is to prevent relaxation of the rubidium atoms on the walls of the cell. The probability of losing coherence upon hitting a wall is very close to unity. This prolongs the lifetime of the atoms in a given state and hence decreases the line width. It also increases the transit time of the atoms in the laser beam and reduces Doppler broadening due to the Dicke effect[9][10][11].
Many different gases, and combinations thereof, can be used as buffer gas. Some shift the frequency to the blue, others, especially heavy gases, to the red.
The absolute effect on the resonance position is not only dependent on the pressure of the buffer gas but the gas also introduces a temperature dependence.

1.3.1 Buffer Gas Frequency Shift

This explanation follows the one given by Vanier in "The Quantum Physics of Atomic Frequency Standards"[9].
The general Hamilton describing the interaction between the akali and buffer gas atoms, under the assumption that they do not react chemically with each other, is:

$$\mathcal{H} = U(r) + \delta A(r)\vec{S}\vec{I} + \gamma(r)\vec{S}\vec{N} + \delta(r)\vec{I}\vec{N} \tag{1.14}$$

$U(r)$ describes the electrostatic forces that create the phenomenon of scattering.
The distortion of the hyperfine interaction is $\delta A(r)\vec{S}\vec{I}$.
$\gamma(r)\vec{S}\vec{N}$ and $\delta(r)\vec{I}\vec{N}$ describes the spin-orbit coupling between the angular momentum $\vec{N}$ and the alkali atom spin $\vec{S}$ and the alkali atom nuclear spin $\vec{I}$, respectively.
The first electrostatic term in the Hamiltonian can be approximated with the Lennard-Jones potential. It does not interact with the electronic spin and does not affect the relaxation. Furthermore the nuclear spin-orbit coupling is much smaller than the electronic spin-orbit coupling and is hence neglected. The resulting Hamiltonian only consists of the following terms:

$$\mathcal{H} = \delta A(r)\vec{S}\vec{I} + \gamma(r)\vec{S}\vec{N} \tag{1.15}$$

The spin-orbit interaction $\gamma(r)\vec{S}\vec{N}$ can be most easily calculated by replacing the actual spin-orbit coupling with the interaction between the spin and a random magnetic field.

$$\gamma(r)\vec{N} = -\gamma_s \hbar \vec{B}(t) \tag{1.16}$$

A rather tedious calculation reveals that the influence on the hyperfine structure is very small compared to the remaining term in the Hamiltonian and can thus be neglected.
The last term to be considered is $\delta A(r)\vec{S}\vec{I}$, describing the variation in the hyperfine interaction.
Van der Waals forces decrease the electron density at the atomic core, therefore decreasing the interaction between the nucleus and the electron cloud. On the other hand if the alkali atoms and the buffer gas atoms get too close and the electron clouds start to overlap the density at the core increases, which in turn boosts the hyperfine interaction.

These forces can result in a positive or negative shift of the hyperfine frequency.
If the buffer gas atoms are fixed in space and their influence, governed by their distance to the alkali, on the resonance is averaged over, the resulting relative frequency shift per buffer gas pressure at a constant density is described by the equation:

$$\frac{\delta\nu_{BG}}{P} = \frac{1}{\hbar k_B T}\int_0^\infty \delta E(r)_{HFS} e^{-\frac{U(r)}{k_B T}} r^2 dr \tag{1.17}$$

The Lennard-Jones 6-12 potential is often used in this equation,

$$U(r) = \epsilon[(\frac{r_m}{r})^{12} - 2(\frac{r_m}{r})^6] \tag{1.18}$$

where ϵ and r_m are the depth and position of the minimum.
$\delta E(r)_{HFS}$ is the variation of the hyperfine splitting and different ones have to be used for long and short range forces. Although the equation is only in qualitative agreement with experiments some conclusions can be drawn from it. First, the pressure shift is expected to be linear function of buffer gas pressure and secondly $\delta\nu_{BG}$ is also a function of temperature.
This temperature dependence around the temperature T_0 for sealed cells is given by:

$$\delta\nu_{BG} = P_0[\beta_0 + \delta_0(T - T_0) + \gamma_0(T - T_0)^2] \tag{1.19}$$

where P_0 is the buffer gas pressure, β_0 the pressure shift coefficient,δ_0 and γ_0 are the first and second order temperature coefficients and T the temperature of the atoms.
The coefficients can be calculated from 1.17 but again the results are not satisfactory. This is due to the necessary simplifications and difficulties regarding $\delta E(r)_{HFS}$. Different $\delta E(r)_{HFS}$ have to evaluated based on the distance between the alkali and the buffer gas atom. In close proximity short-range forces should dominate. Thus a arbitrary cut-off point between short and long-range forces has to be chosen, which greatly affects the results.
There are however experimental values given in the literature, but even these vary widely as can be seen in table 1.1.

1.3.2 Doppler Broadening and Dicke Effect

Introducing a buffer gas not only shifts the position of the hyperfine splitting frequency, but also influences the width of the CPT resonance. The buffer gas pressure, minimizing the linewidth, is different for any given cell size[12] and also depends on the operating temperature.
In a hot vapor cell the thermal motion of the Rubidium atoms follows the Maxwell-Boltzmann distribution. Thus the frequency of the resonance is shifted depending on the velocity of the alkali atoms with respect to the beam propagation direction: the Doppler effect. This leads to a doppler broadened CPT resonance with a full width at half maximum of[13]:

$$\Delta\nu_D = \frac{\nu_0}{c}\sqrt{\frac{8k_B T ln2}{m}} \tag{1.20}$$

with ν_0 the central frequency and m the mass of the Rubidium atom.
For example for Rubidium at room temperature a Doppler width of $\nu_D \approx 500MHz$ would be expected.
However the linewidth of the spectral feature can severely reduced by introducing a buffer gas. The buffer gas leads to a narrowing of the line as a result of the Dicke effect[14]. The mean free path of the Alkali atoms is greatly reduced due to elastic (non groundstate-coherence destroying) collisions with the buffer gas. If the mean free path of the atom is much smaller than the wavelength of the transition, the atom changes velocity and direction many times during an absorption event. This leads to an averaging over many different velocities, resulting in a reduced linewidth. According to Firstenberg et al [15] the Doppler broadening is reduced by a factor of

$$\eta = 2\pi \frac{L}{\lambda_{CPT}}, \tag{1.21}$$

where L is the mean free path and λ_{CPT} the splitting frequency between the two ground states.
For typical experimental conditions, e.g. a small vapor cell at room temperature filled with Rb and several Torr of buffer gas, $\eta \approx 10^{-5}$[16] and the Doppler effect even becomes negligible compared to other broadening factors.

1.3.3 Pressure Broadening

Collisions between atoms do not only lead to Dicke narrowing and the frequency shift discussed in subsection 1.3.1, but also cause broadening themselves.
The effect, responsible for shifting the resonance frequency of the undisturbed atom, is dependent on the distance, which is statistically distributed. Therefore the frequency shift is also statistically distributed causing a broadening of the line [13].
Furthermore both elastic and inelastic collisions disturb the ground state coherence reducing its lifetime, which again causes a broadening of the line. This broadening rises with increasing pressure and is temperature dependent. The result of this effect can be estimated from the time in between collision events $t_P = \frac{1}{\Omega_P} = \frac{1}{n\sigma v}$. The resulting spectral line is a lorentz profile with a FWHM of[17]:

$$\Delta\nu_P = \frac{n\sigma}{2\pi}\sqrt{\frac{2k_BT}{m}}, \tag{1.22}$$

where n is the particle density proportional to the buffer gas pressure within the cell, m the mass of the atom and σ is the effective collosional cross section.

1.3.4 Neon

In the present work in all but one case Neon was used as a buffer gas. Neon is noble gas with atomic number 10. It is colourless, odourless, monoatomic and is inherently unreactive.

As any other buffer gas it is introduced to reduce wall relaxation at the walls. Some also improve the linewidth by reducing the relaxation caused by fluorescence radiation, in that they quench the fluorescence, but neon does not have these properties[18].
Neon is light buffer gas and hence the dark resonance is shifted to higher frequencies because of major contribution of the exchange interaction[19]. As discussed in 1.3.1 on page 15 the shift induced by a buffer gas can be approximated by equation 1.19. The values for the coefficients found in "The Quantum Physics of Atomic Frequency Standards"[9] are:

Table 1.1: β and δ for Neon

$\frac{\beta}{\nu_0}$ $[\frac{10^{-9}}{\mathbf{Torr}}]$	$\frac{\delta}{\nu_0}$ $[\frac{10^{-12}}{\mathbf{°CTorr}}]$	t_0 **[°C]**	t_s **[°C]**	**Reference**
52.6	26	60	27	Bean [20]
57.4	40	25	25	Bender [21]
60.4	19	60	27	Batygin [22]

1.4 VCSEL - Vertical-Cavity Surface-Emmiting Laser

The Vertical-cavity surface emitting Laser, VCSEL, is a semiconductor laser with a beam emission from the top or bottom surface of the wafer.
VCSELs are small, cheap, reliable and have usually Gaussian beams. Furthermore they have a high modulation bandwidth and frequencies are available suitable for atomic spectroscopy on the alkalis[23][24][25]. Disadvantages are their low output power and their rather large linewidth of several 10 MHz[26].

1.4.1 Basic Principles of a Semiconductor-Diode Laser

If a diode is operated in the forward direction, electrons and holes can recombine in the p-n-junction and may give off the energy difference by spontaneous emission. The wavelength of the emitted light is governed by the band gap E_g between conduction and valence band. The surface of the semiconductor is reflective and provides optical feedback leading to induced emission. When the forward current is sufficiently strong, the induced-emission rate exceeds the other recombination processes and intensity builds up. Once the intensity gain is equal to the losses through the reflective surfaces, lasing starts[27].
The potential wavelengths of the device are set by the width of the spectral gain profile and the laser resonator[13]:

$$\delta\lambda = \frac{\lambda^2}{2nd(1-(\frac{\lambda}{n})\frac{\mathrm{d}n}{\mathrm{d}\lambda})}, \tag{1.23}$$

where n is the refractive index and d the length of the resonator.
The wavelength of the laser diode can be tuned by every parameter affecting the band gap, but most commonly it is done by varying the current or the temperature[13].

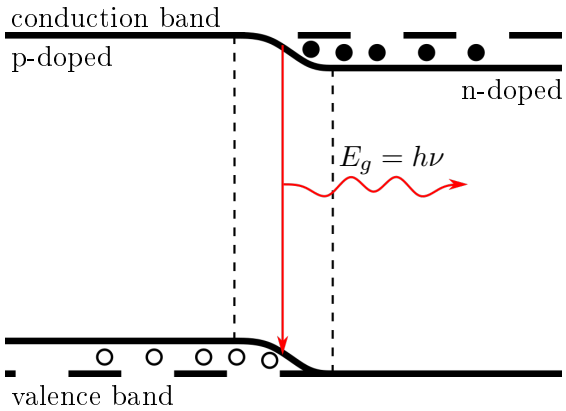

Figure 1.5: Schematic Band diagram of a light-emitting diode. The electrons of the conduction band combine with the holes of the valence band emitting a photon with the energy $E_g = h\nu$. If the Laserdiode is operated below the threshold current is functions like a conventional light-emitting diode.

1.4.2 Typical Structure of a VCSEL

A basic VCSEL is made up of a bottom distributed Bragg reflector (DBR) mirror, an narrow active region and a top DBR-mirror.
A distributed Bragg reflector is made up of an alternating sequence of $\lambda/4$ thick layers with low and high refractive index, built up in a way that it has a reflectivity of nearly unity. One of the mirrors is worse than the other, setting this one as the laser beam direction. The mirrors have to be this good because the gain per pass of the small active region is only about 1% [28]. Moreover the reflectors are similarly doped as the pn junction in the middle.
The active region is a semiconductor containing one or several quantum wells forming a double-heterostructure. The advantage of quantum wells is a decreased threshold current and a larger differential gain[29] because the charge carriers are confined in the QW, hence increasing the charge carrier density.
Furthermore the VCSEL is inherently a single-mode device due to the small size of the of its gain volume: Only one mode has its maximum within the gain profile and is amplified[26][27].

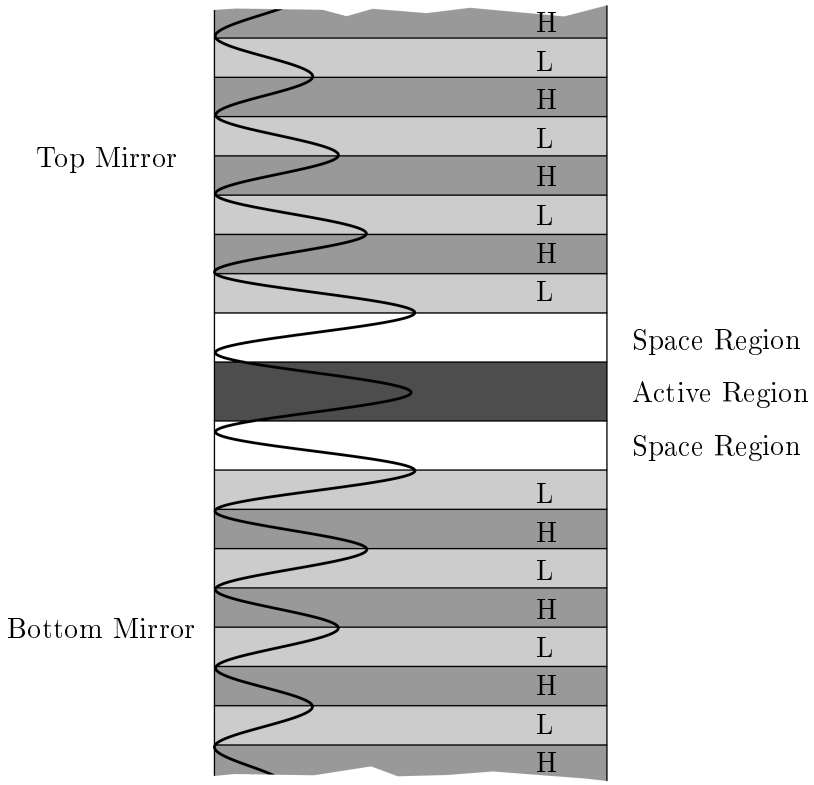

Figure 1.6: Schematic depiction of a VCSEL with Intensity distribution around the active region
H are layers with high index of refraction. L are layers with low index of refraction. In a typical VCSEL the DB-reflector consists of 30+ HL pairs [27]. The active region and the HL layers have a thickness of about $\frac{\lambda}{4n}$ [24]. The distance between the mirrors is $\frac{\lambda}{n}$ [27].

1.4.3 Modulation

In order to realise the laser field necessary to observe Coherent Population Trapping one could either use two different lasers with frequencies Δ_{hfs} apart or one RF modulated laser. The latter case greatly reduces the complexity of the experiment because there is no need for high frequency electronic systems to stabilize the difference frequency and the phase relationship.
There are many different ways achieve a RF modulated Laser but one of the simplest is the direct modulation of the diode current [30].

The equation describing a frequency-modulated laser field is[31]:

$$\begin{aligned} E &= E_0 e^{(i\omega_0 t + \beta \sin(\omega_m t))} \\ \beta &= 2\pi \frac{\Delta F}{\omega_m} \end{aligned} \tag{1.24}$$

where ω_0 is the carrier frequency, ω_m the modulation frequency, ΔF the maximum frequency deviation, and β is the modulation index.
This modulation leads to a frequency comb consisting of the carrier ω_0 with multiple sidebands at the frequencies:

$$\omega_s = \omega_0 \pm n\omega_m \quad n = 1, 2, 3...\infty \tag{1.25}$$

The amplitudes of these decrease with increasing n thus higher-order sidebands can be neglected.
The optical laser spectrum described by 1.24 can be expanded into first-order Bessel functions $J_n(\beta)$[31]:

$$\begin{aligned} E = & J_0 E_0 \sin(\omega_0 t) + J_1 E_0 \sin((\omega_0 + \omega_m)t) \\ & - J_1 E_0 \sin((\omega_0 - \omega_m)t) + ... \\ & + J_1 E_0 \sin((\omega_0 + n\omega_m)t) \\ & + (-1)^n J_1 E_0 \sin((\omega_0 - n\omega_m)t) \end{aligned} \tag{1.26}$$

The intensity of any given sideband is determined by the square of the coefficient in front of the respective sine.
In the case of a direct modulation of the injection current substantial amplitude modulation occurs besides the desired FM[32]. This leads to a asymmetry in the intensity of the n^{th} and the $-n^{th}$ order sideband. Furthermore the share of the total laser power in the sidebands is directly proportional to the power of the modulating RF field [30].
There are three ways to efficiently measure the coherent population trapping resonance with a frequency modualted laser: One can either use both first order sidebands or the carrier with one of two sidebands. In the first case one would use a modulation frequency of Δ_{hfs} in latter two one of $\frac{\Delta_{hfs}}{2}$. For Rubidium the values are about 6.8 GHz and 3.4 GHz, respectively.

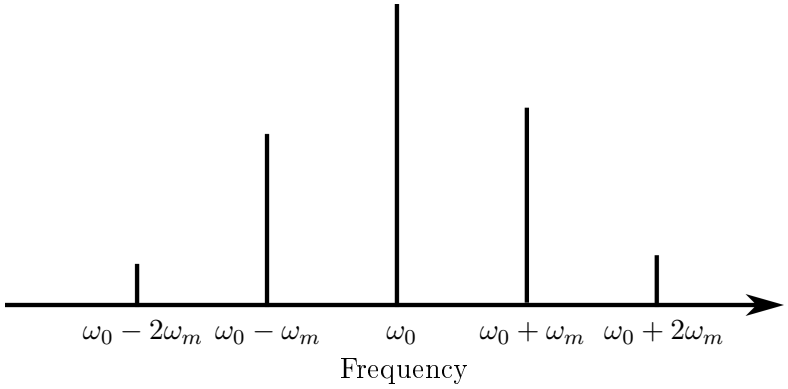

Figure 1.7: Schematic of the laser spectrum under frequency modulation. In order to measure the CPT-resonance in Rubidium a RF of $\omega_m = 6.8$ GHz or of $\omega_m = 3.4$ GHz

1.4.4 Light Shift

The interaction between the electric field of the laser and the induced atomic dipole moment leads to a shift of the atomic energy levels[33][34]. The resulting light shift is given by [35][36]:

$$\delta\nu_{LS} = -\frac{1}{8\pi}\left(\frac{\delta_0}{\delta_0^2 + (\frac{\Gamma}{2})^2}\right)[g_1^2 - g_2^2], \tag{1.27}$$

where $\delta_1 = \delta_2 = \delta_0$ is the laser detuning, assumed to be equal for both lasers, $\frac{\Gamma}{2}$ the excited state decay rate and g_1 and g_2 the Rabi frequencies of the transitions.
It is obvious from the formula that in the case of two equal Rabi frequencies the light shift vanishes[37].
But if a frequency modulated VCSEL is used not only the two CPT-generating sidebands have to be considered but also the rest of the frequency comb [38].
Considering these the ac-stark-shift affecting each ground state is[39]:

$$\begin{aligned}\delta\nu_1 &= \frac{1}{8\pi}|g_{1n}|^2\frac{(\omega_n - \omega_{31})}{(\omega_n - \omega_{31})^2 + (\frac{\Gamma}{2})^2} \\ \delta\nu_2 &= \frac{1}{8\pi}|g_{2n}|^2\frac{(\omega_n - \omega_{32})}{(\omega_n - \omega_{32})^2 + (\frac{\Gamma}{2})^2}\end{aligned} \tag{1.28}$$

ω_n is the different laser frequencies and g_{2n} the respective Rabi frequencies. ω_{31} and ω_{32} are the transition frequencies between the ground states and the excited state. $\frac{\Gamma}{2}$ is again the excited state decay rate.
The difference between between the two is the resulting light shift[39]:

$$\delta\nu_{LS} = \delta\nu_1 - \delta\nu_2 \tag{1.29}$$

In order to calculate the total light shift a summation over all laser sidebands is necessary. The light shift can be significantly reduced by optimizing the modulation index[40] and it

has been found that for a value of 2.4 the light shift vanishes[39]. Unfortunately ageing of the laser changes the index over time[41] and for many applications, for example our Coupled Dark State Magnetometer amongst other things, the necessary operation parameters just not feasible.

1.4.5 Saturation and Power Broadening

The profile of a absorbing transition is dependent on the intensity of the laser. A sufficiently strong laser pumps a considerable number of atoms to the CPT state, reducing the population of the other state, saturating the transition. This Optical pumping causes additional line broadening [42].
According to [42] the absorption coefficient for a saturated transition is a Lorentzian given by:

$$\alpha_s = \alpha_0 \frac{(\frac{\gamma}{2})^2}{(\omega - \omega_0)^2 + (\frac{\gamma_s}{2})^2} \tag{1.30}$$

with α_0 the unsaturated absorption coefficient and γ_s the saturation broadened linewidth. Hence the absorption is reduced at the middle $\omega = \omega_0$ by a factor of $(\frac{\gamma_s}{\gamma})^2$ due to saturation. This factor gets smaller with distance $\Delta\omega = |\omega - \omega_0|$ from the absorption maximum and approaches zero for inf. Due to this the line is broadened.

1.4.6 Time-Of-Flight Broadening

This broadening is caused by the short interaction time between the Laser and the Rb atom compared to the lifetime of the ground state coherence. In this case the width of the resonance is not governed by the lifetime, but by the flight duration[42].
In the case of a Gaussian laser profile the FWHM is[13]:

$$\Delta\nu_{tof} = \frac{\bar{v}\sqrt{8ln2}}{\pi d} \tag{1.31}$$

$\bar{v}$ is the mean velocity and d the diameter of the laser beam.
Thus the linewidth can be decreased by either reducing the velocity of the atoms, e.g. with a buffer gas or working at a lower temperature, or by increasing the beam diameter.

1.4.7 Lightshift vs Detuning

As can be seen in equation 1.27 on page 23 the light shift is dependent on the laser detuning if the radiation amplitudes of the laser fields are not equal[26]. Its' net-shift as a function of optical detuning has a dispersive shape according to Knappe[43].

1.5 Frequency Modulation Spectroscopy

In Frequency Modulation Spectroscopy (FMS) a modulated laser is used to detect a spectral feature. In this case a measurement signal is generated at the modulation frequency and any noise with a frequency not close to it is eliminated[44]. Thus sensitive detection of narrow spectral features is possible[45].
The explanation of the FMS follows the papers by Bjorklund et al.[45], Supplee et al.[44] and Bjorklund[46].
As in subsection 1.4.3 the modulated laser light is given by equation 1.24 and can be expanded into a series of Bessel functions, characterizing the the frequency components of the light.

$$E = E_0 e^{(j\omega_0 t + \beta \sin(\omega_m t))} = E_0 e^{i\omega_0 t} \sum_{n=-\infty}^{\infty} J_n e^{in\omega_m t} \tag{1.32}$$

In typical FMS the modulation index is very small and hence only a strong carrier and the two first order sidebands make up the frequency comb. All higher-order sidebands are negligible.
The laser light next passes through the sample containing the spectral feature of width Γ. The transmitted field is given by:

$$E_T = E_0 e^{i\omega_0 t} \sum_{n=-1}^{1} T_n J_n e^{in\omega_m t} \tag{1.33}$$

where $T_n = e^{-\delta_n - i\phi_n}$ is the complex transmission function, describing the interaction between the sample and the incident laser light. δ_n is the field amplitude attenuation and ϕ_n is the optical phase shift for the frequency component ω_n.
A photodetector than measures the intensity of the laser light, which is proportional to $|E_T|^2$. Based on the assumption that the absorption and dispersion of the spectral feature is weak $|\delta_0 - \delta_{\pm 1}| \ll 1$ & $|\phi_0 - \phi_{\pm 1}| \ll 1$ the measured intensity is proportional to:

$$|E_T|^2 = E_0^2 e^{-2\delta_0}[1 + \beta(\delta_{-1} - \delta_1)\cos\omega_m t + \beta(\phi_{-1} + \phi_1 - 2\phi_0)\sin\omega_m t] \tag{1.34}$$

where the Bessel functions have been approximated by $J_n \approx \frac{\beta^n}{2^n n!}$, which is viable for small β.
In FMS the modulation frequency is large compared to the width of the spectral feature $\omega_m \gg \Gamma$. Under that condition the cos-component (in-phase-component) of the beat signal is directly proportional to the absorption when the lower or upper sideband are resonant. Whereas the sin-component (quadrature-component) shows the dispersion signal, if either the carrier or one of the sidebands is in resonance.
There is no background heterodyne signal in FM absorption spectroscopy because the rf signal arising from the upper band and the carrier is cancelled out by the rf signal arising from the lower band and the carrier, as long as neither are disturbed. However this prefect cancellation is destroyed, as soon as one of both is attenuated by a spectral feature, leading to the great sensitivity of FMS.

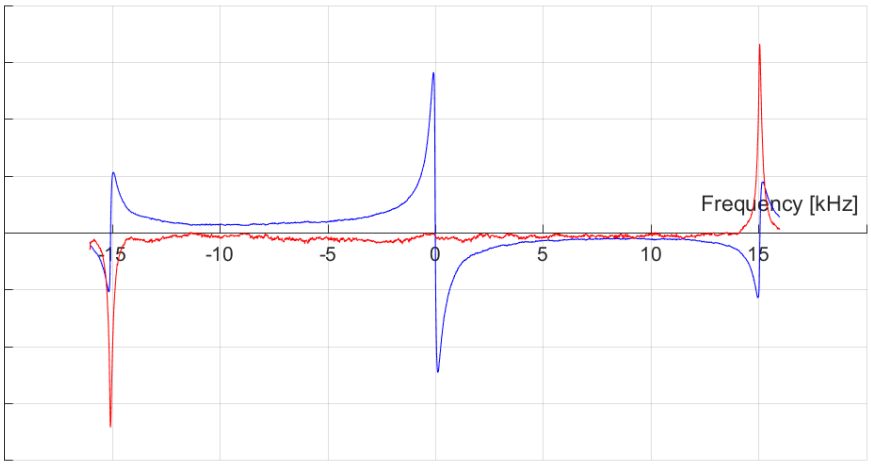

Figure 1.8: In-phase signal (blue) and quadrature signal (red) of a typical CPT measurement with Frequency Modulation Spectroscopy. The modulation frequency ω_m was 30 kHz. Thus, according to 1.34 a dispersion signal is measured at the carrier (0 kHz) and the two sidebands ($\pm$15 kHz) and a absorption signal at both sidebands ($\pm$15 kHz).

1.6 CDSM - Coupled Dark State Magnetometer

The CDSM is a scalar magnetometer for space application currently under development. The first iteration was already successfully tested on a Chinese seismo-electromagnetic satellite [47][48]. Further down the line an updated version will take part in the "JUICE - JUpiter ICy moons Explorer" mission, scheduled for 2022 [49].

1.6.1 DSM - Dark State Magnetometer

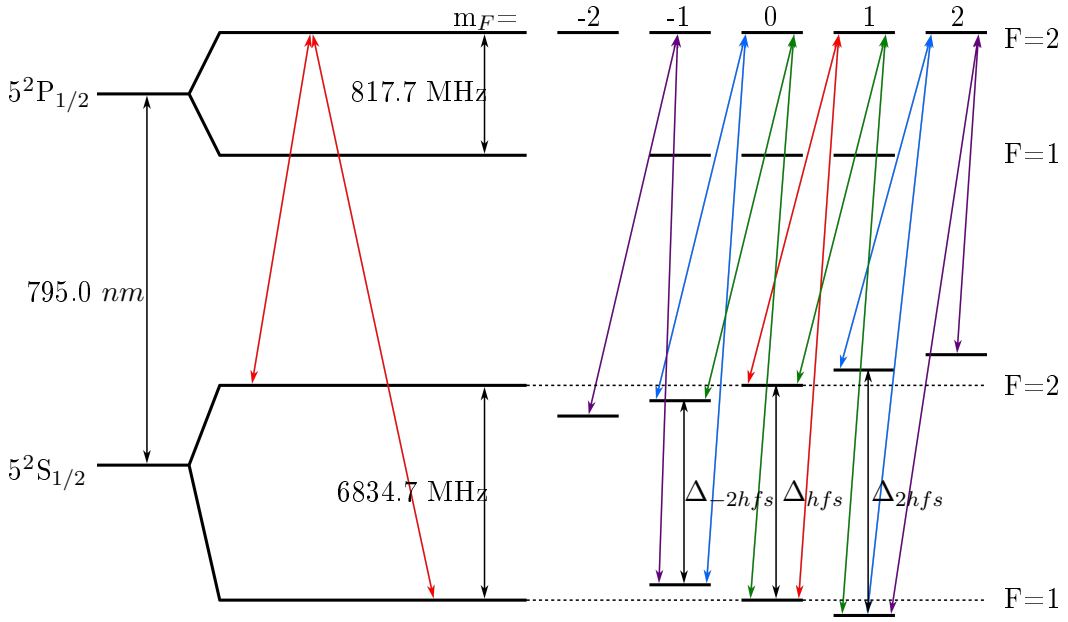

Figure 1.9: ^{87}Rb D_1 line in a magnetic field with possible CPT excitation schemes. Red is the n=0, green the n=±1, blue the n=±2 and violet the n=±3 resonance, where n=m$_{F=1}$+m$_{F=2}$ of the two involved $5^2S_{1/2}$ levels. Δ_{hfs} is the ground state splitting, unaffected by the magnetic field in 1^{st} order perturbation theory. $\Delta_{\pm 2hfs} = \Delta_{hfs} \pm 2\nu_B$ where ν_B is the energy shift introduced by the magnetic field

A magnetic field lifts the degeneracy of the hyperfine ^{87}Rb D_1 line, splitting up the involved states according to their m_F quantum number. The energy shift experienced by the sublevels in 1^{st} order is given by the Breit-Rabi formula[50][51]:

$$\nu_B = \frac{\mu_B}{(2I+h)}[n(g_J - g_I) + 8g_i(m_{F=1} - m_{F=2})g_I]B \tag{1.35}$$

where μ_B is the Bohr magneton, g_J and g_i are the Landé g-factors, I the nuclear spin and n=m$_{F=1}$+m$_{F=2}$.
Thus one can calculate the magnetic field by measuring the dark resonance position of

any of the n=±1,n=±2,n=±3 excitation schemes, denoted in figure 1.9.
Unfortunately any frequency shift, stemming from buffer gas pressure, temperature or intensity, discussed in the previous sections 1.3.1 and 1.4.4, cannot be distinguished from a change in the magnetic field. Hence one has to have either great control over the parameters, affecting the ground state splitting frequency, or exact knowledge about their influence, which is very hard to achieve in both cases.
One further possibility to mend these problems is the CDSM, proposed by Lammeger[52].

1.6.2 CDSM - Coupled Dark State Magnetometer

Instead of measuring just one of the CPT resonances, which are dependent on the magnetic field, two dark states are probed at the same time and their energy difference is measured. Thus any systematic effects, that affect both states the same, are cancelled out.
In order to do so the laser light is first modulated by $\frac{1}{2}\Delta_{hfs}$, determined by measuring the magnetic field independent n=0 resonance depicted in 1.9, and then a second modulation is added. Its' frequency is scanned through till either the n=±1,n=±2 or n=±3 resonances are excited too. If n=±1 or ±2 are established, this frequency correspond to ν_B, in the case of n=±3 it is $2\nu_B$. Hence three dark states are established at once.

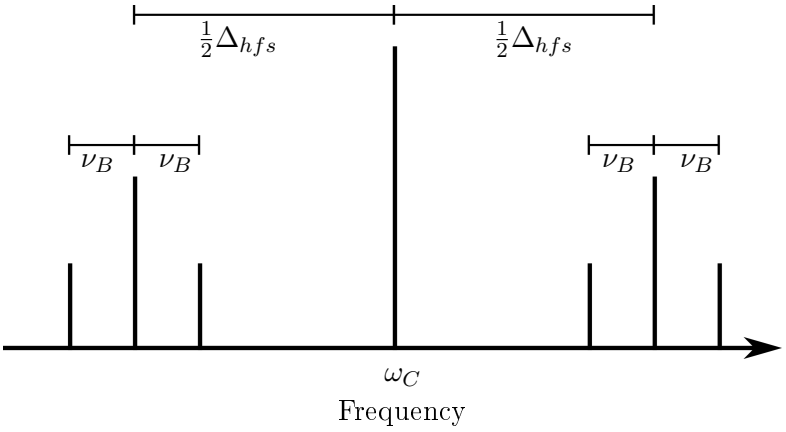

Figure 1.10: Schematic of the laser spectrum necessary for the Coupled Dark State Magnetometer. In the case of ^{87}Rb D_1 Λ_C=795 nm, Δ_{hfs}=6.8 GHz and ν_B dependent on the magnetic field.

2 Experimental Setup

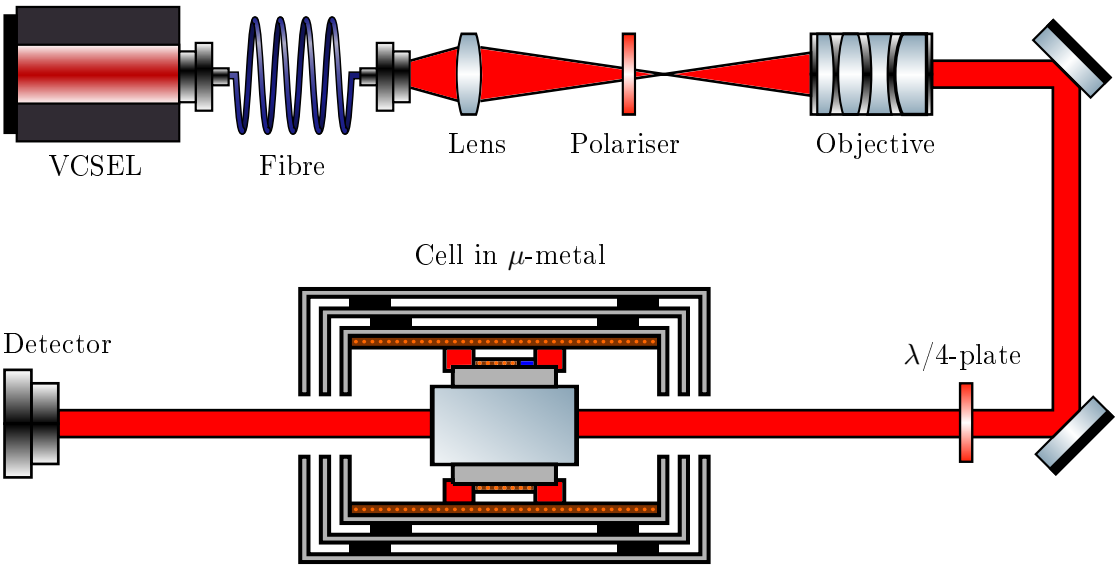

Figure 2.1: VCSEL: 795 nm VCSEL from Oclaro
Fibre: Polarisation Maintaining Single Mode Fibre
Lens: f = 200 mm
Polariser: Glan-Thompson Prism
Objective: f = 70 - 210 mm
$\lambda/4$-plate: Zero-order $\lambda/4$-plate
Cell in μ-metal: ^{87}Rb-cell shielded from stray magnetic fields with 3 layers of μ-metal.
Detector: 1830-C Optical Power Meter

Laser-light, produced by a VCSEL, is first guided through a single-mode polarization maintaining glass fibre. After leaving the glass fibre the light passes a f = 200 mm lens which focuses the laser beam at the focal point of an objective. Its focal length can be varied between 70 mm and 210 mm, thus allowing for an easy variation of the beam profile without ruining the collimation. After two dielectric layer coated mirrors (for easier adjustments) the light passes the ^{87}Rb-cell.
The cell is placed within a aluminium ring, which is equipped with a PT-1000 and a heating wire. This arrangement in turn is fixed with two plastic rings inside a magnetic coil. A bias DC magnetic field of 6 µT is applied to lift the degeneracy of the transition and the setup is shielded from external magnetic fields with 3 layers of µ-metal.

The resulting signal is detected by a "1830-C Optical Power Meter" and further processed by a lock-in-amplifier.
Along the way the light gets first linearly polarized by a Glan-Thompson Prism, positioned between the lens and objective, and later circular polarized by a quarter-wave-plate, positioned in front of the cell.

2.1 VCSEL - Vertical-Cavity Surface-Emmiting Laser

A 795 *nm* VCSEL from Oclaro was used, modulated by a microwave signal generator "R&S SMR20" from Rohde-Schwartz. The oscillator uses the rubidium-based atomic clock "SRS MODEL FS25" as external reference.
The operation principle of a VCSEL and in-depth discussion of modulation can be found in 1.4 on page 19.

2.1.0.1 Laser settings

The coarse adjustment of the laser current was made by looking at the absorption spectrum of the ^{87}Rb-cell and setting it to the $5^2S_{1/2}$ F=1 to F=2 transition. Directly before a measurement the laser was more accurately fine-tuned by setting it to a current value that maximized the CPT-resonance amplitude. This was necessary because there was no external frequency stabiliser, but for a typical measurement time the laser remained stable enough.

2.2 Beam Profile: Setting and Determination

2.2.1 Setting

After the laser beam left the glass fibre, its focus was set to be congruent with the focus point of the objective, with a 200 mm lens as can be seen in figure 2.1. With this setup the beam profile could be fluently set between 4 mm^2 and 34 mm^2 by changing the focal length of the objective.
The collimation was checked by taking two pictures of the laser beam 20 cm apart and determining the beam width. Unfortunately for some settings the beam profile varied by 5 percent over this distance.

2.2.2 Determination

The beam profile was determined by first taking a picture of the laser with a reflex camera without its objective. The pixel values of the picture matrix, after it was converted to "black and white", were then summed up along each row as well as each column. The resulting two bar charts were then fitted with a gauss-curve

$$f(x) = B * \exp(\frac{-(x - x_0)^2}{2\sigma^2}) + C \tag{2.1}$$

and the two resulting σ were used to calculate the area of the laser utilising the ellipse area formula.

$$A = \pi ab \quad a = 2\sigma_1 \quad b = 2\sigma_2 \tag{2.2}$$

As cut-off point for the laser beam D4$\sigma = 4\sigma$ was chosen, what is equivalent to $\frac{1}{e^2}$ in the case of a perfect Gaussian beam. Knowing the size of the camera sensor the area value could be converted into millimetres and the intensity calculated.
This was all done with a self-made program.

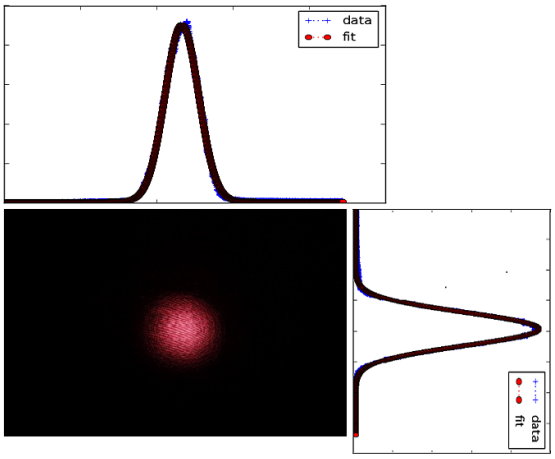

Figure 2.2: Beam profile determination: picture of the laser with the gauss-fits in x and y-direction. The beam was in all cases nearly perfectly circular. This technique works best with single-mode-fibers (as in this case), but the code has been updated to also work with more complicated mode-patterns.

At the start, in order to confirm the results of the aforementioned technique, the beam width was also measured with a manual scanning slit. The two measurements yielded the same results within the standard error, but compared to the manual scanning slit the camera approach is much faster and leaves less room for human error. Furthermore the pictures of the laser are also convenient to check for any adjustment errors by revealing if parts of the laser have been cut off.
The error of the procedure was estimated by taking several pictures of the beam profile while the configuration of the experiment remained the same. In between the pictures the camera was removed and then reinstalled. The results led to a rounded up standard error of $\pm 1\ mm^2$ for the area.

2.3 Frequency Modulation

The VCSEL was frequency modulated twice. Once with a GHz-modulation of 3.4 Ghz in order to create the sidebands, necessary for CPT-detection, and a second time with a kHz-modulation for Frequency Modulation Spectroscopy, discussed in section 1.5.

2.3.1 GHz Oscillator

The signal generator "R&S SMR20" from Rohde-Schwartz, with a rubidium-based atomic clock as external reference, was used for GHz-modulation.
The later presented measurements were done by sweeping the modulation frequency around the vicinity of the CPT-resonance in 2 Hz steps. This was done with a in-house-written computer program.
Except for the measurements in 3.5 the strength of the modulation was set at -0.7 dBm microwave power.

2.3.2 Lock-In amplifier

The used model was the "SR830 DSP Lock-in Amplifier" from Stanford Research Systems. For all measurements it was operated at a frequency of 15 kHz. The phase of the amplifier had to be adjusted from time to time. This device again was controlled by the in-house written computer program.

2.4 Determination of amplitude, width and position of the resonance

The measured data was analysed by a self-written computer program. It fits a straight line through the centre and a square function through the maximum as well as the minimum of the characteristic resonance. For the maximum fit only the data, that was greater than 0.95 times the maximum measured value, was used, for the minimum the data smaller than 0.95 times the minimum and for the centre only the measuring data stretching from 0.1 to -0.1 times the maximum value. These values were reached by trial and error: different percentages were tried for a random subset of measurements and the ones that worked best, were subsequently used for all.
The width of the resonance was defined as the frequency range between the maximum and the minimum of the respective fits, the CPT-resonance amplitude as the height difference between the two. The fit-found zero-crossing is called the ν_{00} frequency of the transition.

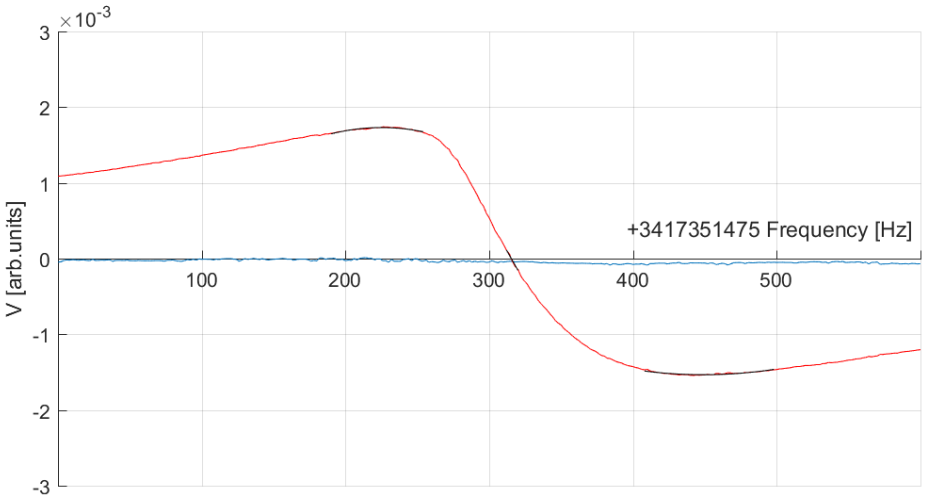

Figure 2.3: CPT-resonance with fits to determine the ν_{00}-frequency, maxima and minima.
ν_{00}-frequency: 3417351790 Hz
Maxima: 3417351700 Hz, 0.0017 arb.units
Minima: 3417351924 Hz, -0.0015 arb.units

2.5 Rubidium-cells

15 cylinder-shaped glass cells, that differ in Neon-buffer-gas-pressure, and one, filled with a mix of Argon and Nitrogen, were available for the experiments.
The pressure for the neon-cells was determined with the equation 1.19 on page 16.

$$\delta\nu_{BG} = P_0[\beta_0 + \delta_0(T - T_0) + \gamma_0(T - T_0)^2] \tag{2.3}$$

The temperature dependence was neglected because its influence on the resonance frequency is very small compared to the buffer-gas frequency-shift, and for the pressure coefficient $\frac{\beta}{\nu_0} = 57.4\ \frac{10^{-9}}{\text{Torr}}$ was used from Bender[21]. $\delta\nu_{BG} = |2\nu_{00} - \nu_0|$ is the difference between the unperturbed $5^2S_{1/2}$ F=1 $\rightarrow$ F=2 transition ν_0=6.8347 Ghz and ν_{00} determined at a cell temperature of 35 °C and laser-intensities between $2.0 \pm 0.2\ \frac{\mu W}{mm^2}$ and $2.5 \pm 0.2\ \frac{\mu W}{mm^2}$. The measured ν_{00} of the disturbed atom has to be doubled because one measures half the transition frequency if the sidebands are used to create the CPT-resonance, as in this case.

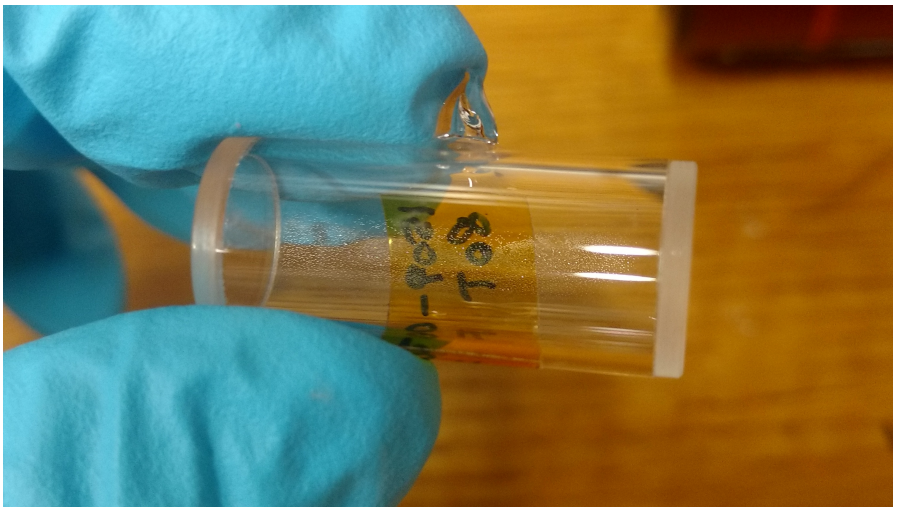

Figure 2.4: Cell filled with Rubidium 87 and Neon. All cells were of identical size: Length = $27mm$; Diameter = $12mm$

2.5.1 List of available Rubidium-cells and experiments done with them

Table 2.1: List of available Rubidium-cells and experiments done with them

Pr	Buffer-Gas-Pressure
T	Temperature Measurement
LW	Laser Width Measurement
Att	Attenuator Measurement
2Pd	Two-Photon Detuning Measurement
dBm	Power Variation

Name	Pr [Torr]	T	LW	Att	2Pd	Dbm
15NE-Special-1	7.5	✓	✓	×	✓	×
15NE-Special-2	7.7	✓	✓	×	×	×
30NE-Special-1	14.9	✓	✓	✓	×	×
30NE-Special-2	16.4	✓	✓	×	✓	×
60NE-Special-1	31.6	✓	✓	×	×	×
60NE-Special-2	31.4	✓	✓	×	×	✓
100NE-Special-1	48.7	✓	✓	×	×	×
100NE-Special-2	52.9	✓	✓	✓	✓	×
120NE-Special-1	54.0	✓	✓	×	×	×
120NE-Special-2	53.7	✓	✓	×	✓	×
1509-001	55.0	✓	✓	×	×	×
1509-002	55.3	✓	✓	×	✓	×
1509-003	40.1	✓	✓	×	×	×
1509-004	37.6	✓	✓	×	×	✓
1509-005	51.2	✓	✓	×	×	×
Special T		✓	✓	×	×	×

As can be seen the calculated pressure differs greatly from the nominal pressure of the cells. The desired pressure is for the first 10 given in the name and for the 1509-00x cells it should have been around 80 Torr. It is in all instances about half of what it is supposed to be, which suggests that there is a systematic problem with the suppliers production method of the cells.
First the evacuated glass cell is connected to a tank, whose pressure is set to the wanted value, via a glass straw. This connection is later melted off. If this happens too close to the cell, the cell heats up during the procedure and thus the pressure within the cell is reduced. This can be prevented by first melting the straw off further away from the cell, waiting till it is cool again and only then shortening it to the length, that can be seen in figure 2.4. In this case the number of particles in the cell stay approximately the same during the melt-off-process.
A further improvement could be made by immersing the cell in water-bath, in order to further stabilise the cell temperature.

In the following sections only the results of the Neon-buffer-gas cells are compared and discussed. The measurements for the Argon-Nitrogen cell are only presented in 6.

2.5.2 Heating strategy

A heating wire heated an aluminium ring, which in turn warmed up the cell. The temperature was measured with a PT-1000 glued to the aluminium ring. Hence we waited 3 minutes before we assumed that the cell also had the desired temperature.
During the intensity experiments the applied voltage corresponding to the desired temperature was adjusted by hand. The heating was constantly turned on because no measurable influence on the ν_{00}-resonance was found.
During all other experiments the temperature was set using an computer and a voltage source, utilizing a two-point-method. The voltage source was turned on till the desired temperature was reached, then remained turned off till the temperature dropped 0.1 °C below the set temperature. Thus during a measurement the heating repeatedly turned off and on, but yet again no influence on the measured data was found.

3 Parameter Studies

First the buffer-gas-pressure of each cell was identified by measuring their ν_{00}-resonance and using the equation 1.19 on page 16. Afterwards the behaviour of the ν_{00}-resonance was determined in regards to different parameters. Only one parameter was changed at a time while all others remained constant.
All measurements can be seen in the Appendix starting on page 73.
If are fit-parameters are shown they are displayed until the first significant digit.

3.1 Buffer-gas-pressure

The measurements of section 3.2 done at the temperature of 35 ℃ were used to calculate the pressure of the individual cells and to discuss its influence on amplitude and width of the measured curve. The laser-intensity varied from measurement to measurement between 2.0 ± 0.2 $\frac{\mu W}{mm^2}$ and 2.5 ± 0.2 $\frac{\mu W}{mm^2}$ due to re-alignment of the whole experimental setup.

Table 3.1: Settings: Buffer-gas-pressure

Cell temperature		35 ℃
Intensity		2.0-2.5 $\frac{\mu W}{mm^2}$
GHz oscillator	Power	0.7 dBm
	Increment	2 Hz
Lock-In amplifier	Modulation Frequency	30120 Hz

3.1.1 ν_{00}-drift

The frequency of the ν_{00}-transition is highly dependent on the used buffer-gas and its pressure. Compared to the other here treated parameters it is by far the largest influence on the position of the transition. Thus the transition frequency can be used to calculate the buffer-gas-pressure to a suitable accuracy. According to [21] Neon should have a positive shift coefficient $\frac{\beta}{\nu_0}$ of 57.4 $\frac{10^{-9}}{\text{Torr}}$, inserted into the formula 1.19 this leads to the buffer-gas-pressures presented in table 2.1 on page 36.

3.1.2 Amplitude and Width

Figures 3.1 and 3.2 show that the CPT-resonance amplitude as well as the width of the measured curves decrease linearly with pressure. This results in figure 3.3, where no distinct correlation between neon-pressure and amplitude to width ratio can be observed.

Furthermore it can be seen, that sometimes cells with almost the same neon-pressure yield very different results in terms of amplitude and width. This could either be caused by different laser-intensities, the positioning of the cell (causing interference effects) or problems concerning the cells itself, e.g. Rubidium deposits on the cell windows.
The difference in laser-intensities were caused in part by laser fluctuations, but mainly by re-adjustments of the experimental setup, which unfortunately was necessary from time to time, due to mishaps and because parts of the setup where needed elsewhere. Yet no discernible pattern emerged between amplitude or width with respect to these involuntary intensity changes.
When the unmodulated laser-frequency was swept through the Rubidium absorption spectrum of a cell a sinus wave layering the spectrum could be observed. This sinus wave changed in height and moved along the frequency axes when positioning of the cell was altered, but it never vanished for any of the possible positions. It is probably caused by interference effects at the coplanar glass fronts of the cell and could explain the different results for cells with almost identical Neon-pressure.
Furthermore Rb atoms deposit on the glass of the cell at lower temperatures as can be seen in figure 2.4. As well the extent as the exact position is different from cell to cell and could also explain the difference in signal strength.

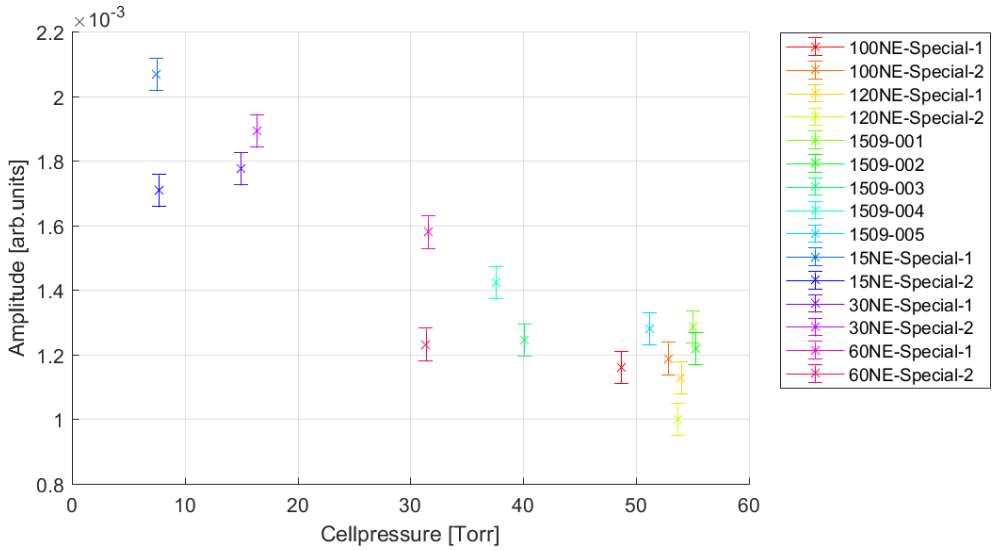

Figure 3.1: Signal amplitude of the individual cells.
Settings in table 3.1 on page 38.

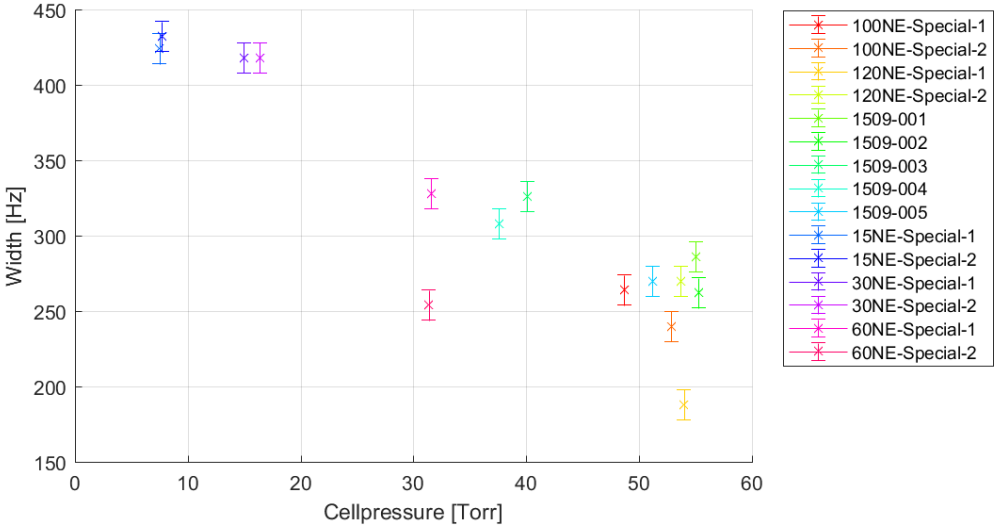

Figure 3.2: Signal width of the individual cells.
Settings in table 3.1 on page 38.

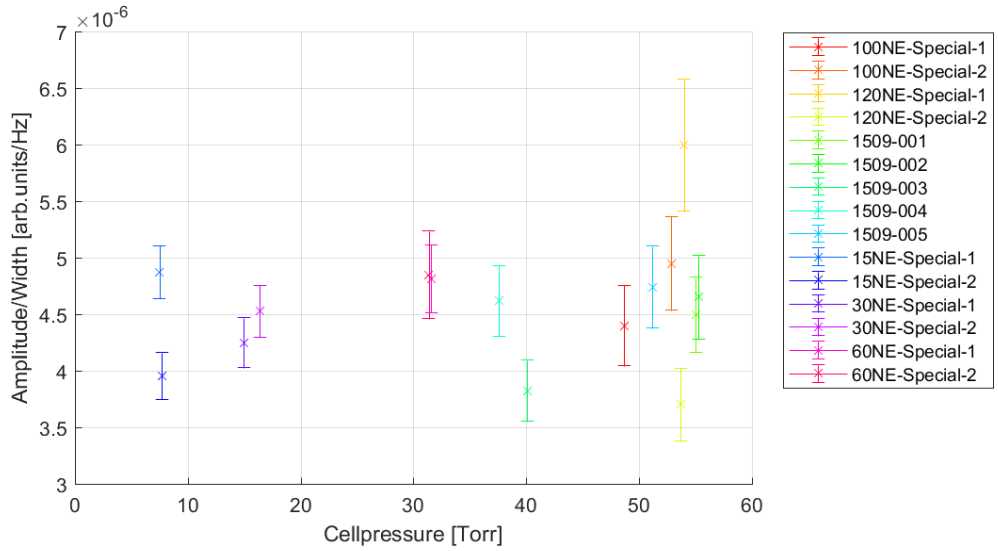

Figure 3.3: Amplitude-width-ratio of the individual cells.
Settings in table 3.1 on page 38.

3.2 Cell temperature

The cell was heated to a certain temperature, left there for about 3 minutes to make sure the whole cell had the desired temperature and then the ν_{00}-resonance was usually measured two times in quick succession. Measurements were done for every available cell starting from either 30 ℃ or 35 ℃ in 5 ℃ steps up to a maximum of 60 ℃.
The beam profile was determined one time before a measurement series and the laser power was identified in front of and after the cell for every temperature. Generally the intensity was set between 2.0 ± 0.2 $\frac{\mu W}{mm^2}$ and 2.5 ± 0.2 $\frac{\mu W}{mm^2}$ in front of the cell.
These measurements (see figures 3.4 and 3.5 on page 42 and Appendix 6) were used to analyse the drift, the amplitude and the width of the resonance in respect to temperature. Especially the ratio from amplitude to width is important to determine the optimal operating temperature.

Table 3.2: Settings: Cell temperature

Cell temperature		30 - 60 ℃
Intensity		2.0-2.5 $\frac{\mu W}{mm^2}$
GHz oscillator	Power	0.7 dBm
	Increment	2 Hz
Lock-In amplifier	Modulation Frequency	30120 Hz

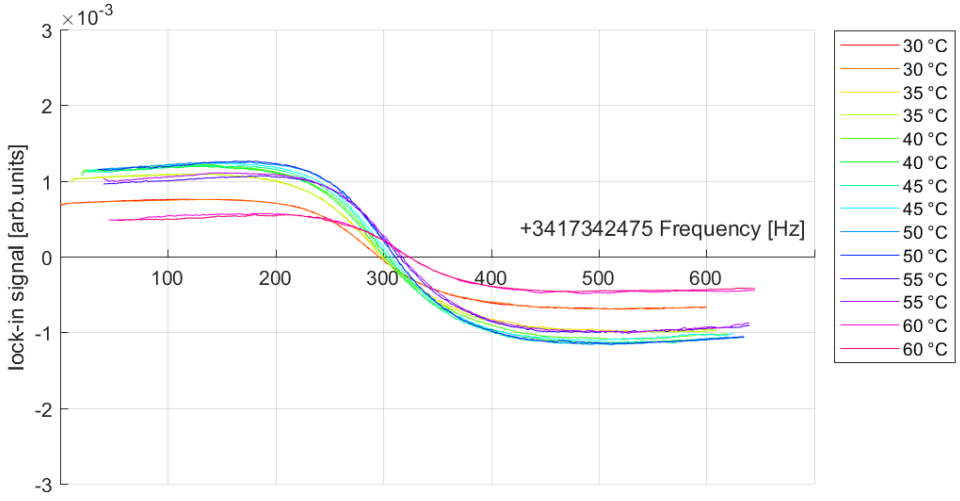

Figure 3.4: Temperature-dependence of cell 15NE-Special-1 - 7.5 Torr.
Settings in table 3.1 on page 41.

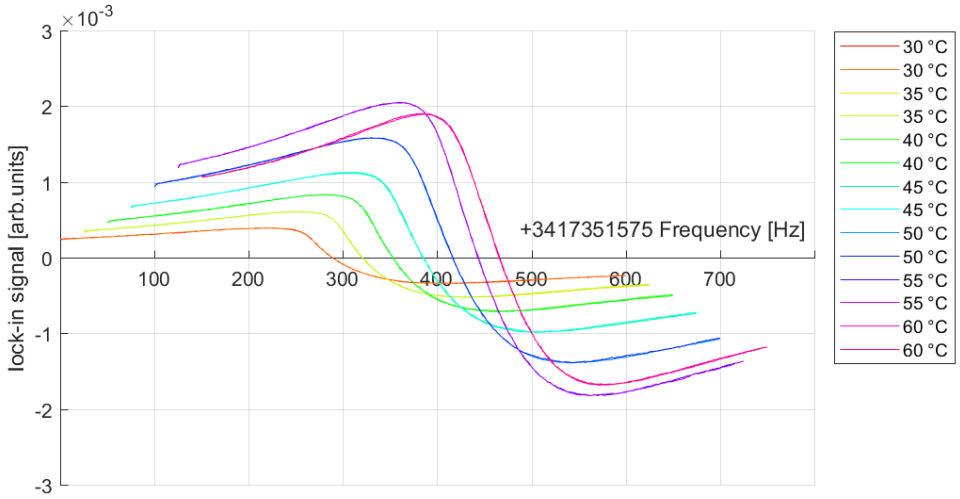

Figure 3.5: Temperature-dependence of cell 120NE-Special-1 - 54.0 Torr.
Settings in table 3.1 on page 41.

3.2.1 ν_{00}-drift

A quadratic fit was fitted through the position of the ν_{00}-resonance. From the fit parameters values the buffer-gas-frequency-shift of neon was calculated.
As can be seen in figures 3.6 and 3.7 on page 43 both the 7.5 Torr cell and the 54.0 Torr cell have a positive ν_{00}-drift with respect to temperature, but nevertheless the behaviour is distinctly different for the two cells. The fit for 15NE-Special-1 yields a linear slope of -0.7 $\frac{Hz}{°C}$ and a quadratic one of 0.02 $\frac{Hz}{°C^2}$ while the fit for 120NE-Special-1 yields 9.2 $\frac{Hz}{°C}$ and -0.04 $\frac{Hz}{°C^2}$, respectively, resulting in a much larger total ν_{00}-drift per °C.
In figures 3.8 and 3.9 a similar behaviour can be observed for all other cells: the quadratic portion decreases while the linear one and the net-drift increases with respect to buffer-gas-pressure.
Yet compared to the effect in chapter 3.1 it is rather small.

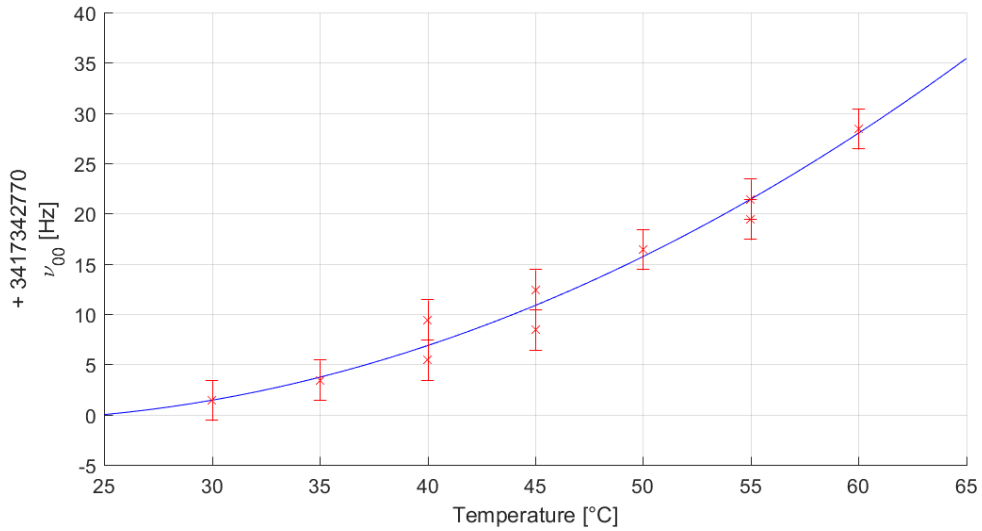

Figure 3.6: ν_{00}-drift of cell 15NE-Special-1 - 7.5 Torr:
$\nu_{00}drift(T) = -0.7T + 0.02T^2$.
Settings in table 3.1 on page 41.

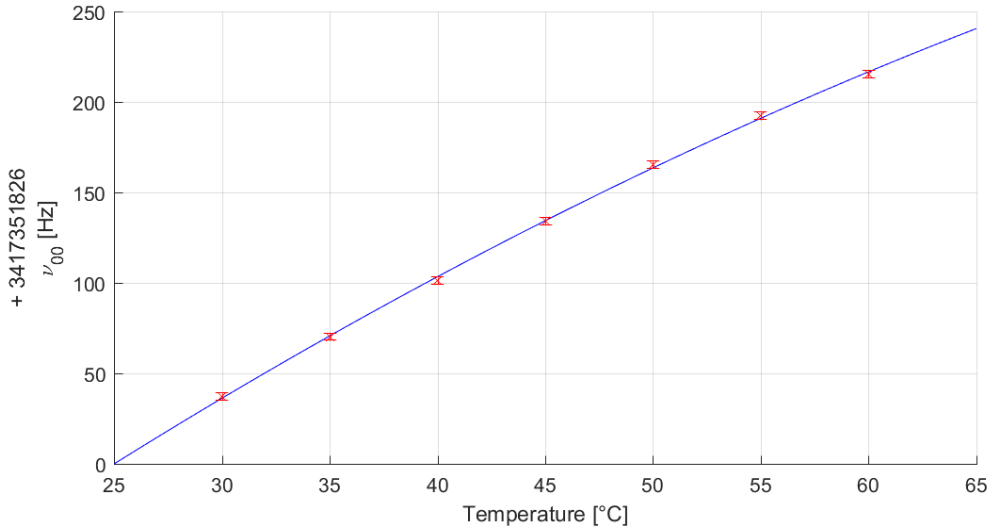

Figure 3.7: ν_{00}-drift of cell 120NE-Special-1 - 54.0 Torr:
$\nu_{00}drift(T) = 9.2T - 0.04T^2$.
Settings in table 3.1 on page 41.

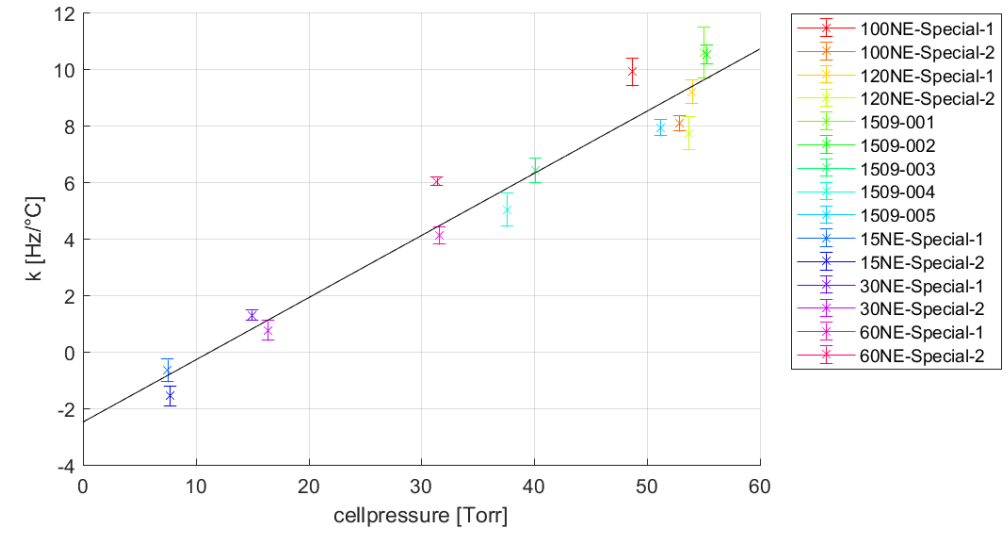

Figure 3.8: Linear Slope of ν_{00}-drift for all available cells:
$k(P) = 0.2198P - 2.4842$.
Settings in table 3.1 on page 41.

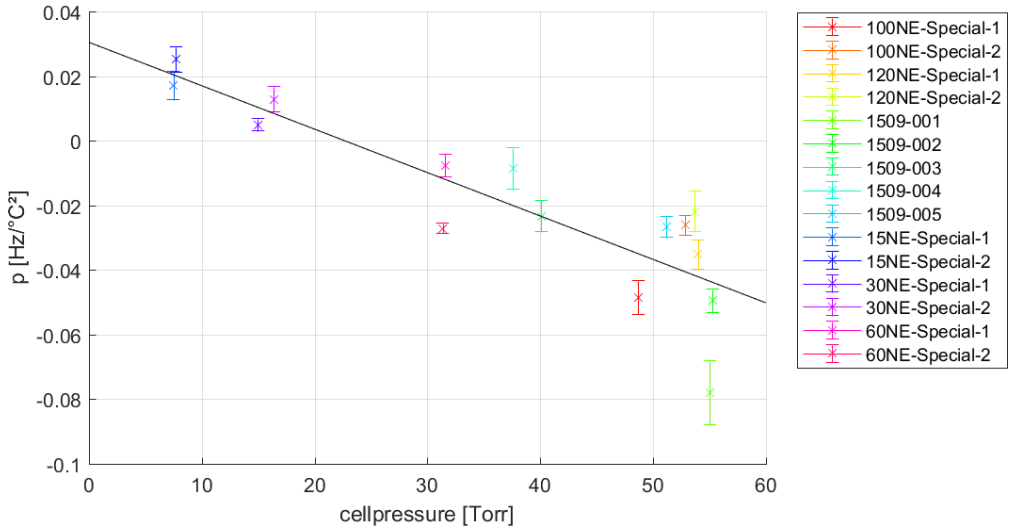

Figure 3.9: Quadratic Slope of ν_{00}-drift for all available cells:
$p(P) = -0.0013P + 0.0304$.
Settings in table 3.1 on page 41.

Considering the figure above 3.9 at a buffer-gas-pressure of around 25 Torr the temperature dependence of the resonance should be an exclusively linear one.

3.2.1.1 Neon buffer-gas-frequency-shift

From the fit parameters presented in figures 3.8 and 3.9 $\frac{\delta}{\nu_0}$ and $\frac{\gamma}{\nu_0}$, discussed in subsections 1.3.4 (page 17) and 1.3.1 (page 15), were calculated. This was done with the formulas $\frac{\delta}{\nu_0} = \frac{2k}{\nu_0 P_0}$ and $\frac{\gamma}{\nu_0} = \frac{2p}{\nu_0 P_0}$. These were derived by considering equation 1.19, and the fact that only half the frequency shift is measured with this experimental setup.

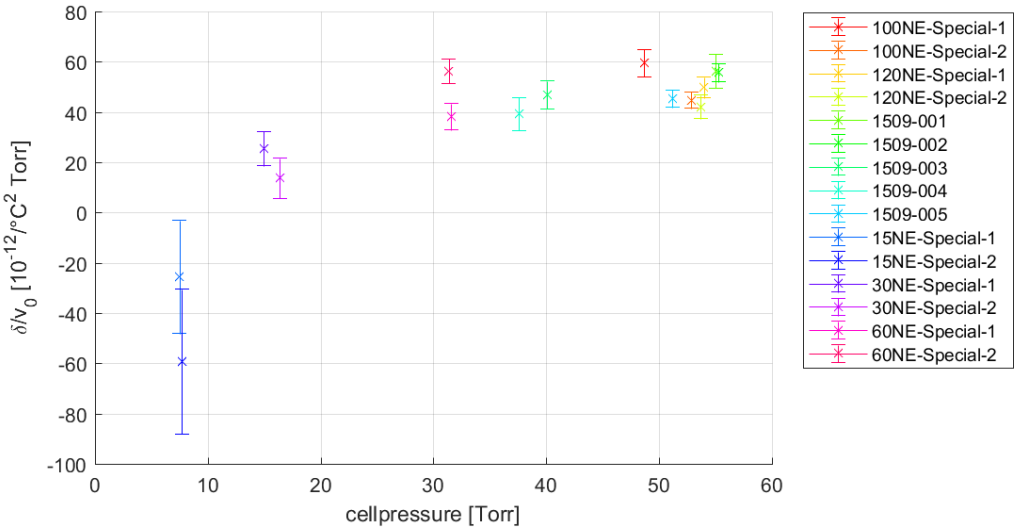

Figure 3.10: Linear temperature coefficient $\frac{\delta}{\nu_0}$ of all available cells.
Settings in table 3.1 on page 41.

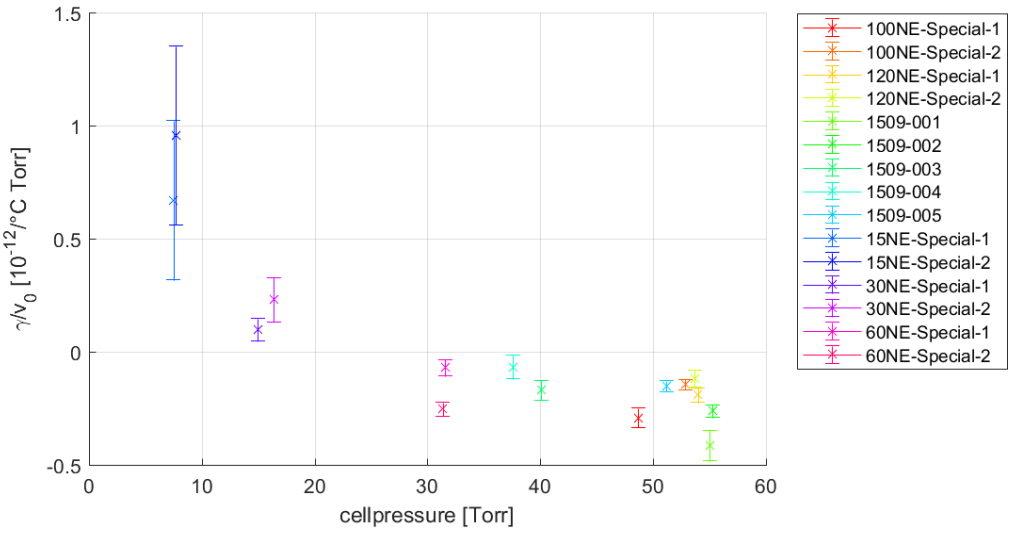

Figure 3.11: Quadratic temperature coefficient $\frac{\gamma}{\nu_0}$ of all available cells. Settings in table 3.1 on page 41.

As can be seen both, $\frac{\delta}{\nu_0}$ and $\frac{\gamma}{\nu_0}$, rapidly change until approximately 30 Torr neon-pressure. Afterwards both stay more or less constant. Taking the average over all cells with a neon pressure greater than 30 Torr a linear temperature coefficient of 48.5±7.5 $\frac{10^{-12}}{℃Torr}$ and a quadratic temperature coefficient of -0.2±0.1 $\frac{10^{-12}}{℃^2Torr}$ were calculated.
Compared to the coefficients presented in tabular 1.1, the linear part calculated here is higher, but even the values found in the literature are far spread. This would suggest that other experimental parameters influence the temperature dependence.
For the quadratic part no literature values were found.
With these two coefficients the inversion temperature, where a change in temperature hardly alters the transition frequency, was found at around 125 ℃. Unfortunately no measurements could be done at such high temperatures because the available cells are already opaque there.

3.2.2 Amplitude and Width

The temperature to maximize the amplitude-width-ratio is dependent on the buffer-gas-pressure of the cells. For example, the best ratio for 15NE-Special-1 (figure 3.12) was found at 50±2.5 ℃, while the best for 120NE-Special-1 was found at 55±2.5 ℃(figure 3.13). It has to be said that for some cells with higher buffer-gas-pressure the absolute maximum of the amplitude-width-ratio was not found, because it is somewhere in the 60 ℃+ region and unfortunately such high temperatures could not be reached with our set-up. Nevertheless from figure 3.16 it can be seen that the ratio improves with gas-pressure, even when just using the available data. Comparing figure 3.15 to the measurements done at 35 ℃(3.2) one finds that the width of the resonance only improves very little and that the pressure-dependent tendency more or less stays the same. The measured

amplitude, on the other hand, increases three to fourfold for higher-buffer-gas cells while it only increases a little bit for cells with lower buffer-gas-pressure, reversing the slope of the curve, as can be seen in figures 3.14 and 3.2.
A fairly similar temperature-dependency was found by Knappe[50]: The width stays approximately the same, while the amplitude first increases due to the increased numbers of atoms that can be pumped into the dark state and later decreases because of the optical thickness effect.
Considering chapters 3.1 and 3.2 the amplitude-width-ratio and the position of the transition are more stable for lower buffer-gas cells, but for the other cells much higher ratios are possible if the the correct temperature is chosen.

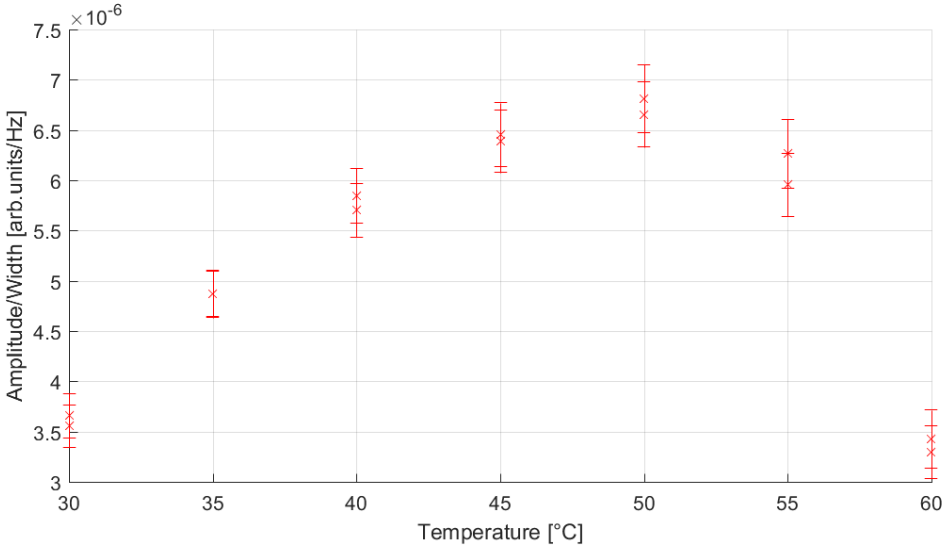

Figure 3.12: Amplitude-width-ratio with respect to temperature for cell 15NE-Special-1 - 7.5 Torr.
Settings in table 3.1 on page 41.

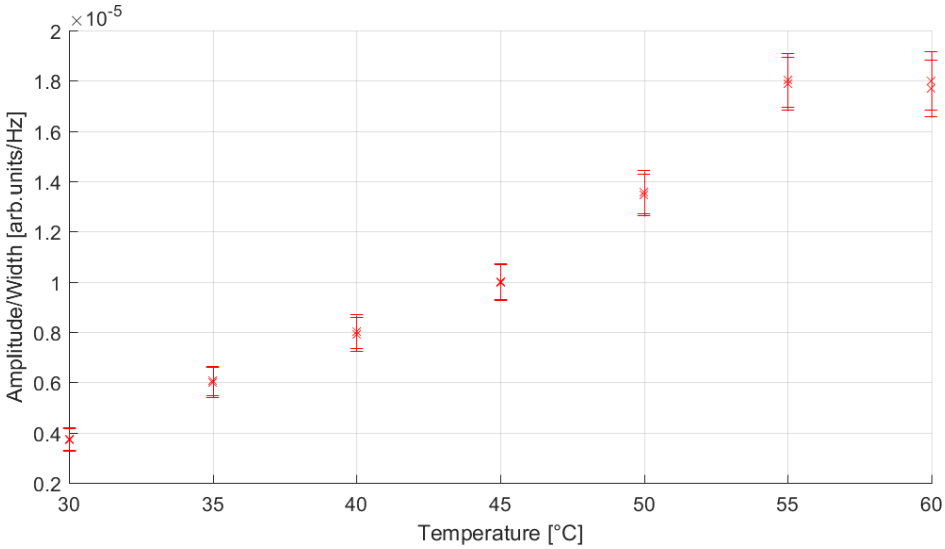

Figure 3.13: Amplitude-width-ratio with respect to temperature for cell 120NE-Special-1 - 54 Torr.
Settings in table 3.1 on page 41.

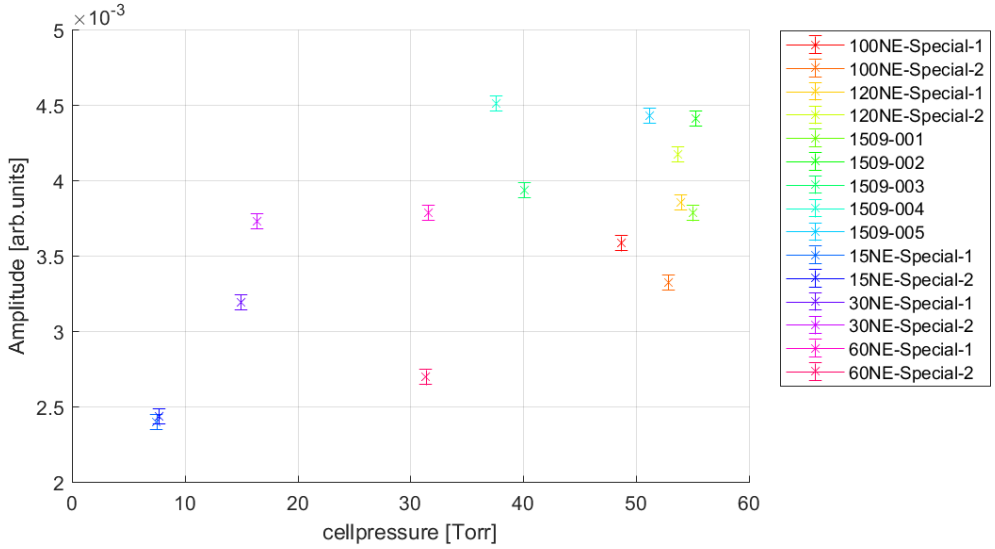

Figure 3.14: Amplitude corresponding to highest achieved amplitude-width-ratio for all cells.
Settings in table 3.1 on page 41.

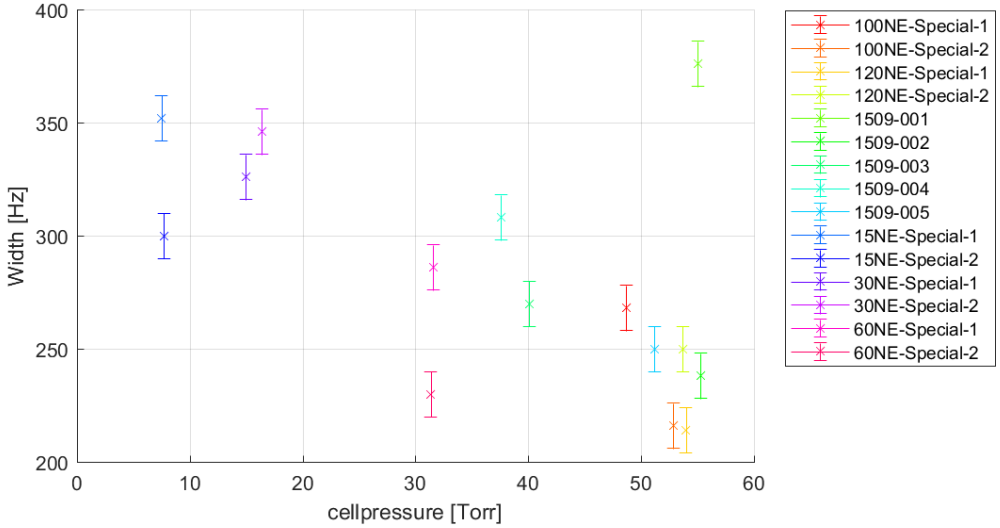

Figure 3.15: Width corresponding to highest achieved amplitude-width-ratio for all cells.
Settings in table 3.1 on page 41.

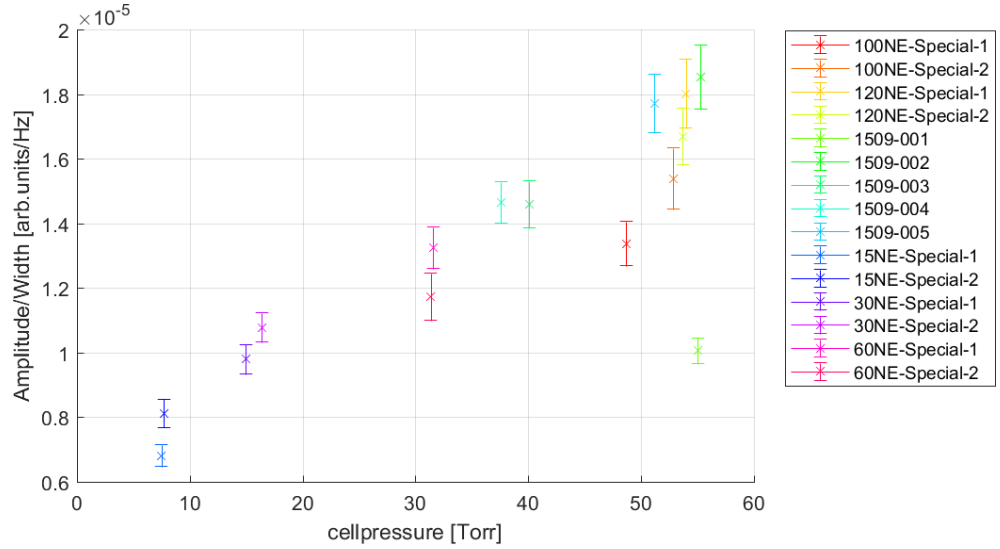

Figure 3.16: Highest achieved amplitude-width-ratio for all cells.
Settings in table 3.1 on page 41.

3.3 Laser intensity

The Laser intensity was either varied by changing the beam profile using the objective or reducing the laser power with an attenuator, placed between the two mirrors. All available cells were measured with the laser-width-method while only two cells were measured with the other.
The temperature of the cells was 35 ℃ during the experiments.

3.3.1 Laser intensity: Laser width

The beam profile could be changed by changing the focal length of the objective, see figure 2.1 on page 29. With this method the beam profile could be varied between 4 to 34 mm^2 without changing the collimation of the laser too much. The resonance was measured at the maximum possible intensity, the minimum and five intermediate steps, two times each. For every step the position of the µ-metal and the mirrors was readjusted to let a maximum of the power through. This was necessary because changing the focal length also slightly changed the path of the laser. The beam profile as well as the power of the laser were determined right in the front of the cell for every step once. During the experiments the temperature was kept at 35 ℃.

Table 3.3: Settings: Laser width

Cell temperature		35 ℃
Intensity		1.0-8.0 $\frac{\mu W}{mm^2}$
GHz oscillator	Power	0.7 dBm
	Increment	2 Hz
Lock-In amplifier	Modulation Frequency	30120 Hz

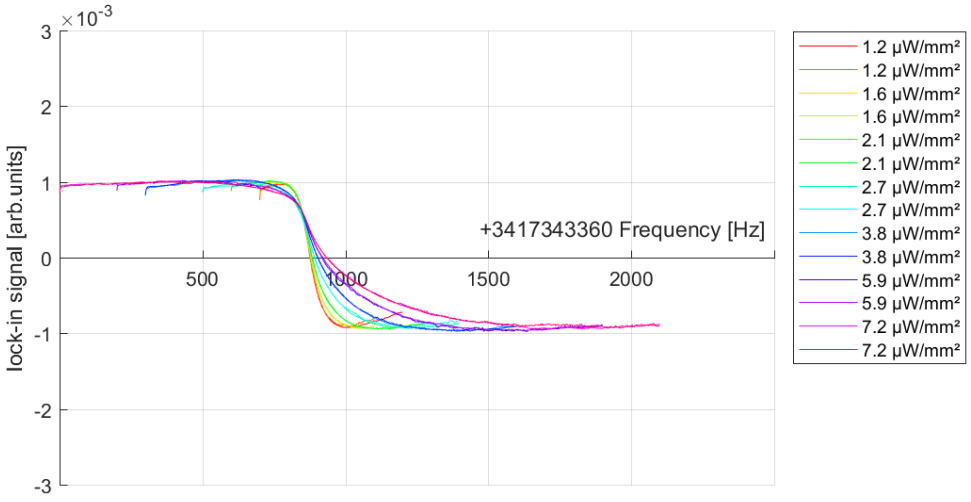

Figure 3.17: Intensity-dependence of cell 30NE-Special-1 - 14.9 Torr.
Settings in table 3.3 on page 50.

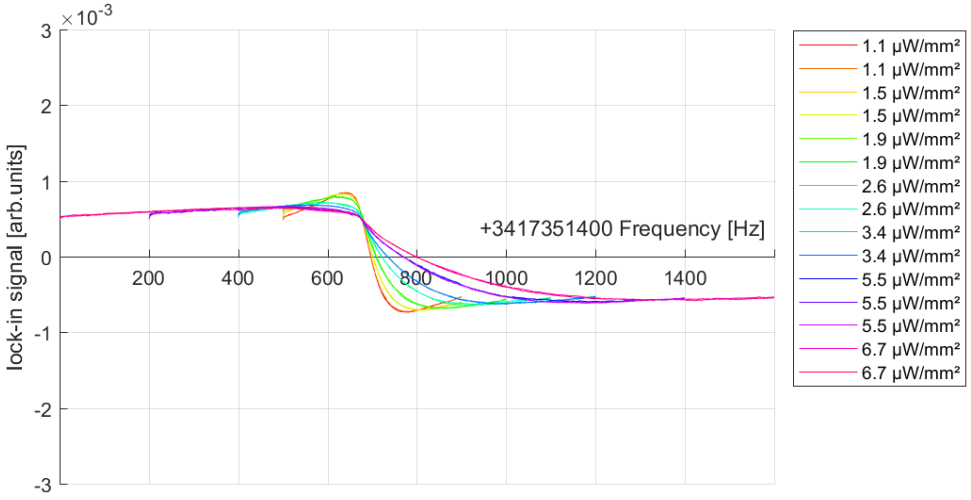

Figure 3.18: Intensity-dependence of cell 1509-001 - 55.0 Torr.
Settings in table 3.3 on page 50.

3.3.1.1 ν_{00}-drift

The position of the resonance has a positive linear drift in respect to intensity for all cells. This behaviour is expected from the theory for a two-level atom and also holds true for real atomic systems at high intensities, which are given here[50]. A similar behaviour was

also found by Merimaa et al[10]. Furthermore the slope increases with Neon-gas-pressure as can be seen in 3.21.

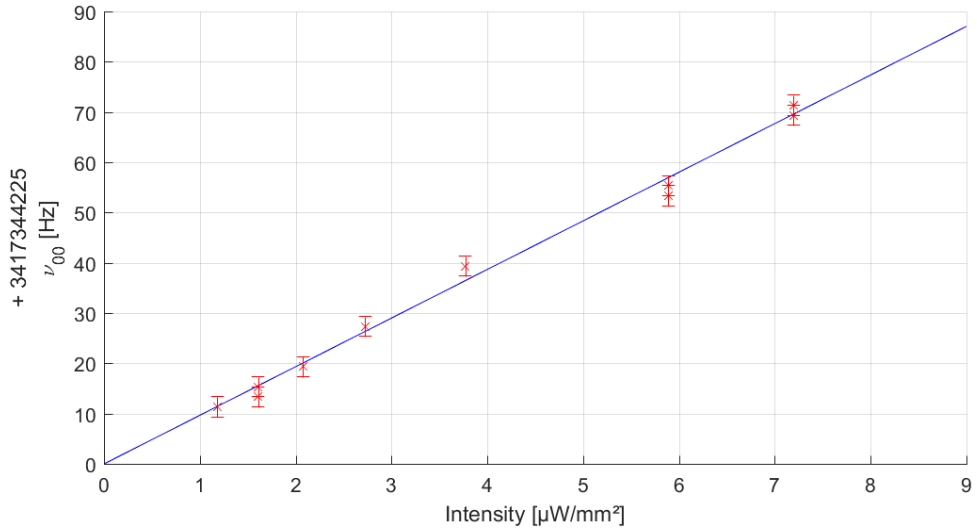

Figure 3.19: ν_{00}-drift of cell 30NE-Special-1 - 14.9 Torr:
$\nu_{00}drift(I) = 9.7I$.
Settings in table 3.3 on page 50.

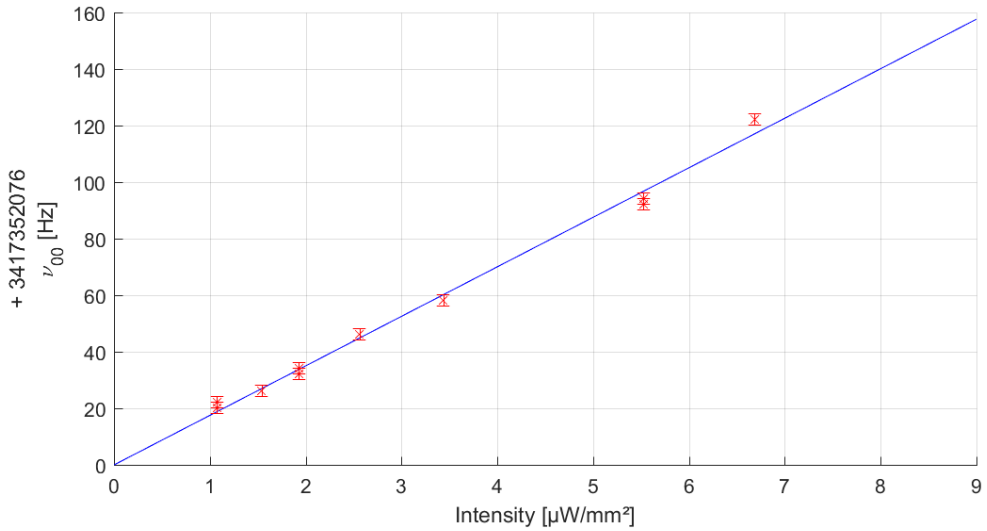

Figure 3.20: ν_{00}-drift of cell 1509-001 - 55.0 Torr:
$\nu_{00}drift(I) = 17.5I$.
Settings in table 3.3 on page 50.

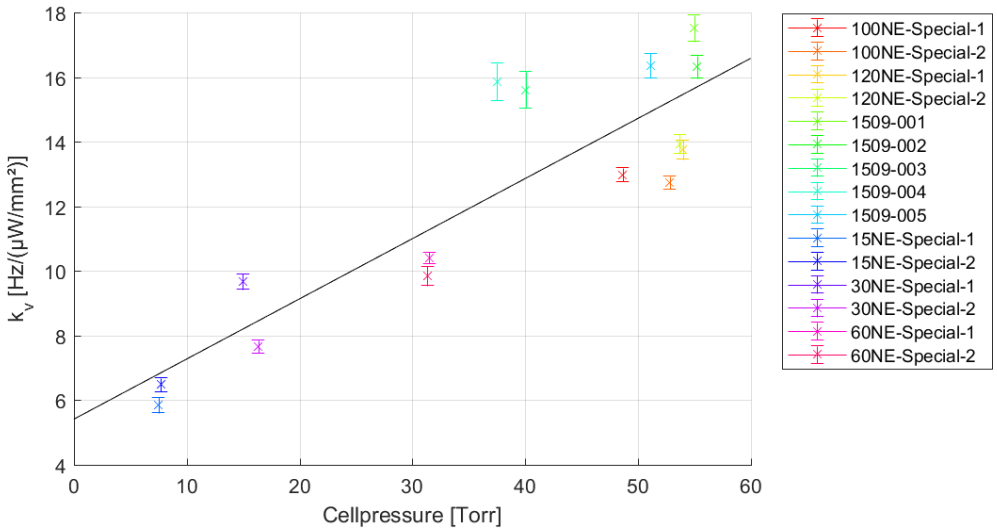

Figure 3.21: Linear Slope of ν_{00}-drift k_v for all available cells.
$k_v(P) = 0.1861P + 5.4178$.
Settings in table 3.3 on page 50.

3.3.1.2 Amplitude and Width

The width of the resonance increases linearly in respect to intensity for all cells. This is expected due to power broadening[53][54]. The slope of the fit decreases fast between 7 to 30 Torr, from 30 Torr onwards there is hardly any change as can be seen in 3.22.

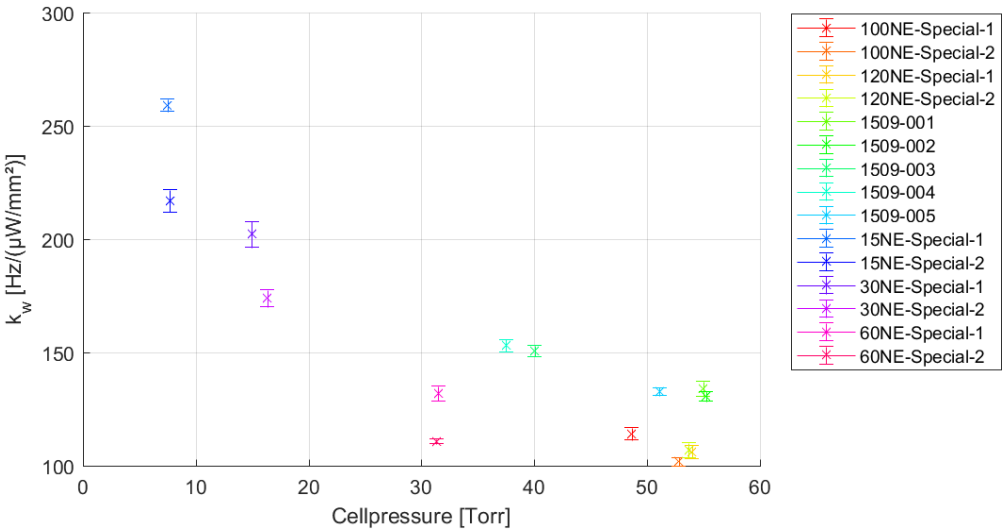

Figure 3.22: Linear Slope of the width k_w for all available cells.
Settings in table 3.3 on page 50.

The CPT-resonance-amplitude decreases slightly or stays the same over the examined region as can be seen in figures 3.17 and 3.18. Thus the ratio is mostly governed by the increase in width: for all cells except for one the best amplitude-width-ratio was found at the lowest intensity or synonymous, largest beam profile. The one outlier has its maximum at the next intensity step. This outlier was caused due to misalignment: part of the laser was cut off as the picture of the laser beam later revealed. As can be seen in in figure 3.23 again better ratios were found for cells with higher-gas-pressure.

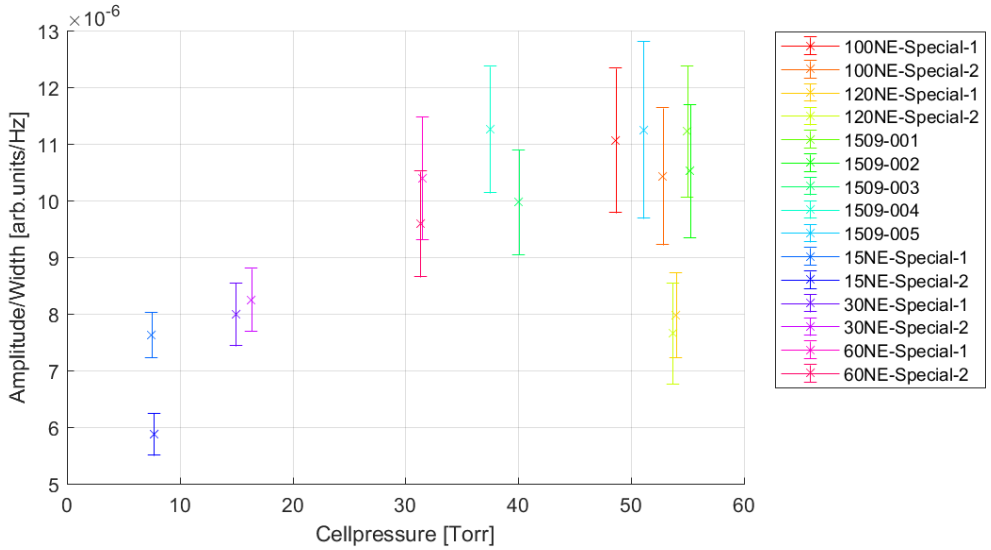

Figure 3.23: Highest achieved amplitude-width-ratio for all cells.
Settings in table 3.3 on page 50.

3.3.1.3 Ground state coherence relaxation

According to [50] the intensity dependence of the resonance width is

$$\delta\nu_{LI} = 2\Gamma_{coh} + \alpha I \tag{3.1}$$

$$\alpha = \frac{\overline{G}}{\Gamma_s} \tag{3.2}$$

where Γ_{coh} is the ground-state coherence relaxation, $\overline{G}$ is dependent on the Rabi-frequency and Γ_s is the decay rate from the excited level.
These have been calculated from the fit parameters for all available cells and are presented in the following plots.

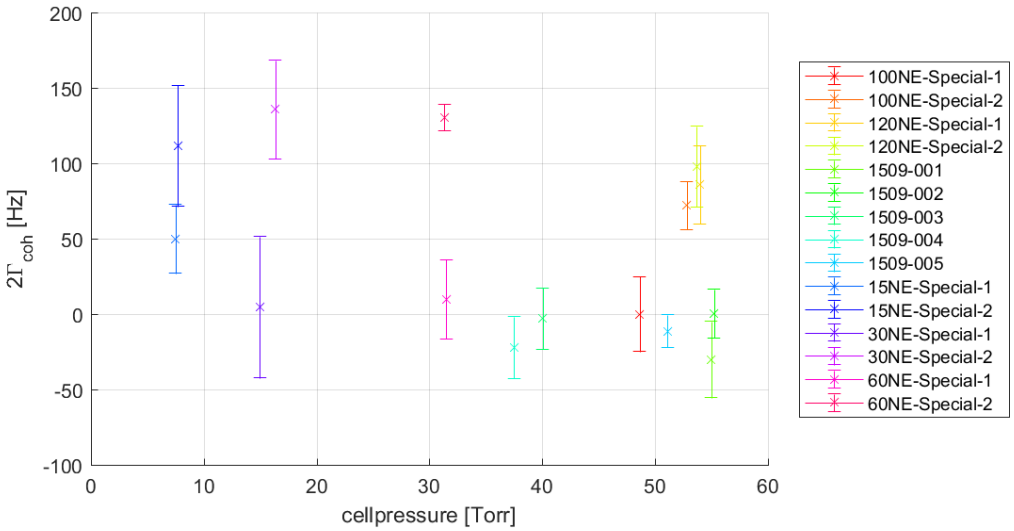

Figure 3.24: $2\Gamma_{coh}$ for all cells.
Settings in table 3.3 on page 50.

Clearly there is a lot variance between the cells of fairly similar neon-pressure and some values do not seem to make a lot of sense, e.g. negative values. This suggests that the measurement is not accurate enough to get a reliable measurement for $2\Gamma_{coh}$. This is probably caused my alignment issues, interference effects between the cell windows and rubidium deposition on the class surface.

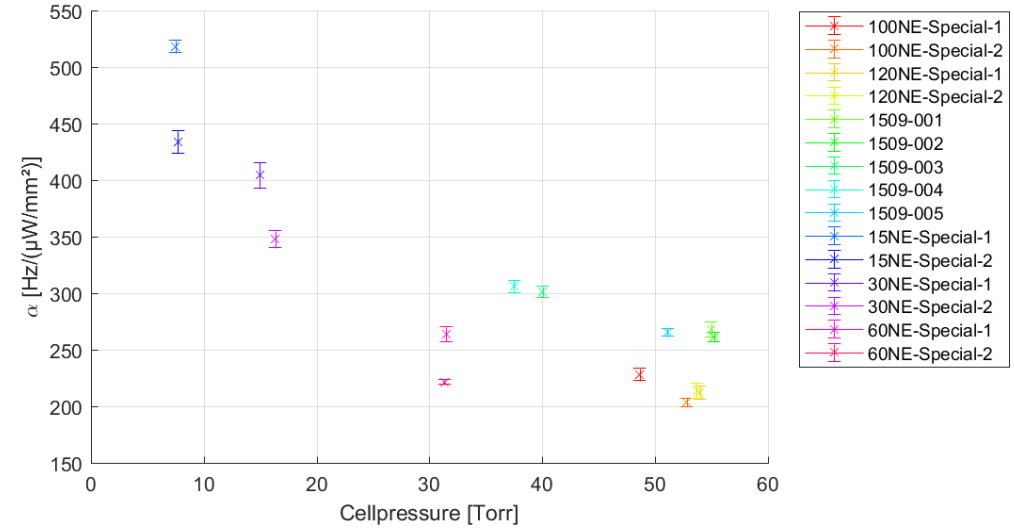

Figure 3.25: α for all available cells.
Settings in table 3.3 on page 50.

As in 3.22 the values drops significantly up to 30 Torr and then stays relatively stable. unfortunately again there is this still a lot of variance.

3.3.2 Laser intensity: Attenuator

The Intensity was decreased by a continuous attenuator, placed between the two mirrors. This was done once with a large beam profile and another time with a small beam profile. Again the cell temperature was kept 35 °C. This was only done for cells 30NE-Special-1 and 100NE-Special-2.

Table 3.4: Settings: Attenuator

Cell temperature		35 °C
Intensity		0.3-4.1 $\frac{\mu W}{mm^2}$
GHz oscillator	Power	0.7 dBm
	Increment	2 Hz
Lock-In amplifier	Modulation Frequency	30120 Hz

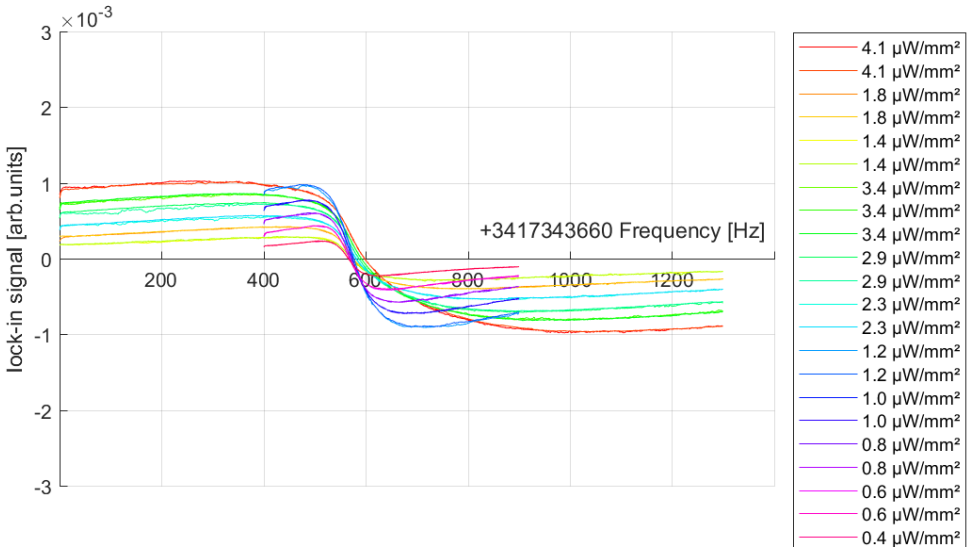

Figure 3.26: Intensity-dependence of 30NE-Special-1 - 14.9 Torr. The scan-width was adjusted to the width of the resonance.
Settings in table 3.4 on page 56.

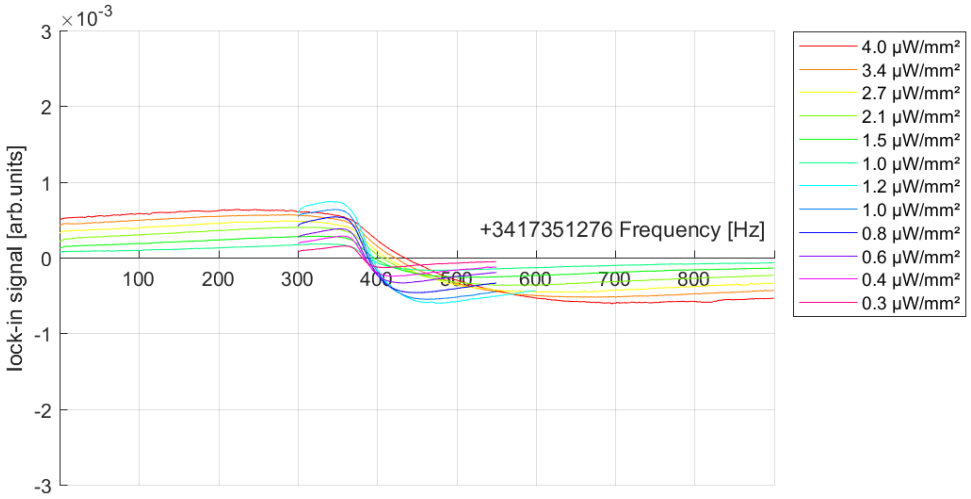

Figure 3.27: Intensity-dependence of 100NE-Special-2 - 52.9 Torr. The scan-width was adjusted to the width of the resonance.
Settings in table 3.4 on page 56.

In both cases the difference between small and large beam profile can clearly be seen:. In the case of the small beam diameter the resonance is far wider.

3.3.2.1 ν_{00}-drift

Both cells showed a similar behaviour as in 3.3.1.1 on page 51.
The slope of the drift for the 30NE-Special-1 was found to be $k_v = 9.7 \pm 0.3 \ \frac{Hz}{(\mu W/mm^2)}$ in the laser width case and $k_v = 8.3 \pm 0.4 \ \frac{Hz}{(\mu W/mm^2)}$ in the other.
For the 100NE-Special-2 cell slopes of $k_v = 12.7 \pm 0.2 \ \frac{Hz}{(\mu W/mm^2)}$) and $k_v = 13.7 \pm 0.4 \ \frac{Hz}{(\mu W/mm^2)}$ were found for laser width and attenuator case, respectively. Thus it can be concluded, that the shift of the resonance is directly dependent on the laser intensity. It is not important whether the intensity is achieved by varying the laser power or by altering the laser width. This is evident from figure 3.28 which lacks the jump, that can be clearly seen in figures 3.30 and 3.27, between small and large beam profile.

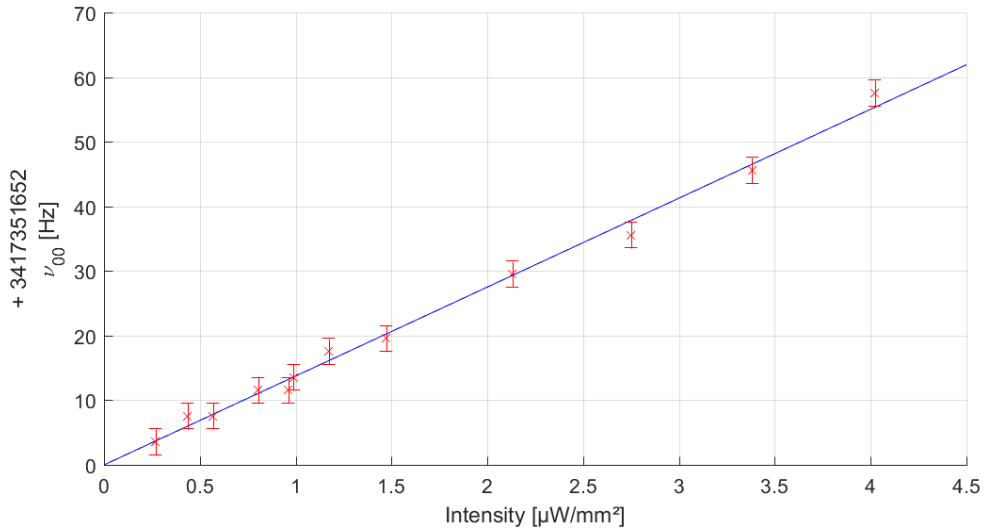

Figure 3.28: ν_{00}-drift of cell 100NE-Special-2 - 52.9 Torr:
$\nu_{00}drift(I) = 13.7I$.
Settings in table 3.4 on page 56.

3.3.2.2 Amplitude and Width

As in 3.3.1.2 the width of the signal increases with intensity. This time on the other hand the amplitude is notably dependent on the total power of the laser. This results in the figures 3.29 and 3.30 in which the ratio is rather constant for the large beam profile because the increase in width and amplitude cancel each other out, while for a small beam profile the ratio improves with intensity. The jump that can be seen in figures 3.29 and 3.30 is caused by the switch between small and large beam profile.
Again a better ratio was achieved with the higher buffer gas cell.

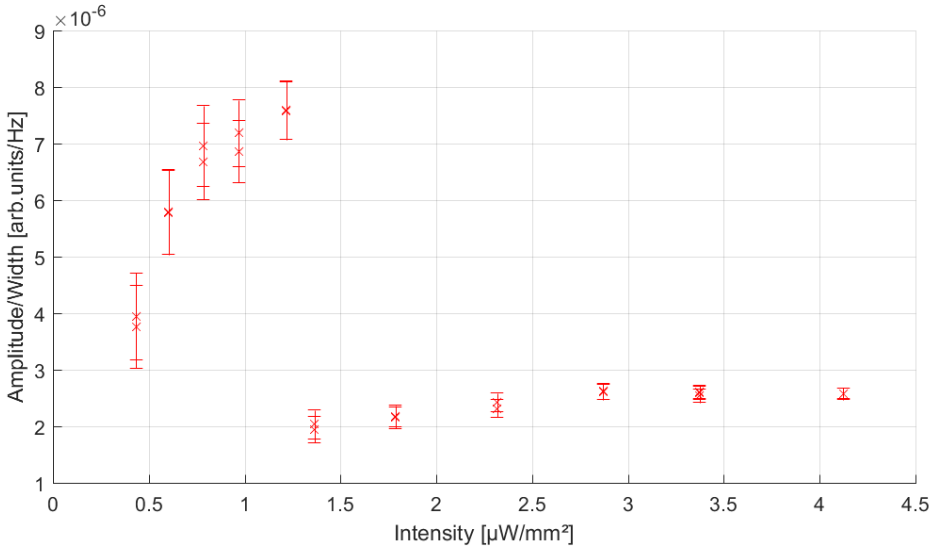

Figure 3.29: Amplitude-width-ratio of 30NE-Special-1 - 14.9 Torr.
Settings in table 3.4 on page 56.

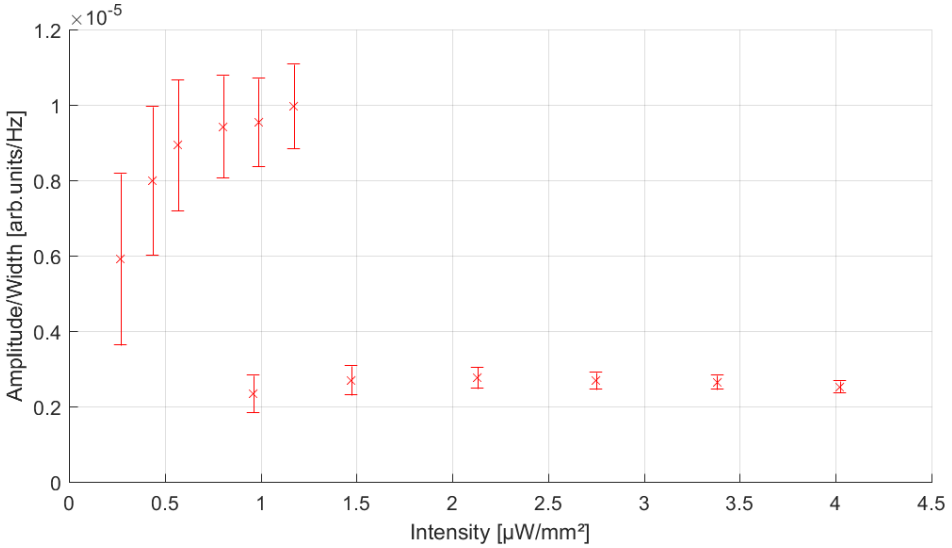

Figure 3.30: Amplitude-width-ratio of 100NE-Special-2 - 52.9 Torr.
Settings in table 3.4 on page 56.

3.3.2.3 Ground state coherence relaxation

As in section 3.3.1.3 $2\Gamma_{coh}$ and α were calculated. For 30NE-Special-1 - 14.9 Torr $2\Gamma_{coh}$ is 80 ± 9 Hz and α is 356 ± 4 $\frac{Hz}{(\mu W/mm^2)}$ compared to $2\Gamma_{coh} = 4 \pm 47$ Hz and $\alpha = 404 \pm 12$ $\frac{Hz}{(\mu W/mm^2)}$ in section 3.3.1.3.

For the second cell 100NE-Special-2 - 52.9 Torr the values are in the attenuator case $2\Gamma_{coh} = 32 \pm 11$ Hz and $\alpha = 235 \pm 6$ $\frac{Hz}{(\mu W/mm^2)}$ while in section in the laser width case they are $2\Gamma_{coh} = 72 \pm 16$ Hz and $\alpha = 204 \pm 4$ $\frac{Hz}{(\mu W/mm^2)}$, respectively.
This again shows that the measurements are not accurate enough for a reliable measurement of $2\Gamma_{coh}$. Unfortunately also the values for α are not within a standard error, but at least they show the same tendency: alpha is much lower for higher pressure cells.

3.4 Two Photon Detuning

The laser carrier frequency was detuned from the value that maximized the CPT-resonance-amplitude in both directions. The temperature was kept at 35 °C and the intensity between 2.0 ± 0.2 $\frac{\mu W}{mm^2}$ and 2.5 ± 0.2 $\frac{\mu W}{mm^2}$ in front of the cell.
The conversion factor from current to frequency was found to be -127 $\frac{GHz}{mA}$ for this specific laser in this regime[16]. This was done for cells 15NE-Special-1, 30NE-Special-2, 100NE-Special-2, 120NE-Special-2 and 1509-002.

Table 3.5: Settings: Two Photon Detuning

Cell temperature		35 °C
Intensity		2-2.5 $\frac{\mu W}{mm^2}$
GHz oscillator	Power	0.7 dBm
	Increment	2 Hz
Lock-In amplifier	Modulation Frequency	30120 Hz

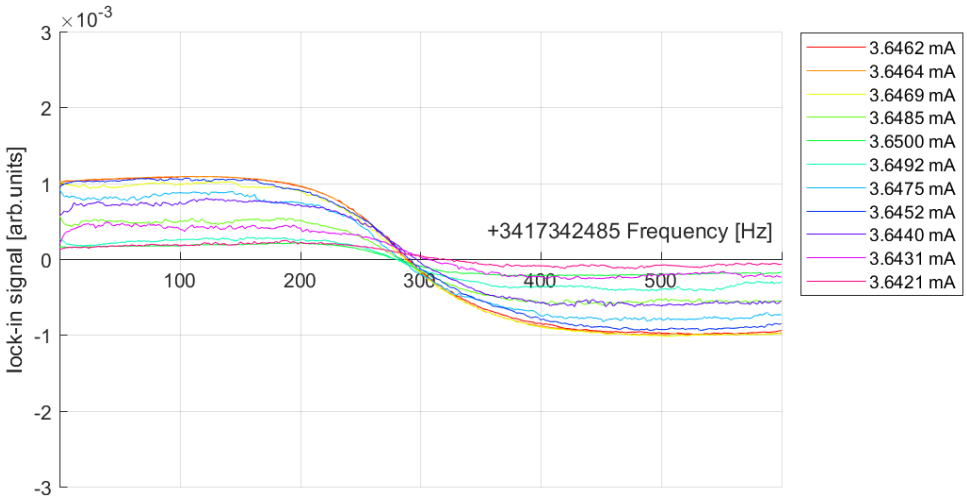

Figure 3.31: Two Photon Detuning of cell 15NE-Special-1 - 7.5 Torr.
As zero detuning point the laser carrier frequency was chosen that should maximize the amplitude.
Settings in table 3.5 on page 61.

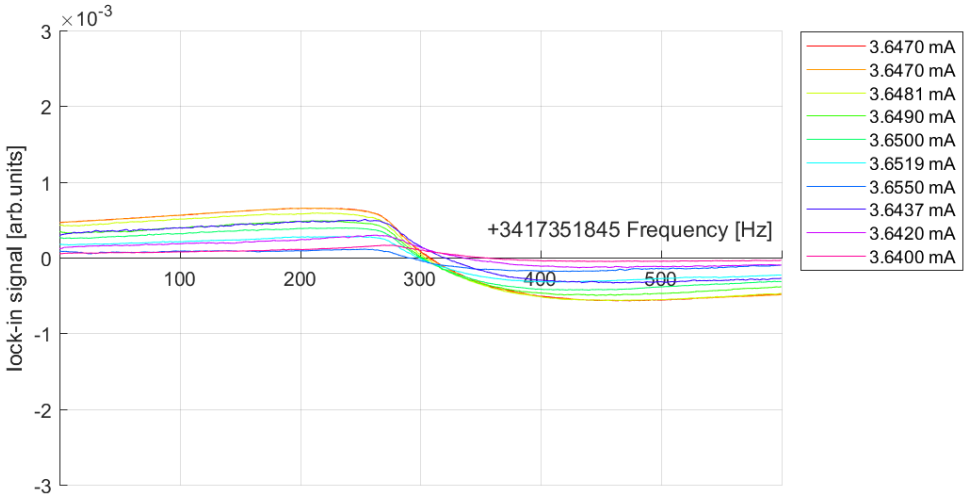

Figure 3.32: Two Photon Detuning of cell 1509-002 - 55.3 Torr.
As zero detuning point the laser carrier frequency was chosen that should maximize the amplitude.
Settings in table 3.5 on page 61.

3.4.1 ν_{00}-drift

The position behaves like a exponential-function as can be seen in figures 3.33 and 3.34. The drift is caused by a combination of ac Stark shifts from the excited state loss channels and an overall change of the lineshape with detuning[43].
The position is relatively stable to a negative detuning, while the zero crossing shifts considerably more for a positive detuning. But in both directions the laser can be detuned several MHz without causing too much of a shift.
Moreover the cells with higher neon pressure could be further detuned and move less than the low buffer gas cell.

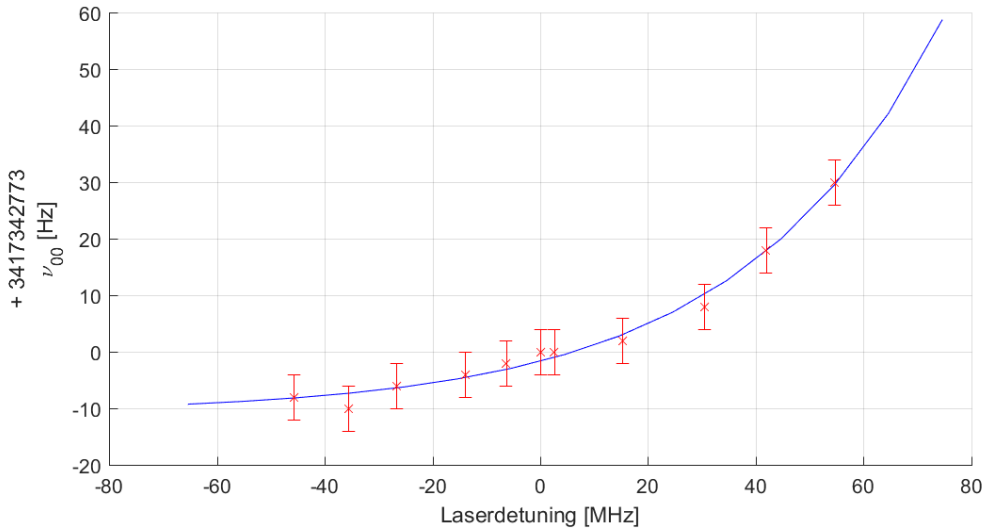

Figure 3.33: ν_{00}-drift of cell 15NE-Special-1 - 7.5 Torr:
$\nu_{00}drift(PD) = 9.1e^{-0.027PD}$.
As zero detuning point the laser carrier frequency was chosen that should maximize the amplitude.
Settings in table 3.5 on page 61.

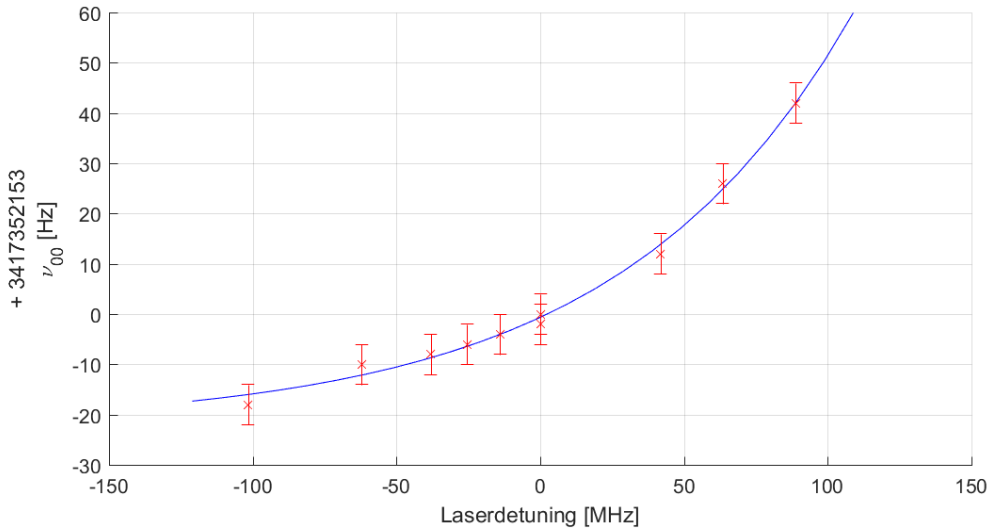

Figure 3.34: ν_{00}-drift of cell 1509-002 - 55.3 Torr:
$\nu_{00}drift(PD) = 21.5e^{-0.012PD}$.
As zero detuning point the laser carrier frequency was chosen that should maximize the amplitude.
Settings in table 3.5 on page 61.

3.4.2 Amplitude and Width

The amplitude-width-ratio remains approximately the same for a detuning of several MHz. Afterwards the amplitude rapidly decreases, while the width stays approximately the same. This threshold value is higher for higher buffer-gas cells.

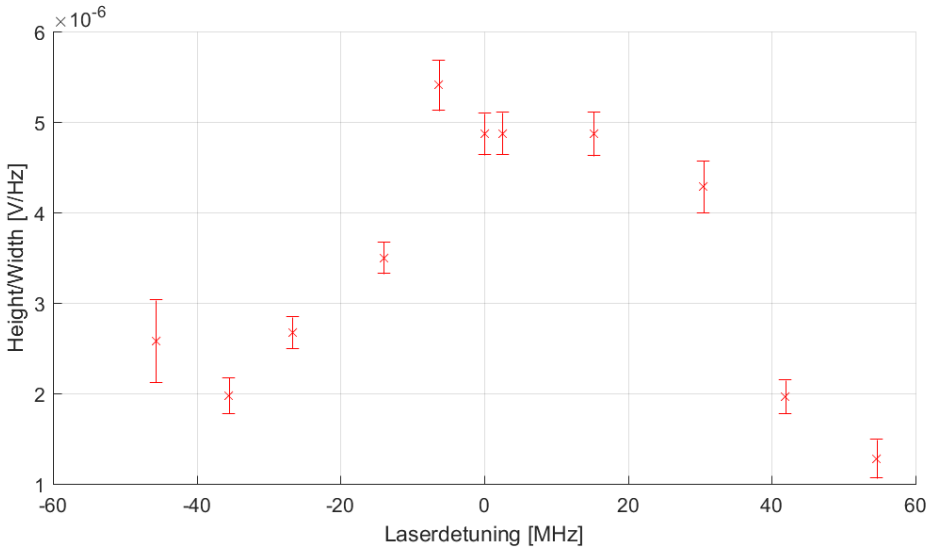

Figure 3.35: Amplitude-width-ratio of cell 15NE-Special-1 - 7.5 Torr.
As zero detuning point the laser carrier frequency was chosen that should maximize the amplitude.
Settings in table 3.5 on page 61.

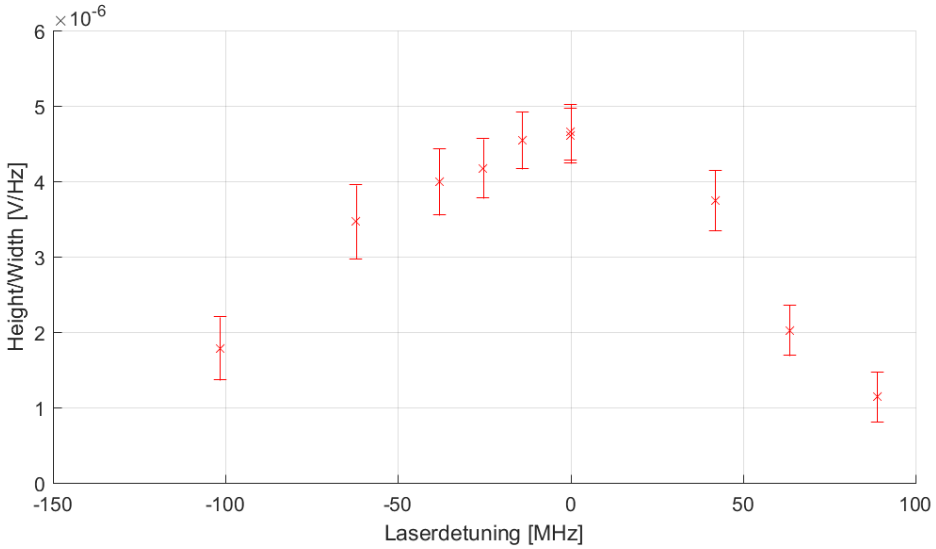

Figure 3.36: Amplitude-width-ratio of cell 1509-002 - 55.3 Torr.
As zero detuning point the laser carrier frequency was chosen that should maximize the amplitude.
Settings in table 3.5 on page 61.

3.5 Microwave Power Variation

The settings of the microwave signal generator were changed between -4.7 and 3.0 dBm microwave power. Higher ones were not tested for fear of destroying the laser.
This alters the ratio between carrier and sidebands strength as discussed in subsection 1.4.3. The temperature was again kept at 35.0 °C and the intensity between 2.0 ± 0.2 $\frac{\mu W}{mm^2}$ and 2.5 ± 0.2 $\frac{\mu W}{mm^2}$ in front of the cell. This was done for cell 60NE-Special-2 and cell 1509-004.

Table 3.6: Settings: Power Variation

Cell temperature		35 °C
Intensity		2-2.5 $\frac{\mu W}{mm^2}$
GHz oscillator	Power	-4.7 - 3 dBm
	Increment	2 Hz
Lock-In amplifier	Modulation Frequency	30120 Hz

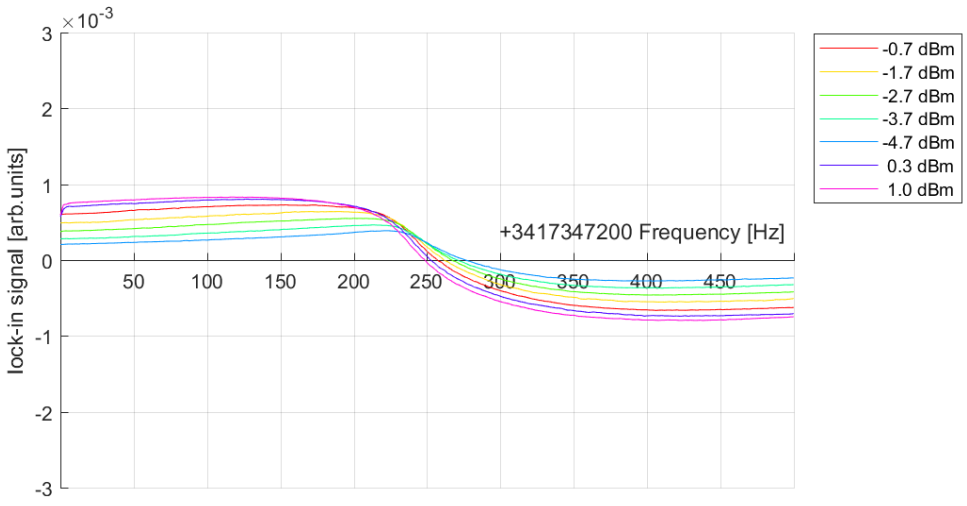

Figure 3.37: Power Variation of cell 60NE-Special-2 - 31.4 Torr.
Settings in table 3.6 on page 66.

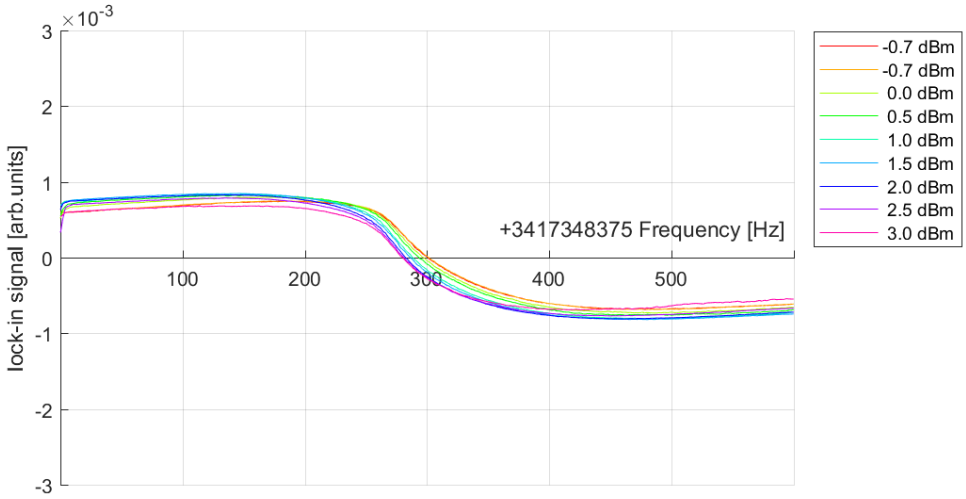

Figure 3.38: Power Variation of cell 1509-004 - 37.6 Torr.
Settings in table 3.6 on page 66.

3.5.1 ν_{00}-drift

The correlation between the position of ν_{00} and dBm is for both tested cells in this region approximately a linear one. This is probably caused by the increase of the total resonant light intensity[50].

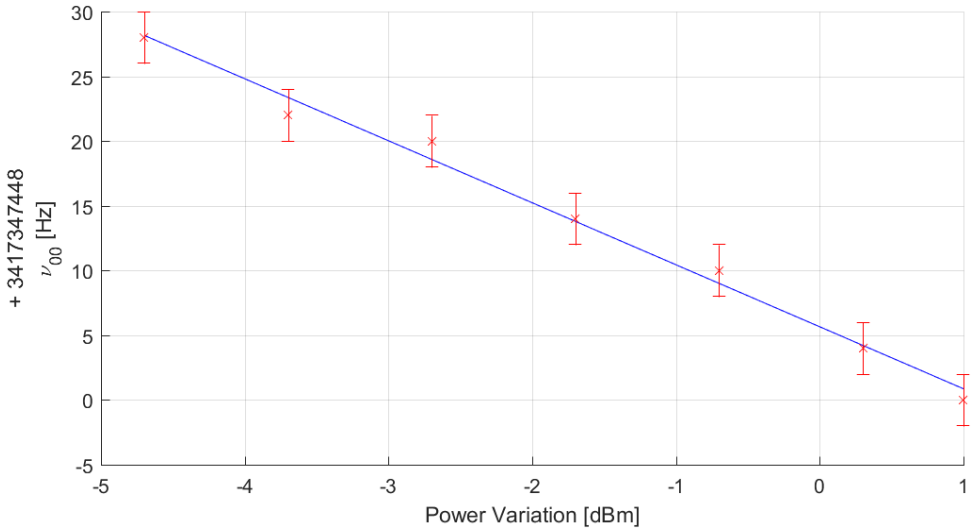

Figure 3.39: ν_{00}-drift of cell 60NE-Special-2 - 31.4 Torr: $\nu_{00} drift(PV) = -4.8PV$.
Settings in table 3.6 on page 66.

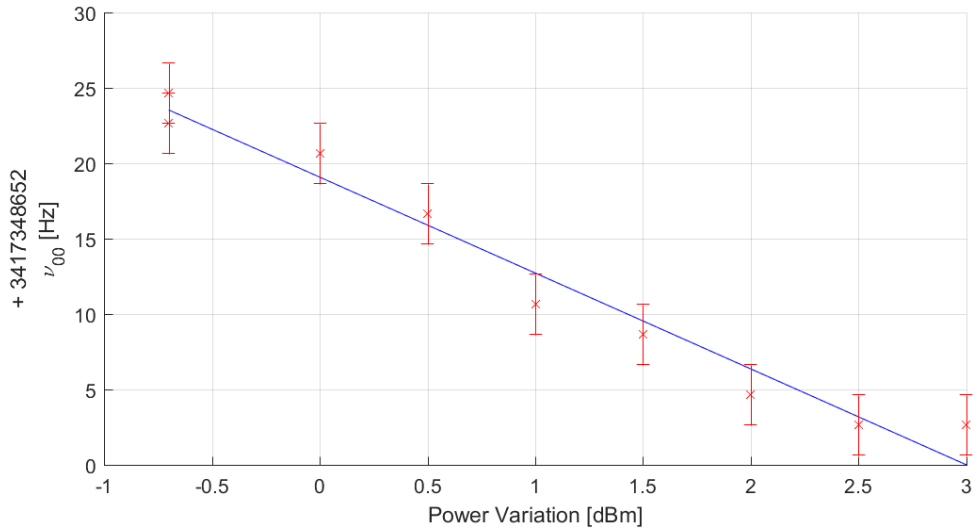

Figure 3.40: ν_{00}-drift of cell 1509-004 - 37.6 Torr: $\nu_{00} drift(PV) = -6.3PV$.
Settings in table 3.6 on page 66.

3.5.2 Amplitude and Width

At first, for the 60NE-Special-2 cell, the ratio slightly increased with power gain in the sidebands, but after -2 dBm the ratio remained almost constant.
The cell 1509-004 kept its' amplitude-width-ratio for the examined region between -0.7 and 3 dBm.

3.5.3 Symmetry

The sideband-strength has a very profound influence on the symmetry of the resonance. In our measurements the best symmetry is achieved with the highest dBm setting as can be in figures 3.41 and 3.42. This is probably because the two sidebands get closer to each other in strength.
The best dBm value should also vary from laser to laser because the modulation capability of every single one is different.

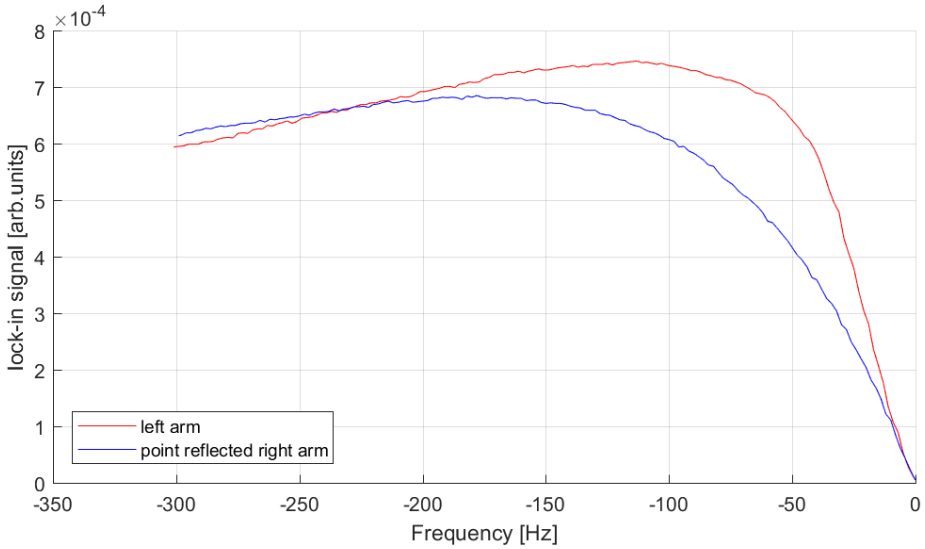

Figure 3.41: Point reflection around ν_{00} for -0.7 dBm microwave signal generator power level for 1509-004 - 37.6 Torr.
Settings in table 3.6 on page 66.

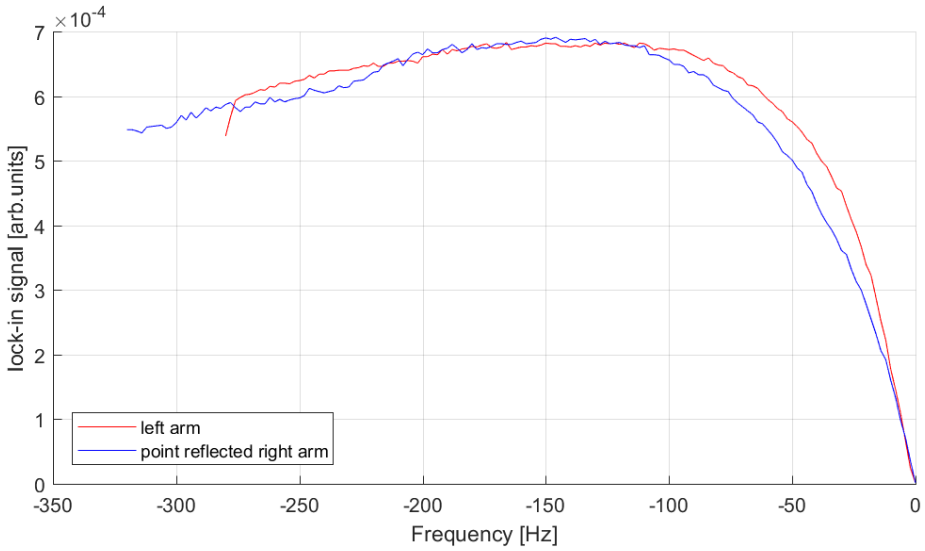

Figure 3.42: Point reflection around ν_{00} for 3.0 dBm microwave signal generator power level for 1509-004 - 37.6 Tor.
Settings in table 3.6 on page 66.

4 Summary

Buffer-gas-Pressure: Section 3.1 starting on page 38

- ν_{00}-drift was used to calculate the buffer-gas-pressure.
- Pressure was a lot lower than assumed.
- Pressure between 7.5 and 55.3 Torr.
- Amplitude-width-ratio stays approximately the same at a temperature of 35℃.

Temperature: Section 3.2 starting on page 41

- ν_{00}-drift best fitted with a quadratic function.
- ca.10 $\frac{Hz}{℃}$ and -0.04 $\frac{Hz}{℃^2}$ at 50 Torr.
- Neon buffer-gas-frequency coefficients change rapidly until ca. 30 Torr and than remains fairly stable.
- Linear temperature coefficient $\frac{\delta}{\nu_0} = 48.5 \pm 7.5 \frac{10^{-12}}{℃Torr}$.
- Quadratic temperature coefficient $\frac{\gamma}{\nu_0} = -0.2 \pm 0.1 \frac{10^{-12}}{℃^2 Torr}$.
- Amplitude-width-ratio improves until ca. 50-60 ℃.
- Improvements are greater for higher buffer-gas-cells.

Laser intensity: Section 3.3 starting on page 50

- ν_{00}-drift is linear.
- Slope increases with higher buffer-gas-pressure.
- Amplitude depends on laser-power.
- Width depends linearly on laser-intensity.
- Best amplitude-width-ratio with a broad laser-profile.
- Better ratio with higher buffer-gas-pressure.

Two Photon Detuning: Section 3.4 starting on page 61

- ν_{00} fairly stable to detuning.
- Higher buffer-gas-pressure leads to more stability.
- Amplitude-width-ratio decreases with detuning.

Microwave Power Variation: Section 3.5 starting on page 66

- ν_{00} decreases linearly with higher dBm.

- Amplitude-width-ratio improves to a certain threshold value.
- Higher dBm lead to higher symmetry of the resonance

5 Conclusion

Based on the results of chapter 3 "Parameter Studies" certain conclusions can be made for an optimal operation of the CDSM.
Firstly, neon-pressure should be high. Cells with high buffer-gas-pressure constantly performed better and there should be even further improvement with increased pressure.
The temperature for the best possible amplitude-width-ratio is dependent on the cell, but is around 40-60 °C. If the width of the resonance is of utmost concern lower temperatures are desirable.
Furthermore the width of the laser should be maximized, as the best results have always been found with the largest beam profile. In the case of a large profile the amplitude-width-ratio can be optimized by increasing the laser power, but this comes again at the cost of a wider resonance.
Lastly the microwave power should be chosen such that the resonance is as symmetric as possible, but this is highly dependent on the given VCSEL.

6 Appendix

6.1 15NE-Special-1

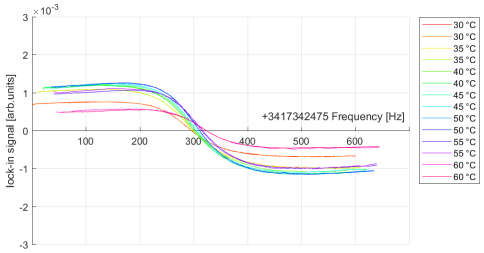

(a) All measurements

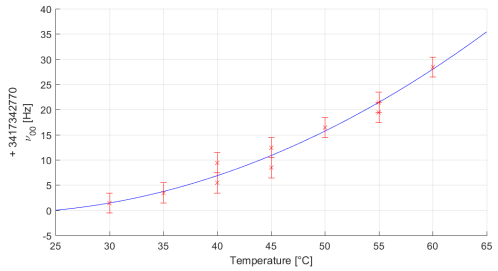

(b) ν_{00}-drift: $\nu_{00}drift(T) = -0.7T + 0.02T^2$

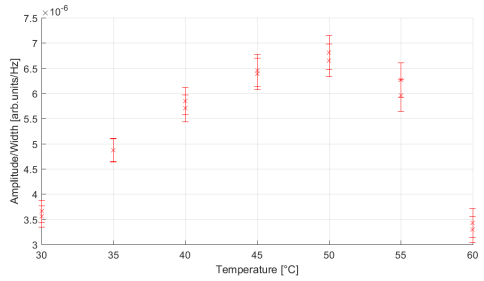

(c) Amplitude-width-ratio

Figure 6.1: Temperature dependence

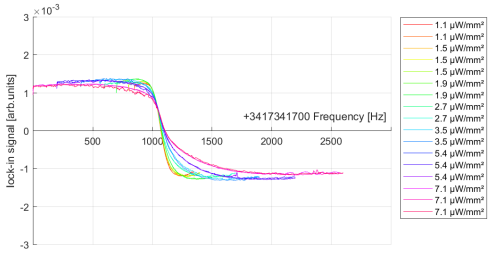

(a) All measurements

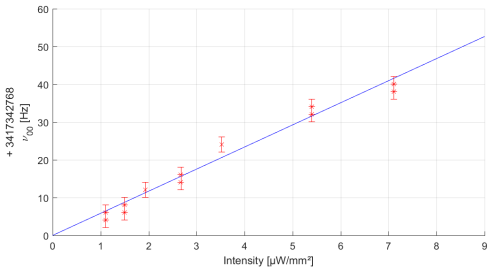

(b) ν_{00}-drift: $\nu_{00}drift(I) = 5.9I$

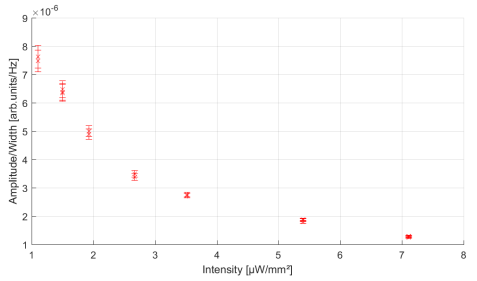

(c) Amplitude-width ratio

Figure 6.2: Laser width dependence

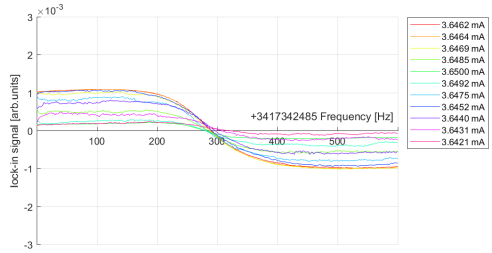

(a) All measurements

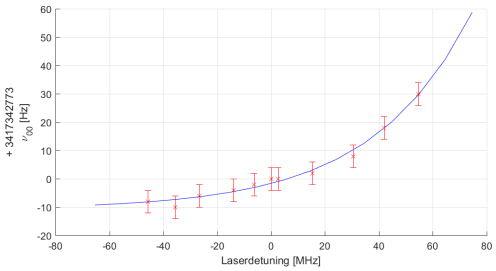

(b) ν_{00}-drift: $\nu_{00} drift(PD) = 9.1e^{-0.027PD}$

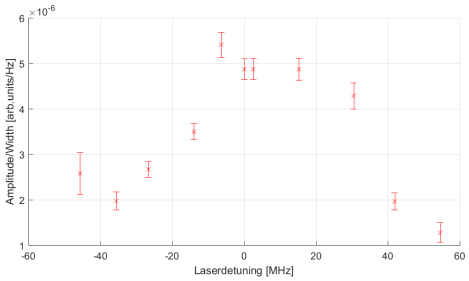

(c) Amplitude-width ratio

Figure 6.3: Two Photon Detuning

6.2 15NE-Special-2

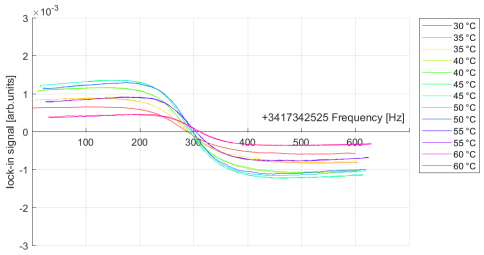

(a) All measurements

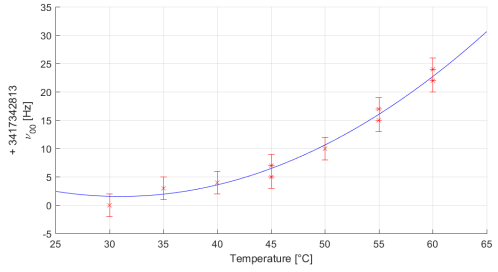

(b) ν_{00}-drift: $\nu_{00}drift(T) = -1.6T + 0.03T^2$

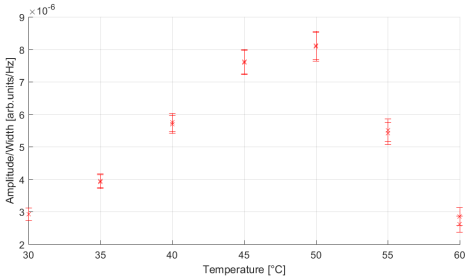

(c) Amplitude-width ratio

Figure 6.4: Temperature dependence

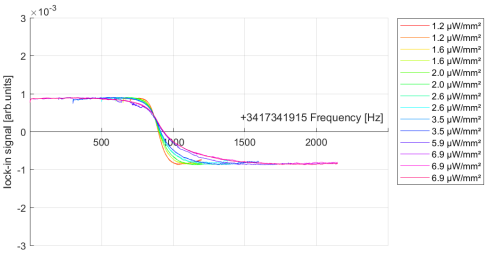

(a) All measurements

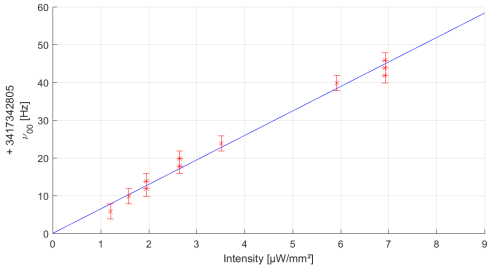

(b) ν_{00}-drift: $\nu_{00}drift(I) = 6.5I$

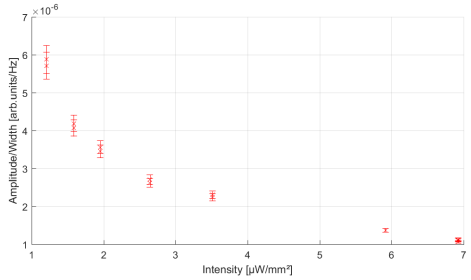

(c) Amplitude-width ratio

Figure 6.5: Laser width dependence

6.3 30NE-Special-1

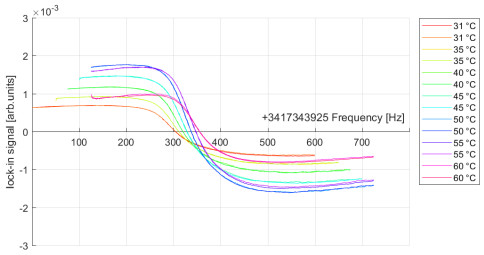

(a) All measurements

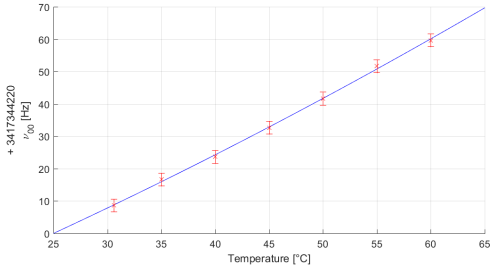

(b) ν_{00}-drift: $\nu_{00}drift(T) = 1.3T + 0.01T^2$

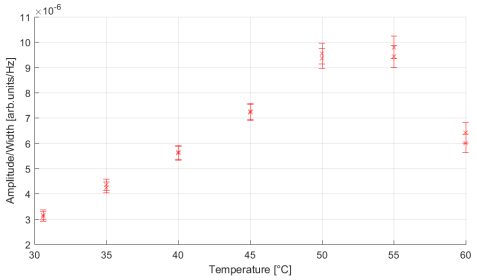

(c) Amplitude-width ratio

Figure 6.6: Temperature dependence

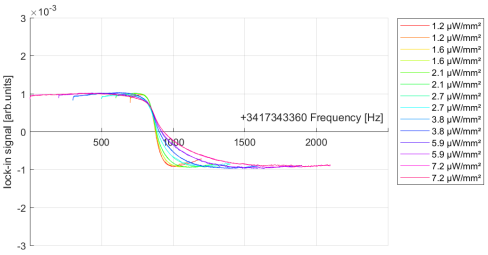

(a) All measurements

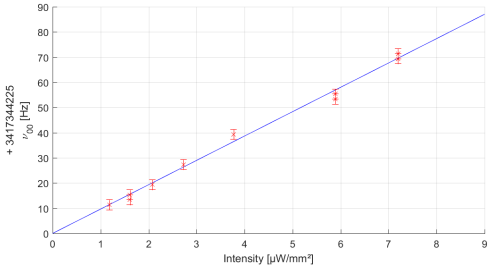

(b) ν_{00}-drift: $\nu_{00}drift(I) = 9.7I$

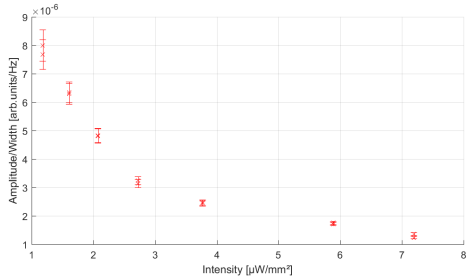

(c) Amplitude-width ratio

Figure 6.7: Laser width dependence

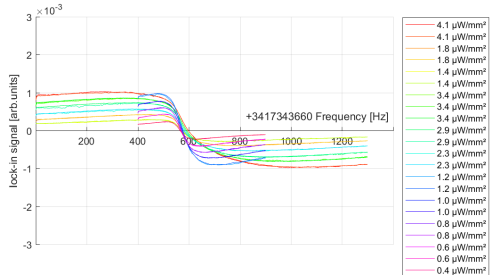

(a) All measurements

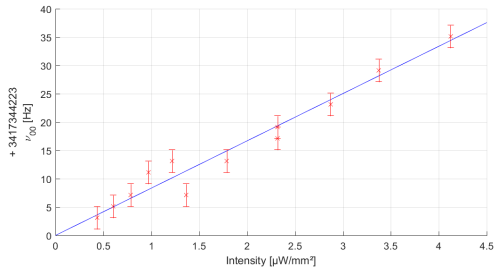

(b) ν_{00}-drift: $\nu_{00} drift(I) = 8.3I$

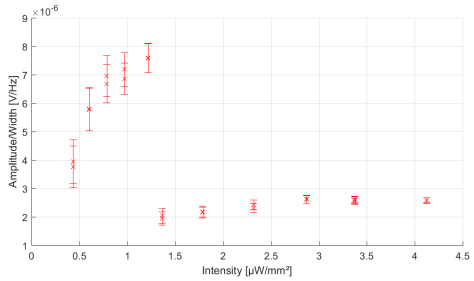

(c) Amplitude-width ratio

Figure 6.8: Attenuator dependence

6.4 30NE-Special-2

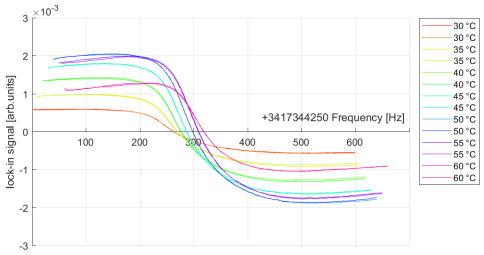

(a) All measurements

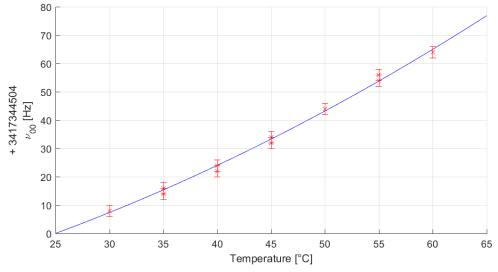

(b) ν_{00}-drift: $\nu_{00}drift(T) = 0.8T + 0.01T^2$

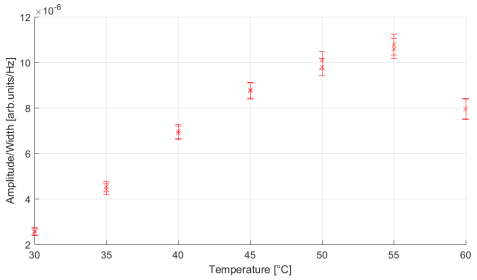

(c) Amplitude-width ratio

Figure 6.9: Temperature dependence

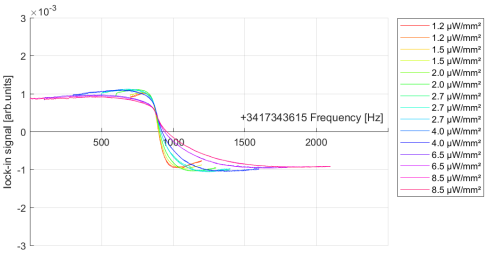

(a) All measurements

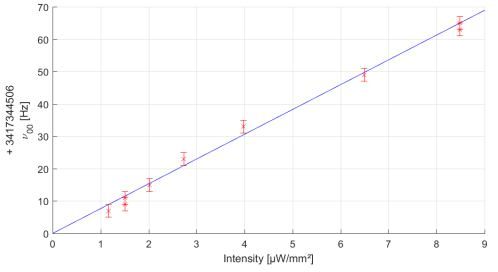

(b) ν_{00}-drift: $\nu_{00}drift(I) = 7.7I$

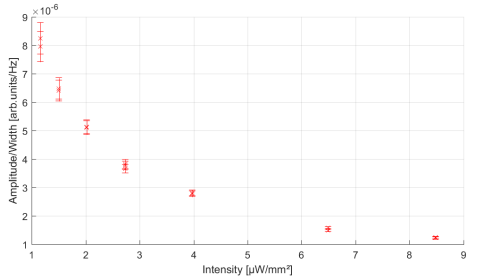

(c) Amplitude-width ratio

Figure 6.10: Laser width dependence

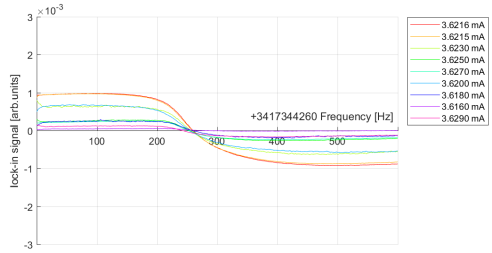

(a) All measurements

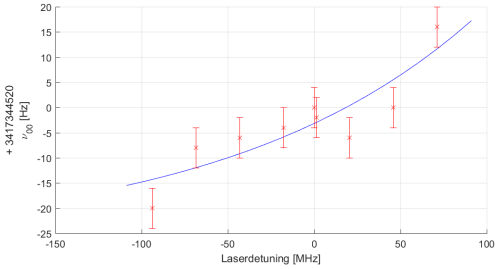

(b) ν_{00}-drift: $\nu_{00}drift(PD) = 23.4e^{-0.069PD}$

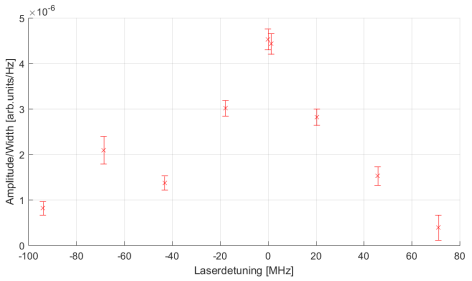

(c) Amplitude-width ratio

Figure 6.11: Two Photon Detuning

6.5 60NE-Special-1

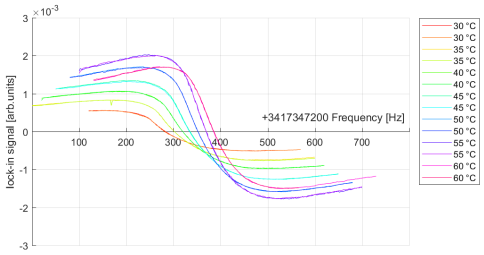

(a) All measurements

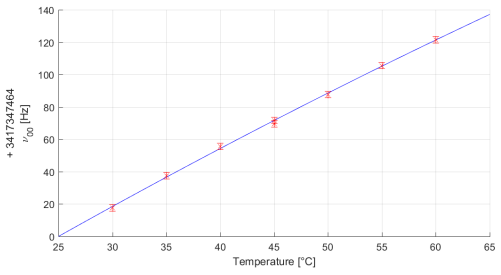

(b) ν_{00}-drift: $\nu_{00}drift(T) = 4.1T - 0.01T^2$

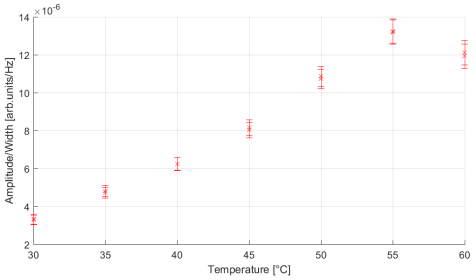

(c) Amplitude-width ratio

Figure 6.12: Temperature dependence

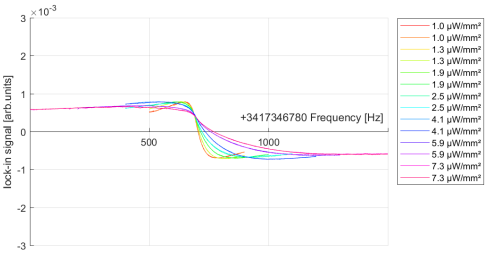

(a) All measurements

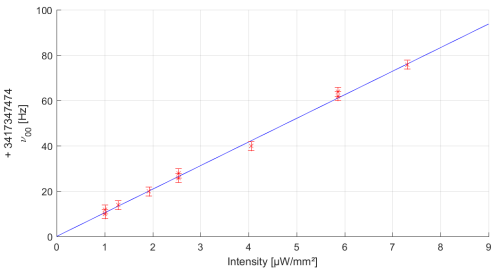

(b) ν_{00}-drift: $\nu_{00}drift(I) = 10.4I$

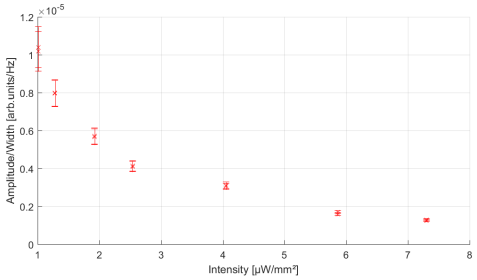

(c) Amplitude-width ratio

Figure 6.13: Laser width dependence

6.6 60NE-Special-2

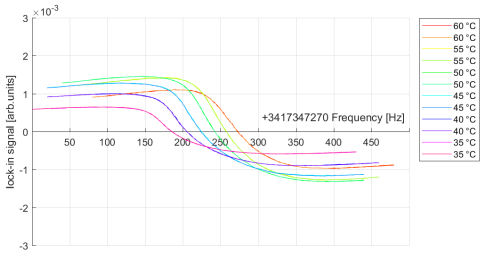

(a) All measurements

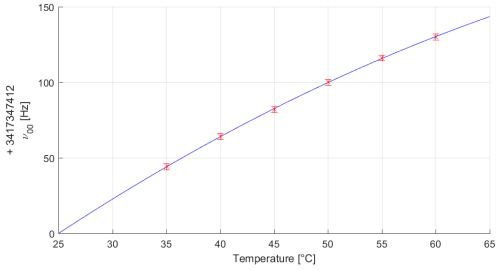

(b) ν_{00}-drift: $\nu_{00} drift(T) = 6.0T - 0.03T^2$

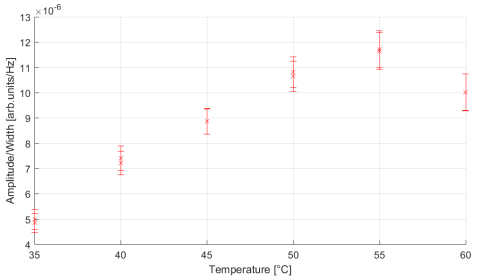

(c) Amplitude-width ratio

Figure 6.14: Temperature dependence

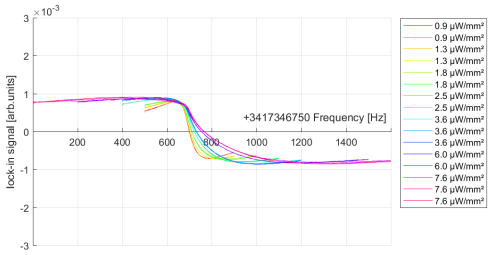

(a) All measurements

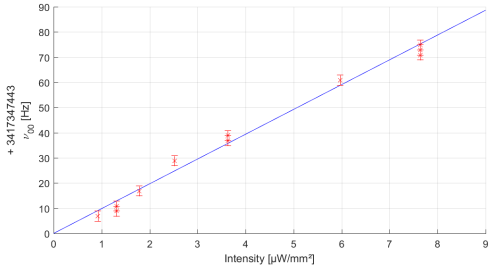

(b) ν_{00}-drift: $\nu_{00} drift(I) = 9.8I$

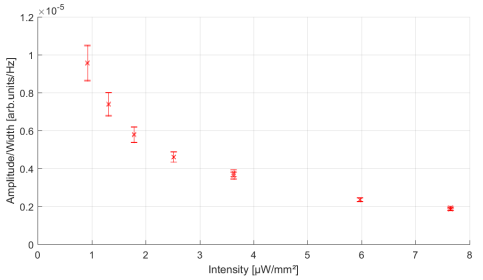

(c) Amplitude-width ratio

Figure 6.15: Laser width dependence

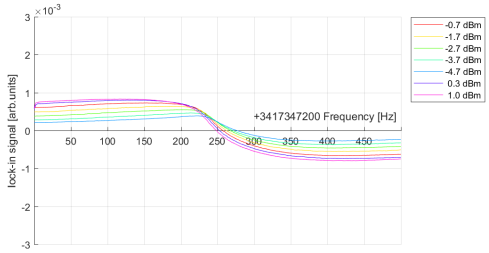

(a) All measurements

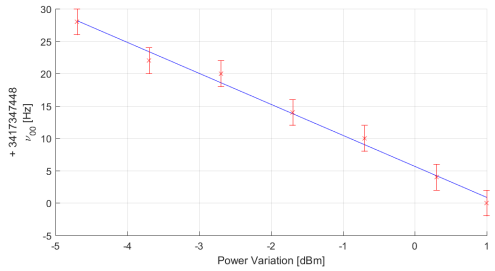

(b) ν_{00}-drift: $\nu_{00} drift(PV) = -4.8PV$

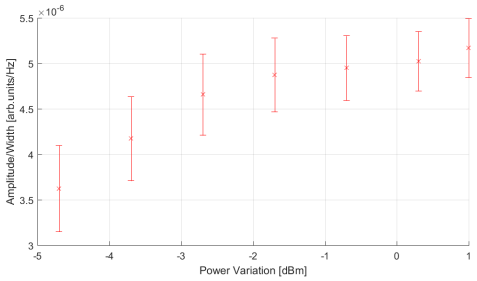

(c) Amplitude-width ratio

Figure 6.16: Power variation

6.7 100NE-Special-1

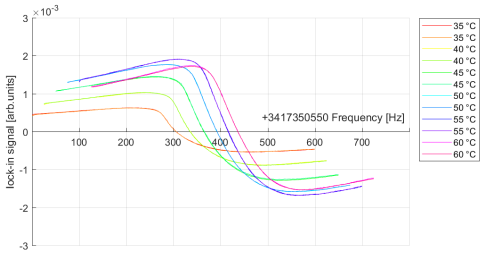

(a) All measurements

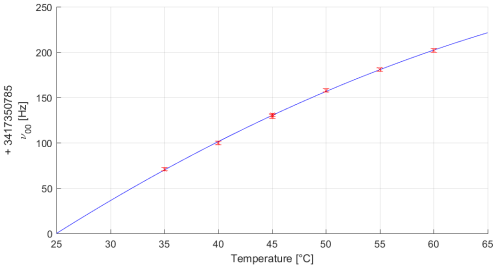

(b) ν_{00}-drift: $\nu_{00}drift(T) = 9.9T - 0.05T^2$

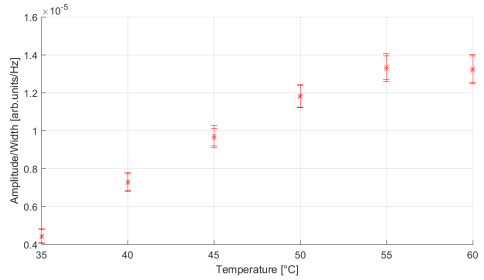

(c) Amplitude-width ratio

Figure 6.17: Temperature dependence

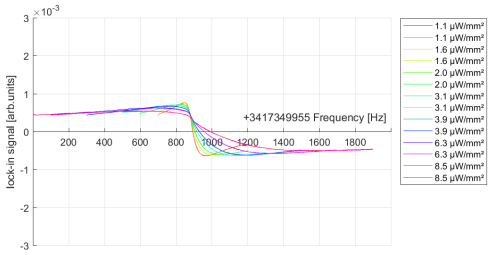

(a) All measurements

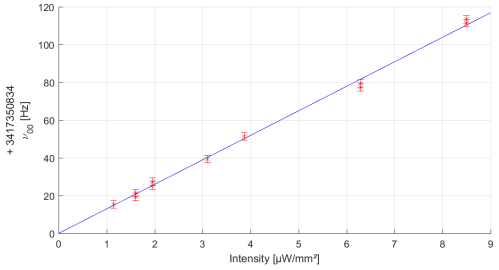

(b) ν_{00}-drift: $\nu_{00}drift(I) = 13.0I$

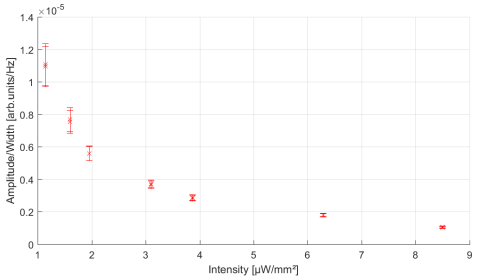

(c) Amplitude-width ratio

Figure 6.18: Laser width dependence

6.8 100NE-Special-2

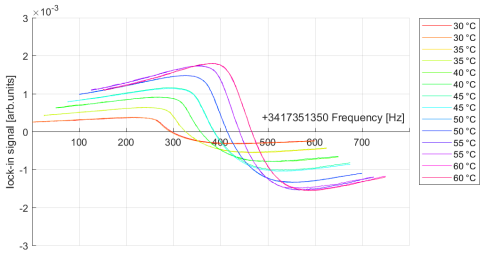

(a) All measurements

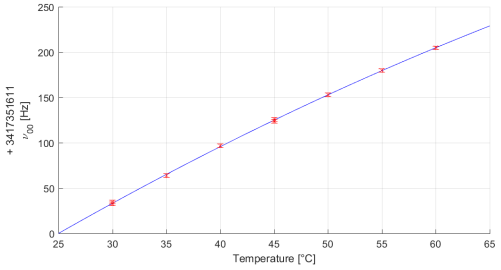

(b) ν_{00}-drift: $\nu_{00}drift(T) = 8.1T - 0.03T^2$

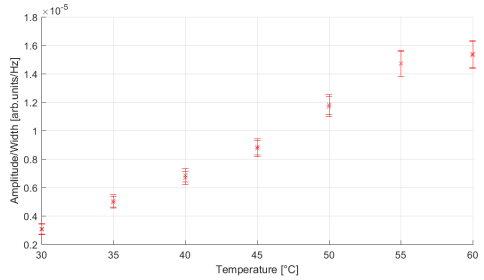

(c) Amplitude-width ratio

Figure 6.19: Temperature dependence

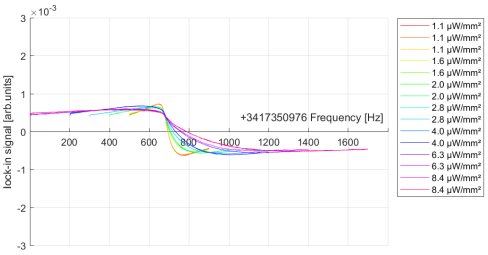

(a) All measurements

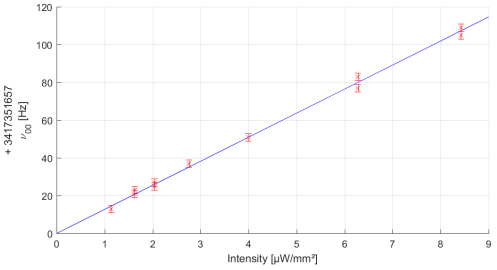

(b) ν_{00}-drift: $\nu_{00}drift(I) = 12.7I$

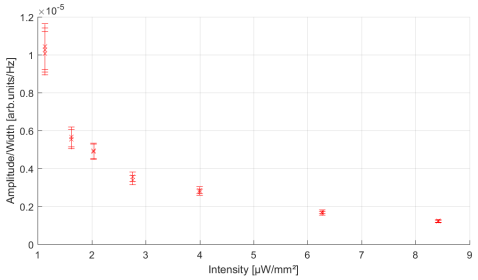

(c) Amplitude-width ratio

Figure 6.20: Laser width dependence

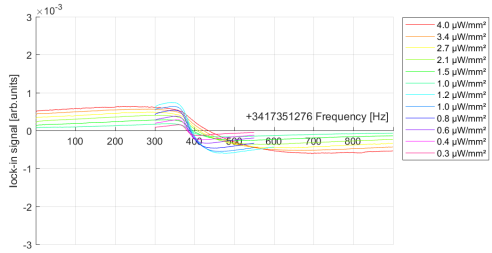

(a) All measurements

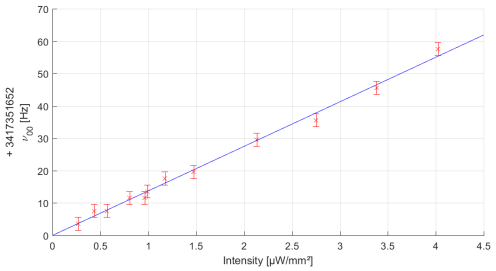

(b) ν_{00}-drift: $\nu_{00}drift(I) = 13.7I$

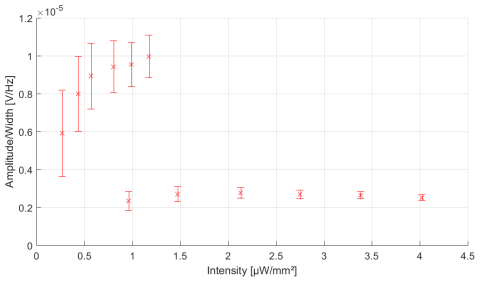

(c) Amplitude-width ratio

Figure 6.21: Attenuator dependence

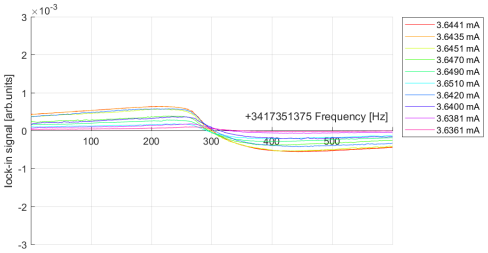

(a) All measurements

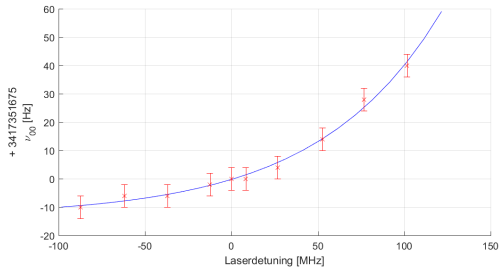

(b) ν_{00}-drift: $\nu_{00}drift(PD) = 13.0e^{-0.014PD}$

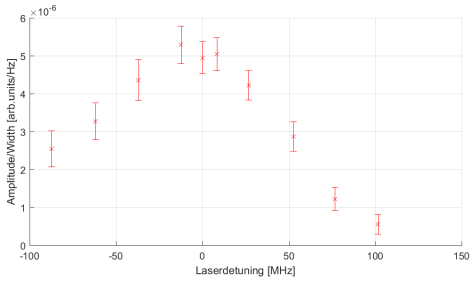

(c) Amplitude-width ratio

Figure 6.22: Two Photon Detuning

6.9 120NE-Special-1

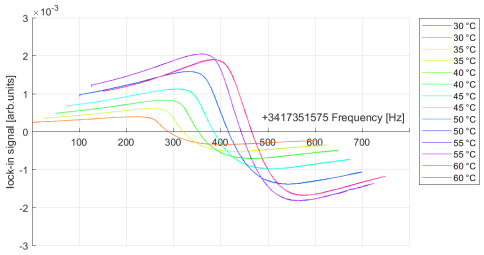

(a) All measurements

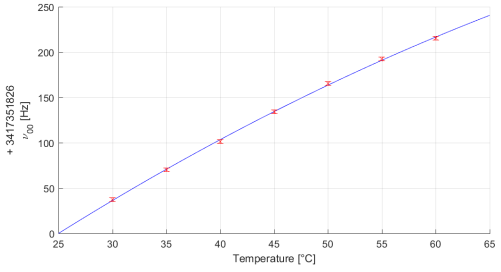

(b) ν_{00}-drift: $\nu_{00}drift(T) = 9.2T - 0.04T^2$

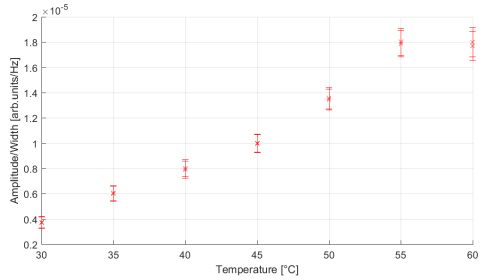

(c) Amplitude-width ratio

Figure 6.23: Temperature dependence

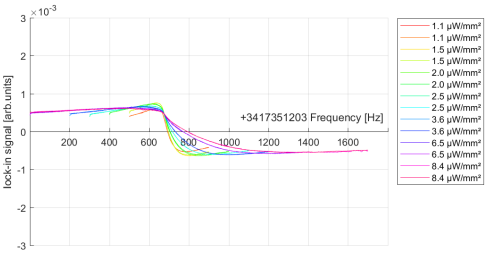

(a) All measurements

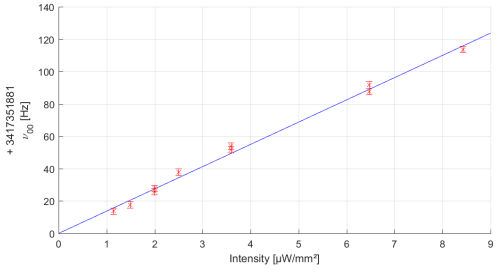

(b) ν_{00}-drift: $\nu_{00}drift(I) = 13.7I$

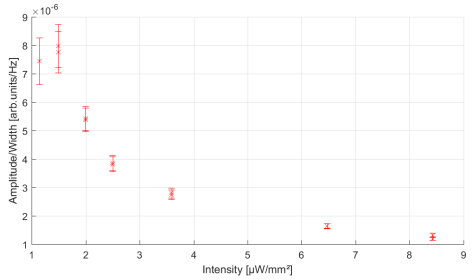

(c) Amplitude-width ratio

Figure 6.24: Laser width dependence

6.10 120NE-Special-2

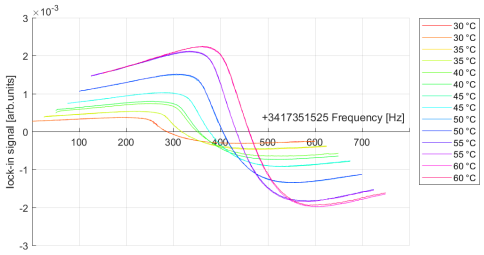

(a) All measurements

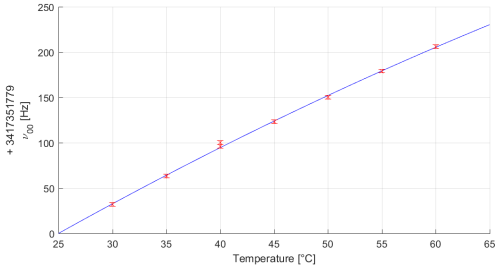

(b) ν_{00}-drift: $\nu_{00}drift(T) = 7.7T - 0.02T^2$

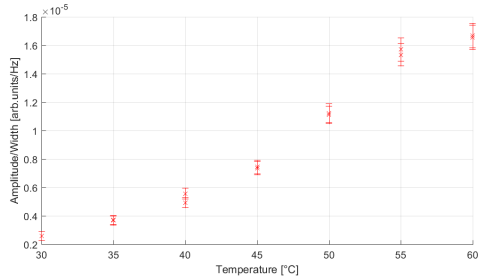

(c) Amplitude-width ratio

Figure 6.25: Temperature dependence

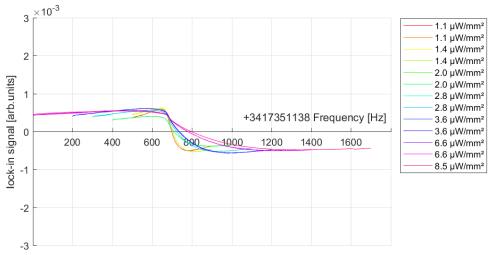

(a) All measurements

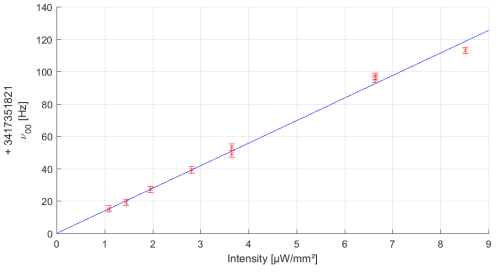

(b) ν_{00}-drift: $\nu_{00}drift(I) = 13.9I$

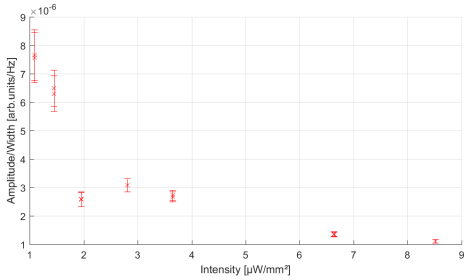

(c) Amplitude-width ratio

Figure 6.26: Laser width dependence

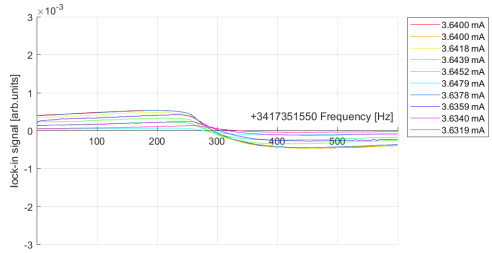

(a) All measurements

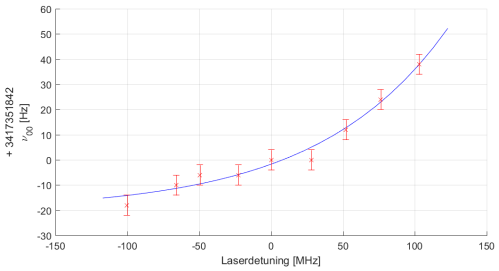

(b) ν_{00}-drift: $\nu_{00}drift(PD) = 18.5e^{-0.011PD}$

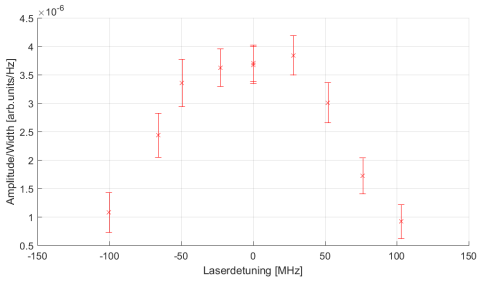

(c) Amplitude-width ratio

Figure 6.27: Two Photon Detuning

6.11 1509-001

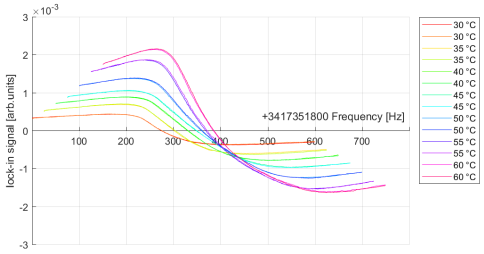

(a) All measurements

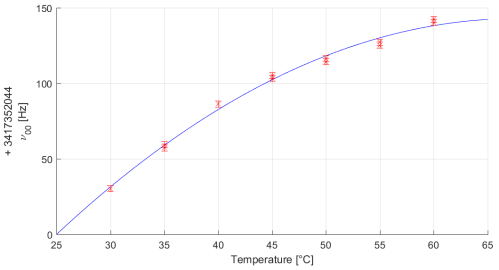

(b) ν_{00}-drift: $\nu_{00}drift(T) = 10.6T - 0.08T^2$

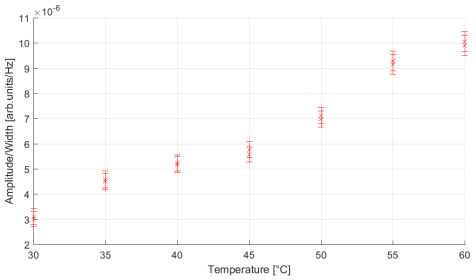

(c) Amplitude-width ratio

Figure 6.28: Temperature dependence

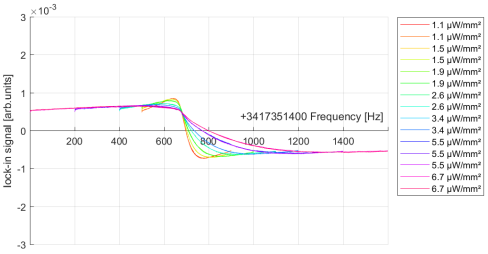

(a) All measurements

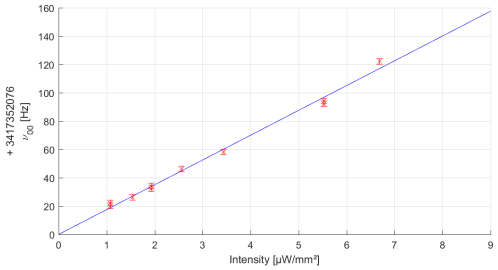

(b) ν_{00}-drift: $\nu_{00}drift(I) = 17.5I$

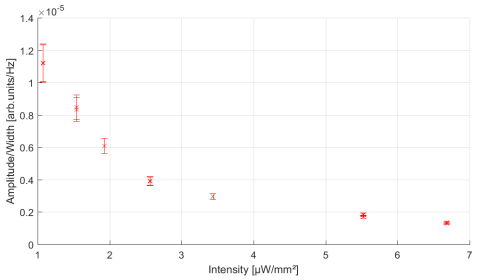

(c) Amplitude-width ratio

Figure 6.29: Laser width dependence

6.12 1509-002

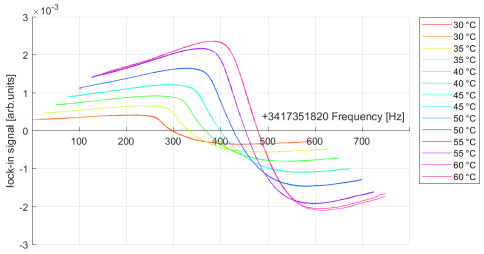

(a) All measurements

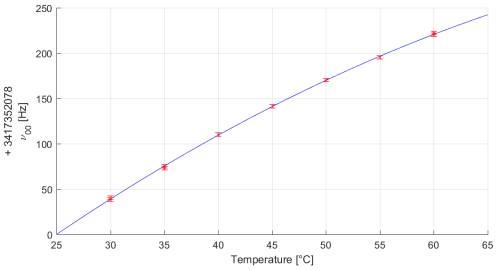

(b) ν_{00}-drift: $\nu_{00}drift(T) = 10.5T - 0.05T^2$

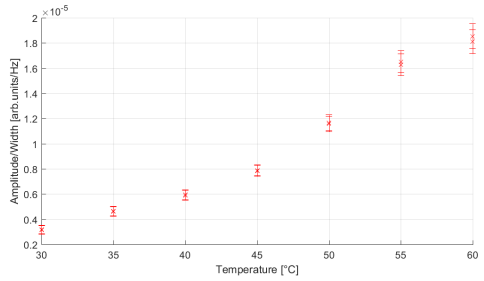

(c) Amplitude-width ratio

Figure 6.30: Temperature dependence

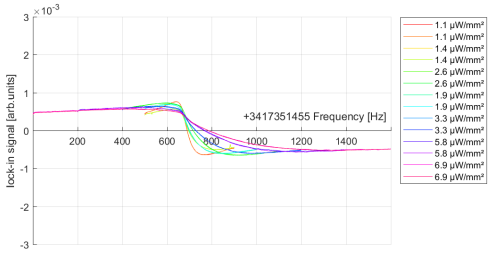

(a) All measurements

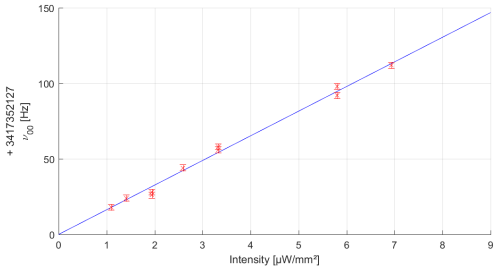

(b) ν_{00}-drift: $\nu_{00}drift(I) = 16.3I$

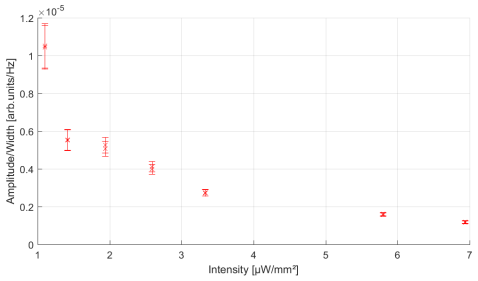

(c) Amplitude-width ratio

Figure 6.31: Laser width dependence

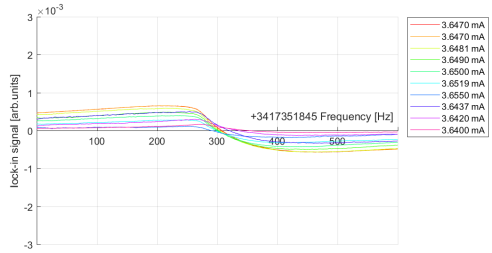

(a) All measurements

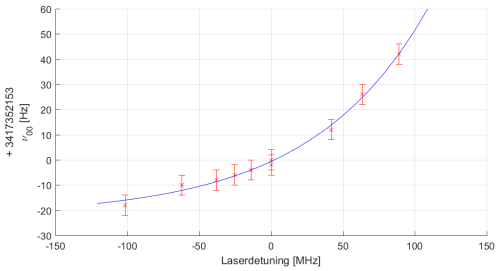

(b) ν_{00}-drift: $\nu_{00}drift(PD) = 21.5e^{-0.012PD}$

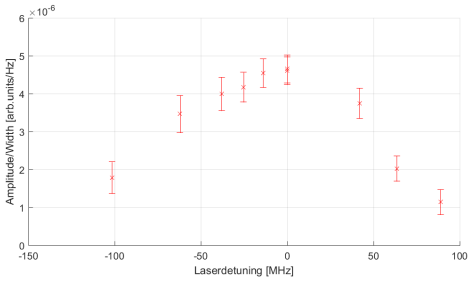

(c) ν_{00}-drift

Figure 6.32: Two Photon Detuning

6.13 1509-003

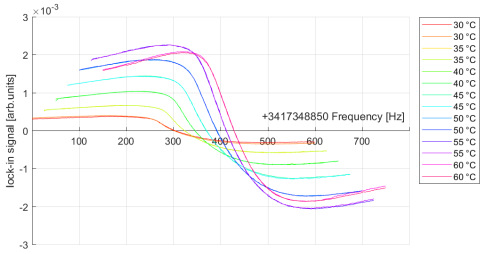

(a) All measurements

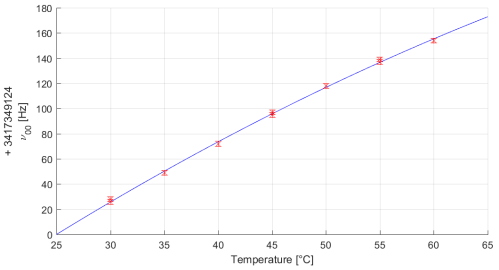

(b) ν_{00}-drift: $\nu_{00}drift(T) = 6.4T - 0.02T^2$

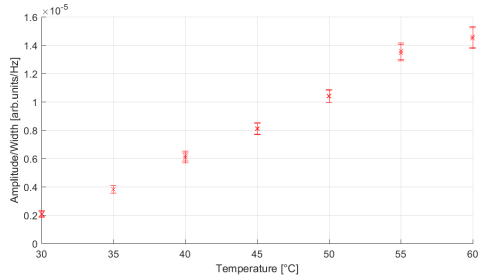

(c) Amplitude-width ratio

Figure 6.33: Temperature dependence

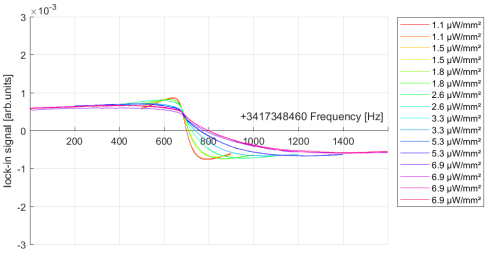

(a) All measurements

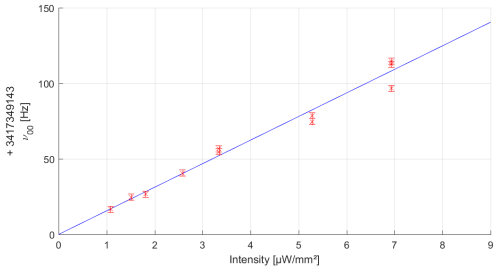

(b) ν_{00}-drift: $\nu_{00}drift(I) = 15.6I$

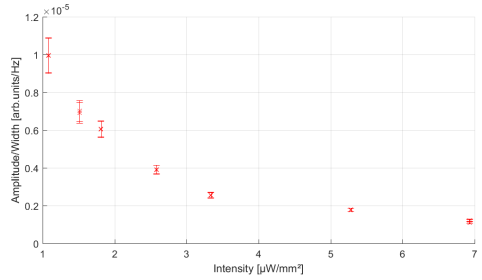

(c) Amplitude-width ratio

Figure 6.34: Laser width dependence

6.14 1509-004

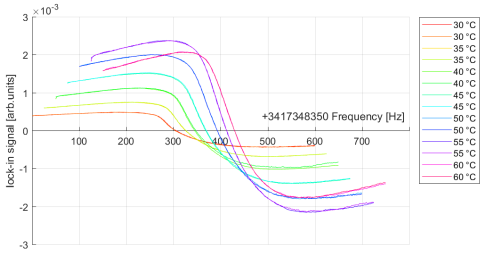

(a) All measurements

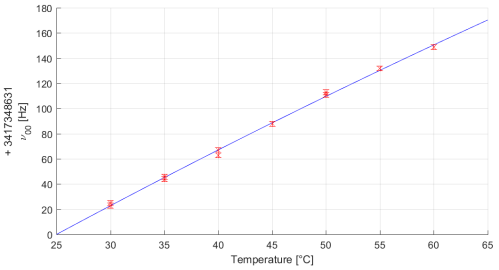

(b) ν_{00}-drift: $\nu_{00}drift(T) = 5.0T - 0.01T^2$

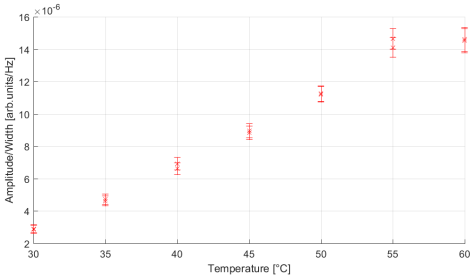

(c) Amplitude-width ratio

Figure 6.35: Temperature dependence

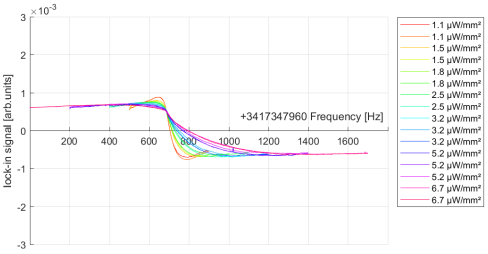

(a) All measurements

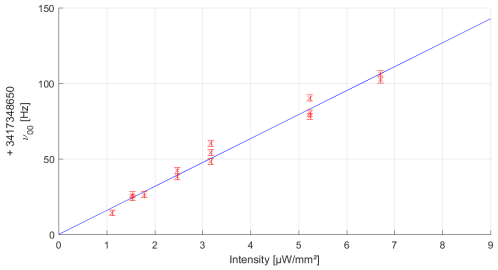

(b) ν_{00}-drift: $\nu_{00}drift(I) = 15.9I$

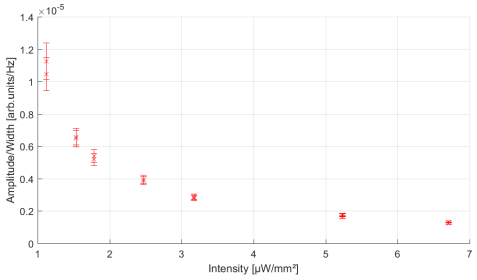

(c) Amplitude-width ratio

Figure 6.36: Laser width dependence

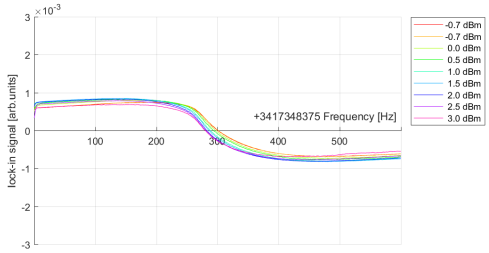

(a) All measurements

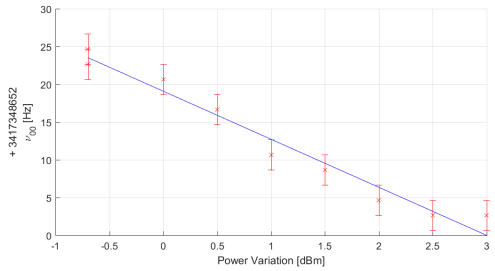

(b) ν_{00}-drift$\nu_{00} drift(PV) = -6.3PV$

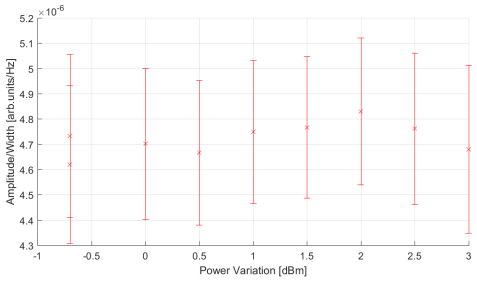

(c) Amplitude-width ratio

Figure 6.37: Power variation

6.15 1509-005

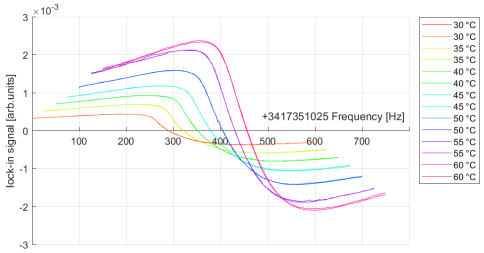

(a) All measurements

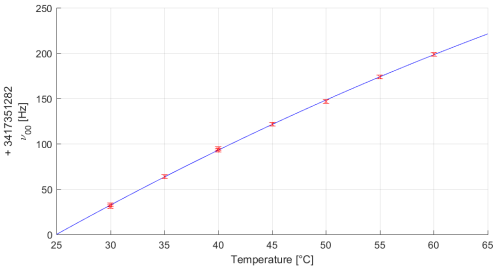

(b) ν_{00}-drift: $\nu_{00}drift(T) = 7.9T - 0.03T^2$

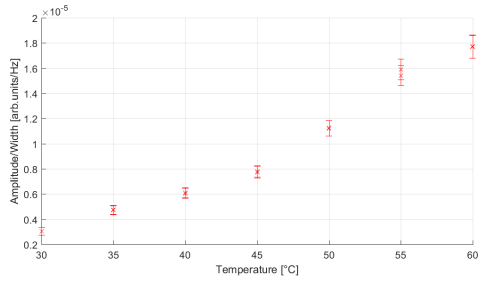

(c) Amplitude-width ratio

Figure 6.38: Temperature dependence

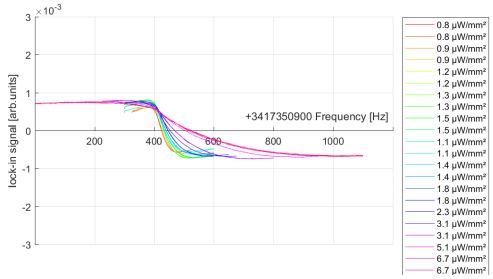

(a) All measurements

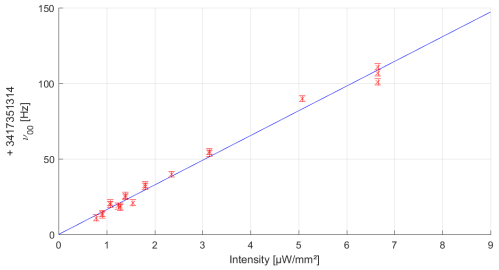

(b) ν_{00}-drift: $\nu_{00}drift(I) = 16.4I$

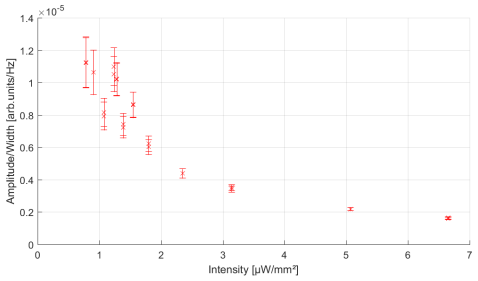

(c) Amplitude-width ratio

Figure 6.39: Laser width dependence

6.16 Special T

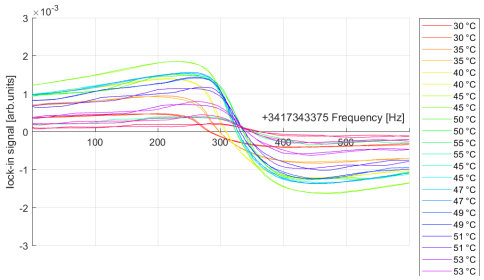

(a) All measurements

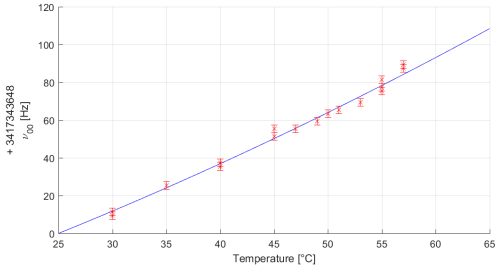

(b) ν_{00}-drift: $\nu_{00}drift(T) = 1.8T - 0.01T^2$

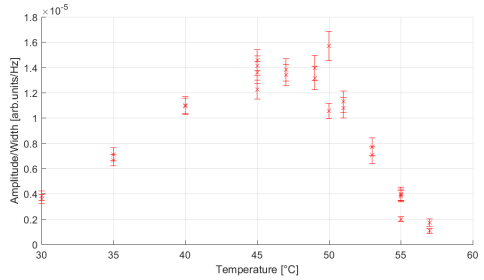

(c) Amplitude-width ratio

Figure 6.40: Temperature dependence

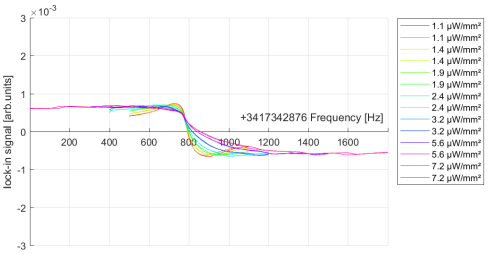

(a) All measurements

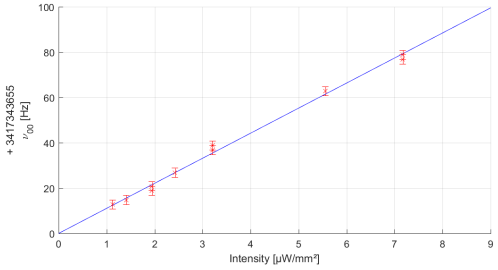

(b) ν_{00}-drift: $\nu_{00}drift(I) = 11.1I$

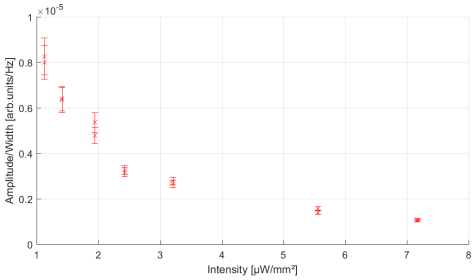

(c) Amplitude-width ratio

Figure 6.41: Laser width dependence

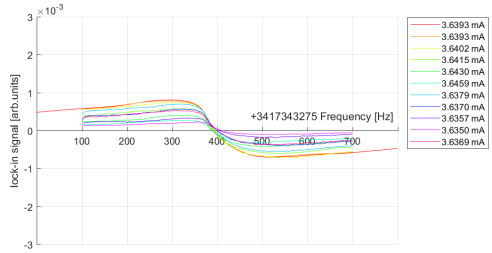

(a) All measurements

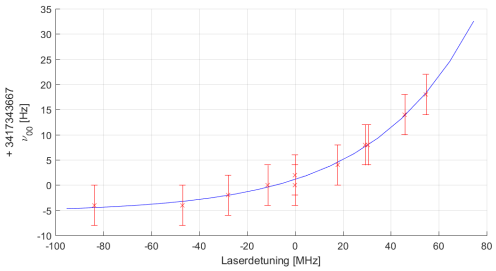

(b) ν_{00}-drift: $\nu_{00} drift(PD) = 6.4e^{-0.024PD}$

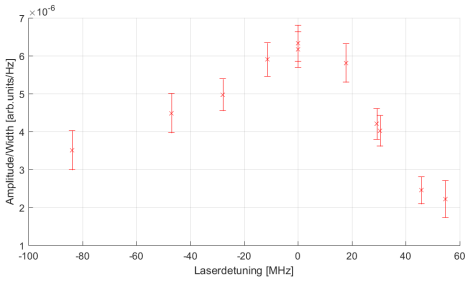

(c) Amplitude-width ratio

Figure 6.42: Two Photon Detuning

Bibliography

[1] E. Arimondo, "Coherent Population Trapping in Laser Spectroscopy," 1996.

[2] G. Alzetta, A. Gozzini, L. Moi, and G. Orriols, "An Experimental Method for the Observation of R.F. Transitions and Laser Beat Resonances in Oriented Na Vapour," *Nuovo Cimento*, vol. 36, 1976.

[3] R. Wynands and A. Nagel, "Precision spectroscopy with coherent dark states," *Applied Physics B: Lasers and Optics*, vol. 68, pp. 1–25, Jan. 1999.

[4] B. D. Agap'ev, M. B. Gornyi, B. G. Matisov, and Y. V. Rozhdestvenskii, "Coherent population trapping in quantum systems," p. 32, 1993.

[5] G. Orriols, "Nonabsorption resonances by nonlinear coherent effects in a three-level system," *Il Nuovo Cimento B Series 11*, vol. 53, pp. 1–24, Sept. 1979.

[6] K. Blum, *Density Matrix Theory and applications*. Plenum Pr, 1989.

[7] Kelley, Harsman, Blum, and Gustafson, "Radaiative renormalization analysis of optical double resonance," *Journal of the Optical Society of America B*, vol. 11, no. 11, 1994.

[8] D. Steck, "Rubidium 87 D Line Data," Sept. 2001.

[9] J. Vanier and C. Audoin, *The Quantum Physics of Atomic Frequency Standards*. No. 1, IOP Publishing Ltd, 1989.

[10] M. Merimaa, T. Lindvall, I. Tittonen, and E. Ikonen, "All-optical atomic clock based on coherent population trapping in ^85Rb," *Journal of the Optical Society of America B*, vol. 20, p. 273, Feb. 2003.

[11] K. Deng, T. Guo, D. W. He, X. Y. Liu, L. Liu, D. Z. Guo, X. Z. Chen, and Z. Wang, "Effect of buffer gas ratios on the relationship between cell temperature and frequency shifts of the coherent population trapping resonance," *Applied Physics Letters*, vol. 92, p. 211104, May 2008.

[12] S. Knappe, L. Hollberg, and J. Kitching, "Dark-line atomic resonances in submillimeter structures," *Optics Letters*, vol. 29, p. 388, Feb. 2004.

[13] W. Demtröder, *Laserspektroskopie. 1: Grundlagen*. Berlin: Springer, 6., aktualisierte aufl ed., 2011. OCLC: 756371794.

[14] R. H. Dicke, "The Effect of Collisions upon the Doppler Width of Spectral Lines," *Physical Review*, vol. 89, pp. 472–473, Jan. 1953.

[15] O. Firstenberg, M. Shuker, A. Ben-Kish, D. R. Fredkin, N. Davidson, and A. Ron, "Theory of Dicke narrowing in coherent population trapping," *Physical Review A*, vol. 76, July 2007.

[16] M. Ellmeier, "Influence of Characteristic Parameters on the Performance of a Coupled Dark State Magnetometer."

[17] I. V. Hertel, C.-P. Schulz, and I. V. Hertel, *Moleküle und Photonen - Spektroskopie und Streuphysik*. No. Ingolf V. Hertel; C.-P. Schulz ; 2 in Atome, Moleküle und optische Physik, Berlin: Springer, 2010. OCLC: 845708635.

[18] J. Vanier, A. Godone, F. Levi, and S. Micalizio, "Atomic clocks based on coherent population trapping: basic theoretical models and frequency stability," pp. 2–15, IEEE, 2003.

[19] R. Boudot, P. Dziuban, M. Hasegawa, R. K. Chutani, S. Galliou, V. Giordano, and C. Gorecki, "Coherent population trapping resonances in Cs–Ne vapor microcells for miniature clocks applications," *Journal of Applied Physics*, vol. 109, p. 014912, Jan. 2011.

[20] B. L. Bean and R. H. Lambert, "Temperature dependence of hyperfine density shifts. IV. Na 23 , K 39 , and Rb 85 in He, Ne, Ar, and N 2 at low temperatures," *Physical Review A*, vol. 13, pp. 492–494, Jan. 1976.

[21] P. L. Bender, E. C. Beaty, and A. R. Chi, "Optical Detection of Narrow Rb 87 Hyperfine Absorption Lines," *Physical Review Letters*, vol. 1, pp. 311–313, Nov. 1958.

[22] V. V. Batygin and V. S. Zholnerov, "Temperature dependence of the hyperfine transition frequency of the ground state of Rb 87 in a buffer medium," *Optics and Spectroscopy*, vol. 39, pp. 254–255, Sept. 1975.

[23] R. W. Herrick, "Reliability of Vertical-Cavity Surface-Emitting Lasers," *Japanese Journal of Applied Physics*, vol. 51, p. 11PC01, Nov. 2012.

[24] J. Jewell, J. Harbison, A. Scherer, Y. Lee, and L. Florez, "Vertical-cavity surface-emitting lasers: Design, growth, fabrication, characterization," *IEEE Journal of Quantum Electronics*, vol. 27, pp. 1332–1346, June 1991.

[25] C. J. Chang-Hasnain, "Tunable VCSEL," *IEEE JOURNAL ON SELECTED TOPICS IN QUANTUM ELECTRONICS*, vol. 6, no. 6, 2000.

[26] C. Affolderbach, A. Nagel, S. Knappe, C. Jung, D. Wiedenmann, and R. Wynands, "Nonlinear spectroscopy with a vertical-cavity surface-emitting laser (VCSEL)," *Applied Physics B: Lasers and Optics*, vol. 70, pp. 407–413, Mar. 2000.

[27] A. Baranov and E. Tournié, *Semiconductor lasers*. Woodhead Publishing Limited, 2013.

[28] K. Y. Lau, P. L. Derry, and A. Yariv, "Ultimate limit in low threshold quantum well GaAlAs semiconductor lasers," *Applied Physics Letters*, vol. 52, pp. 88–90, Jan. 1988.

[29] Z. I. Alferov, "Nobel Lecture: The double heterostructure concept and its applications in physics, electronics, and technology," *Reviews of Modern Physics*, vol. 73, pp. 767–782, Oct. 2001.

[30] P. N. Melentiev, M. V. Subbotin, and V. I. Balykin, "Simple and Effective Modulation of Diode Lasers," vol. 11, no. 7, p. 6, 2001.

[31] S. Kobayashi, Y. Yamamoto, M. Ito, and T. Kimura, "Direct Frequency Modulation in AlGaAs Semiconductor Lasers," p. 14.

[32] T. L. Paoli, "Direct Modulation of Semiconductor Lasers," p. 9.

[33] C. Cohen-Tannoudji and J. Dupont-Roc, "Experimental Study of Zeeman Light Shifts in Weak Magnetic Fields," *Physical Review A*, vol. 5, pp. 968–984, Feb. 1972.

[34] J. Barrat and C. Cohen-Tannoudji, "Optical pumping and the density matrix formalism," *J. Phys. Radium*, vol. 22, no. 6, pp. 329–336, 1961.

[35] F. Levi, A. Godone, and J. Vanier, "The light shift effect in the coherent population trapping cesium maser," *IEEE Transactions on Ultrasonics, Ferroelectrics and Frequency Control*, vol. 47, pp. 466–470, Mar. 2000.

[36] Jinquan Deng, "Light shift compensation in a Rb gas cell frequency standard with two-laser pumping," *IEEE Transactions on Ultrasonics, Ferroelectrics and Frequency Control*, vol. 48, pp. 1657–1661, Nov. 2001.

[37] J. Vanier, A. Godone, and F. Levi, "Coherent population trapping in cesium: Dark lines and coherent microwave emission," *Physical Review A*, vol. 58, pp. 2345–2358, Sept. 1998.

[38] Zhu and Cutler, "Theoretical and Experimental Study Of Light Shift in a CPT-based Rb Vapor Cell Frequency Standard," Nov. 2000.

[39] J. Vanier, A. Godone, and F. Levi, "Coherent microwave emission in coherent population trapping: origin of the energy and of the quadratic light shift," vol. 1, pp. 96–99, IEEE, 1999.

[40] D. Miletic, C. Affolderbach, M. Hasegawa, R. Boudot, C. Gorecki, and G. Mileti, "AC Stark-shift in CPT-based Cs miniature atomic clocks," *Applied Physics B*, vol. 109, pp. 89–97, Oct. 2012.

[41] Ke Deng, Tao Guo, J. Su, Dengzhu Guo, Xuzong Chen, and Zhong Wang, "Light shift in modulated coherent population trapping atomic clocks," pp. 998–1000, IEEE, Apr. 2009.

[42] W. Demtröder, *Laser Spectroscopy*, vol. Volume 1. Springer, 4 ed., 2009.

[43] S. Knappe, R. Wynands, J. Kitching, H. G. Robinson, and L. Hollberg, "Characterization of coherent population-trapping resonances as atomic frequency references," *Journal of the Optical Society of America B*, vol. 18, p. 1545, Nov. 2001.

[44] J. M. Supplee, E. A. Whittaker, and W. Lenth, "Theoretical description of frequency modulation and wavelength modulation spectroscopy," *Applied Optics*, vol. 33, p. 6294, Sept. 1994.

[45] G. Bjorklund, M. Levenson, W. Lenth, and C. Ortiz, "Frequency modulation spectroscopy," *Applied Physics B*, vol. 32, pp. 145–152, 1983.

[46] G. C. Bjorklund, "Frequency-modulation spectroscopy: a new method for measuring weak absorptions and dispersions," *Optics Letters*, vol. 5, p. 15, Jan. 1980.

[47] A. Pollinger, R. Lammegger, W. Magnes, C. Hagen, M. Ellmeier, I. Jernej, M. Leichtfried, C. Kürbisch, R. Maierhofer, R. Wallner, G. Fremuth, C. Amtmann, A. Betzler, M. Delva, G. Prattes, and W. Baumjohann, "Coupled Dark State Magnetometer for the China Seismo-Electromagnetic Satellite," *Measurement Science and Technology*, 2018.

[48] B. Cheng, B. Zhou, W. Magnes, R. Lammegger, and A. Pollinger, "High precision magnetometer for geomagnetic exploration onboard of the China Seismo-Electromagnetic Satellite," *Science China Technological Sciences*, vol. 61, pp. 659–668, May 2018.

[49] ESA, "JUICE - JUpiter ICy moons Explorer - Red Book," Sept. 2014.

[50] S. Knappe, "Dark Resonance Magnetomerters and Atomic Clocks," Apr. 2001.

[51] G. Breit and I. I. Rabi, "Measurement of Nuclear Spin," p. 2.

[52] R. Lammegger, "Method and Device for measuring magnetic Fields," July 2010.

[53] E. Arimondo, "Relaxation processes in coherent-population trapping," *Physical Review A*, vol. 54, pp. 2216–2223, Sept. 1996.

[54] M. Erhard, S. Nußmann, and H. Helm, "Power broadening and Doppler effects of coherent dark resonances in Rb," *Physical Review A*, vol. 62, Nov. 2000.